ACCSCIENCE PUBLISHING

Engineering Science in Additive Manufacturing

REVIEW ARTICLE

Multi-material additive manufacturing of metals: A review of structures and mechanical characteristics

Saneej N. Samad[1], **Jacklyn Griffis**[2], **Guha Manogharan**[2], and **Nadia Kouraytem**[1]*

[1]Department of Mechanical and Aerospace Engineering, College of Engineering, Utah State University, Logan, Utah, United States of America

[2]Department of Mechanical Engineering, College of Engineering, Pennsylvania State University, Philadelphia, Pennsylvania, United States of America

Abstract

The ability to manufacture complex designs from multiple materials has long been a key objective for applications operating in extreme environments. Multi-material (MM) additive manufacturing (MMAM) has significantly enhanced the functionality of additive manufacturing (AM) by enabling the integration of dissimilar alloys while leveraging the inherent advantages of AM, including design flexibility, reduced material waste, and rapid production, with the ability to tailor mechanical properties through spatial material distribution and local processing conditions. This process unlocks unprecedented opportunities across industries such as aerospace, automotive, biomedical, energy, and nuclear sectors. This article provides a comprehensive review of the state-of-the-art in MMAM, focusing on the manufacturing processes, molten pool formation, alloy compatibility, and bimetallic interface characteristics—including microstructural and mechanical properties—as well as modeling and simulation approaches for performance prediction and optimization, with developments tracked from 2013 to 2024. This review article predominantly focuses on: (i) MM-laser powder bed fusion, (ii) MM-directed energy deposition, and (iii) MM-wire-arc AM by detailing the mechanisms of molten pool formation at the interface and dissimilar alloy material compatibilities. Subsequently, the article provides an in-depth analysis of the meso- and micro-structural characteristics at the interface in bimetallic structures across widely employed MMAM alloys. The mechanics of MMs under various mechanical properties are presented, including microhardness/micro-indentation, tensile, flexural, compression, and fatigue strength, which are critical for MMAM applications in extreme conditions. In addition, current modeling and simulation approaches for MMAM are discussed with respect to the challenges and opportunities to increase MMAM adoption. The article concludes with a future roadmap for advancing MMAM by overcoming feedstock and build material cross-contamination, monitoring the *in situ* process, standardizing MM testing, and further developing thermo-mechanical modeling, specifically, for MMAM.

Keywords: Multi-material additive manufacturing; Interfacial boundary layers; Process–structure–property relationships; Three-dimensional printing; Mechanical behavior; Modeling and simulation

***Corresponding author:**
Nadia Kouraytem
(nadia.kouraytem@usu.edu)

Citation: Samad SN, Griffis J, Manogharan G, Kouraytem N. Multi-material additive manufacturing of metals: A review of structures and mechanical characteristics. *Eng Sci Add Manuf.* 2025;1(2):025180010. doi: 10.36922/ESAM025180010

Received: May 1, 2025

Revised: June 8, 2025

Accepted: June 13, 2025

1. Introduction

Metal additive manufacturing (AM) is revolutionizing industries with its growing adoption across automotive,[1,2] nuclear,[3-5] aerospace,[6-9] energy,[10-12] and biomedical sectors.[13-18] Utilizing a layer-by-layer approach guided by computer-aided design models,[19] metal AM offers transformative advantages over traditional manufacturing methods, including reduced material waste, accelerated production cycles, enhanced part consolidation, and unprecedented design flexibility. While significant strides have been made in fabricating single-material components, the next frontier lies in further advancing multi-material (MM) metal AM (MMAM). Enhancing the quality, reliability, and performance of MM components is critical to unlocking their full potential and meeting the rigorous demands of real-world applications—a challenge this review seeks to address following a roadmap consisting of six topics, as presented in Figure 1.

Recent advancements in AM have enabled the processing of multiple materials within a single build, a technique referred to as MMAM. Components manufactured using MMs can produce tailored mechanical properties according to spatial part design requirements, and concurrent local material assignment and processing conditions. In addition to the tailored mechanical characteristics, the MMAM approach also enables manufacturing complex structures that are otherwise cost-prohibitive or often not feasible through other manufacturing methods.[24-30] Recent advancements in material deposition have enabled AM users to achieve precision control at the voxel length scale in the order of a few hundred microns.[31,32] By leveraging the existing advantages of AM processes, ongoing advancements in MM would introduce a new paradigm and range of opportunities for design, mechanical properties, and manufacturing capabilities.[33]

Despite the numerous advantages of MMAM, limitations in the detailed understanding of the process–structure–property (P-S-P) relationships present severe constraints in fully adopting and leveraging its capabilities.[34] Some examples of the critical challenges faced by MMAM include the complex behavior at the interfaces of the dissimilar materials, heterogeneous thermal properties (melting temperature, thermal conductivity, laser absorptivity, and coefficient of thermal expansion [CTE]), and cross-contamination between virgin and used powders. Addressing these gaps is essential for qualifying MMAM for high-performance applications in aerospace, defense, energy, biomedical, and other emerging industries.

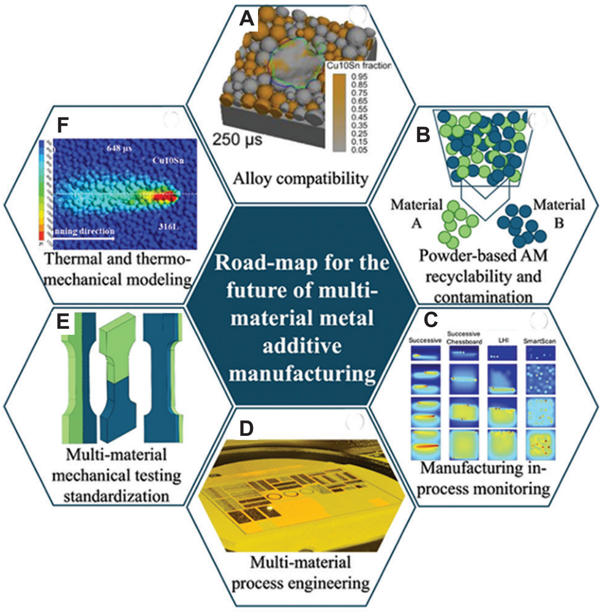

Figure 1. Road map for the future of bimetallic multi-material additive manufacturing (MMAM). Includes the discussion on (A) alloy compatibility. Reproduced with permission from Sun *et al.*[20] Copyright© Elsevier 2020. (B) Powder recyclability and contamination, (C) AM in-process monitoring techniques. Reproduced with permission from He *et al.*[21] Copyright© Elsevier 2023. (D) MMAM process engineering,[22] (E) MMAM mechanical testing standardization, and (F) modeling and simulation.[23] Reproduced with permission from Aerosint Company[22] and Gu *et al.*[23] Copyright © Elsevier 2020.

To effectively address these challenges, it is vital to examine the most widely adopted metal AM processes that have been proven for single metallic materials and are under rapid development for MMAM. The list includes three main processes: (i) Laser-based powder bed fusion (LPBF) and electron-beam powder bed fusion (EB-PBF), (ii) laser-directed energy deposition (LDED), and (iii) wire-arc AM (WAAM). Among these, LPBF is known for achieving higher dimensional accuracy; however, it suffers from small build volumes, low surface roughness, and low production efficiency. These drawbacks result from factors such as fine powder particles (10 – 50 μm),[35] relatively large laser spot size (50 – 80 μm),[36] small layer thickness (<100 μm),[37] and a high risk of powder cross-contamination.[38-41] In Section 2.1, the author will discuss in depth the advantages and limitations of LPBF. In contrast, LDED and WAAM offer significant advantages in terms of higher deposition rate, minimal cross-contamination between multiple materials, and suitability for large-scale component manufacturing. However, these techniques are associated with high surface roughness and low-dimensional accuracy (100 μm).[39] Given these trade-offs, recent progress has focused on leveraging all three process techniques for the fabrication of MM components. A detailed description of each process and the mechanics of melt pool formation, as well as alloy compatibility in

MMAM, is provided in Section 2. Using these processes, the transition between dissimilar materials can be either discrete or gradual.

The interfaces of MMAM structures consist of either a discrete boundary (discrete MMAM), characterized by a direct transition between two materials; a functionally graded boundary—in which the proportion of material composition varies along the interface—or a discrete boundary incorporating a third material as an interlayer, as shown in Figure 2. Functionally graded materials (FGM) enable complex and locally controlled MM component fabrication by providing smooth transitions between dissimilar materials. However, FGM comes with limitations, such as inconsistent gradient control and unpredictable feedstock deposition, which may limit the repeatability and precision of the FGM components. In contrast, discrete MMAM with direct compositional change (including adaptation of interlayer material) offers significant engineering benefits such as increased flexibility in design and production, property optimization, and the ability to realize complex functionalities.[42,43] Both FGM and discrete MMAM components can deliver localized enhancements, such as high wear resistance, high-temperature resistance, and corrosion resistance in target regions, while maintaining traditional mechanical properties at adequate level, an approach that is often restricted in single-material components.[40,44] For the reader's ease, the term MMAM will now be used interchangeably with discrete MMAM to identify a discrete compositional change between dissimilar materials using AM here on.

The adoption of MMAM has garnered increasing interest across industries such as aerospace,[22,45-49] automotive,[50,51] biomedical,[52] and nuclear energy.[53,54] In the aerospace industry, MMAM implemented functionality in propulsion, heat exchangers, and other components. For instance, in 2017, the National Aeronautics and Space Administration launched the "Rapid Analysis and Manufacturing Propulsion Technology" program to reduce the cost and weight of the thrust chamber assembly. This initiative utilized bimetallic joints to directly fuse the copper (Cu) combustion chamber with the nickel (Ni) alloy nozzle, eliminating the need for additional fasteners. Cu/Ni alloy combinations are particularly suitable for propulsion applications due to the high thermal conductivity of Cu and the mechanical strength of Ni.[45-47] Another MMAM demonstration in industry integrated titanium (Ti) and aluminum (Al) to manufacture a lightweight yet corrosion-resistant spaceflight frame, capitalizing on Ti's high corrosion resistance and Al's lightweight.[48] Another example of MMAM application is the Cu/stainless steel (SS) MMAM heat exchanger fabricated by Aerosint (Belgium), where complex Cu channels were embedded in SS to produce a monolithic structure that demonstrated a relatively higher cost-effectiveness over conventional manufacturing.[22] Similarly, an SS/Ni component was manufactured through MMAM for a heat exchanger by leveraging the high-temperature performance of Ni and the higher ductility, corrosion resistance, and lower cost of SS.[49] The applications of MMAM in aerospace have extended to vital components such as propulsion systems, heat exchangers, and spacecraft body frames without compromising functional performance.

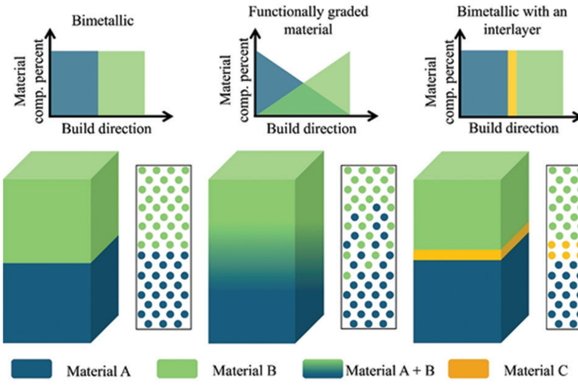

Figure 2. Schematic illustration of bimetallic, functionally graded materials, and interlayer-assisted multi-material additive manufacturing structures, highlighting the differences in materials transition and material compositional distribution characteristics across the interface Abbreviation: Comp.: Composition.

The impact of MMAM extends beyond the aerospace industry. With the growing adoption in the automotive industry, components such as electric motor rotor[51] and car chassis[50] have been fabricated using MMAM techniques with iron (Fe)/Ni and Al/SS compositions, respectively. The design flexibility enabled through LPBF allowed for the reduction of eddy currents and increased motor efficiency. Meanwhile, the Al/SS MMAM chassis helped reduce the vehicle's weight while maintaining higher strength and corrosion resistance. Similarly, to the automotive industry, the biomedical fields,[52] nuclear energy,[53,54] and anti-counterfeiting[55] have implemented MMAM. The MMAM of Ni/Ti has been explored as a viable hip implant due to its shape memory behavior and bio-compatibility.[52] In the nuclear energy industry, tungsten/Cu has been explored for use in fusion nuclear reactor components, leveraging their combined high-temperature resistance and excellent plasma radiation resistance properties.[53,54] Besides the large-scale industries, MMAM has shown promise in anti-counterfeiting, where embedded safety features, such as a quick response code, have been incorporated into metallic components made of SS/Cu alloys to allow traceability and authentication.[55]

While the array of current applications of MMAM demonstrates its versatility, a deeper understanding of the underlying microstructures, mechanical behavior, and modeling and simulation of materials used in MMAM is crucial to ensure wider adoption. The goal of this review article is to identify a potential road map for advancing the field of MMAM by providing a detailed insight into the current state of microstructure, mechanical characteristics, and modeling and simulation of MMAM structures. In contrast to previous review articles (Table A1), which have primarily focused on FGM, this article gathers and synthesizes the results reported in empirical studies that investigated the P-S-P relationships of MMAM structures, with a roadmap toward further development of MMAM. Prior literature has explored various aspects, including applications,[60-66] challenges in FGM-LDED,[60,67] challenges in thermal properties and creation of harmful compounds,[68] challenges in steel- and metal-based FGM,[69,70] progress in structures and functionality of FGM,[71] manufacturing techniques,[60,64,72-75] experimental studies on metal-metal, metal-ceramic and metal-intermetallic gradient, and numerical studies on material science and engineering,[67,76,77] and practical applications.[62,63,67,70,71,74,75,78] While these review articles provide abundant information on MMAM, a critical research gap and future direction (applicable to MMAM) concerning structures with discrete transitions remain unexplored. This article aims to address that gap in the following sections.

To systematically address these research gaps and advance the understanding of structures with discrete transitions, this review article is organized as follows. This review article is divided into five main sections, followed by a discussion and future trends. The first section includes an overview of the processing principles of the three main metal MMAM processes, along with a discussion on MM melt pool formation mechanisms and alloy compatibility observed across the discussed processes. The second section consists of a detailed review of macro- and micro-structural characteristics observed at bimetallic interfaces (e.g., microstructural growth, defects, metallurgical bonding, intermetallic phases) from reported studies. The third section focuses on the available data on the mechanical properties of MMAM (e.g., microhardness, tensile strength, flexural strength, compression, fatigue, *etc.*). The fourth section focuses on the modeling and simulation (e.g., phase transformation, melt pool formation, computer coupling of phase diagrams and thermochemistry [CALPHAD], finite element analysis [FEA]) approaches for bimetallic structures. Finally, the review article closes with a discussion on current technological roadblocks in advancing the development and adoption of MMAM, specifically: (i) Alloy compatibility, (ii) powder recyclability, (iii) AM in-process monitoring, (iv) MM process monitoring, (v) MM mechanical testing standardization, and (vi) thermal- and thermo-mechanical modeling as presented in Figure 1.

2. Overview of MMAM processes

2.1. Laser powder bed fusion (LPBF)

LPBF is a metal-AM process that utilizes a high-powered scanning laser beam to selectively melt a region of a powder bed onto a metal substrate in a layer-by-layer fashion to produce three-dimensional (3D) solid metal parts. Melting occurs on metal powder fabricated through various powder processes (e.g., gas atomization, plasma atomization, plasma rotating electrode process, hydride-dehydride, and wire atomization) inside a sealed inert gas build chamber, usually filled with argon or nitrogen, which is pumped throughout the build chamber to maintain a low oxygen content. Previous studies indicate that an oxygen content of 300 – 1,000 ppm is required to prevent oxidation during the manufacturing process.[79] In addition to maintaining a low oxygen content, inert gas is used to reduce the likelihood of defects associated with high oxygen levels, which may include irregular melt track morphology, irregular melt pool surface tension, and spattering.[80-83] The build plate, as shown in Figure 3A, is made of a material similar to the feedstock metal and can be preheated to minimize thermal gradients and reduce the buildup of thermally induced residual stresses or thermally induced part distortion.[84] LPBF imposes process-specific design constraints on part geometry and material selection but offers an elevated level of design complexity compared to traditional subtractive manufacturing methods. The metal alloys that are compatible with LPBF include Ti, Al, Fe (steels), cobalt–chromium, Ni, and Cu-based alloys (analogously, any metal that can be welded).[85] Similar to the single-material LPBF process, in MM-LPBF, the powder that is not melted is retained in the powder bed while dissimilar material is deposited over it, following a process analogous to single-material LPBF. The dissimilar material powder spreading mechanism in MM-LPBF comprised various methods, such as (i) blade-based dissimilar material spreading, (ii) ultrasonic-based dual powder dispenser, (iii) electrophotographic-based dual powder dispense, and (iv) "blade + ultrasonic" hybrid powder spreading technique, which were used.[40]

Advantages of MM-LPBF include (i) the ability to manufacture intricate 3D structures monolithically,[86] (ii) high resolution and rigorous build accuracy with dimension error lower than 100 μm,[39] (iii) better processing accuracy compared to other metal-AM due to smaller powder size (10 – 50 μm),[35] larger laser spot diameter (50 – 80 μm),[36]

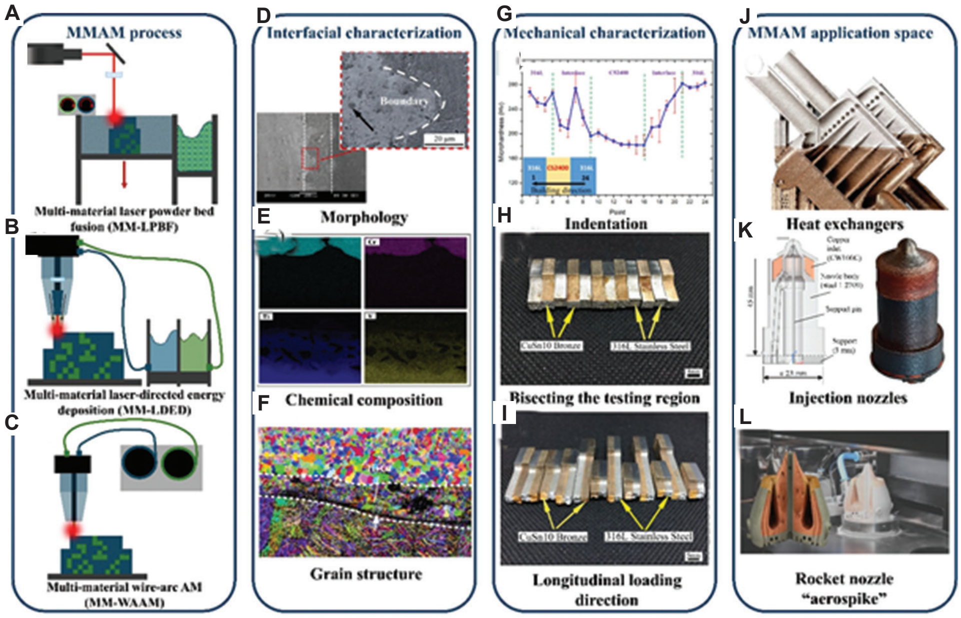

Figure 3. Summary of discrete multi-material (MM) additive manufacturing (MMAM) processes, interfacial characterization techniques, mechanical properties characterization, and industrial applications. (A-C) The three common methods of metal MMAM are MM-LPBF, MM-DED, and MM-WAAM. (D-F) Common methods of interfacial characterization, namely scanning electron microscopy,[140] energy dispersive spectroscopy,[140] and electron backscatter diffraction,[57] respectively. Scale bar: 100 μm. Reprinted with permission from Bai *et al.*[140] and Wei *et al.*[57] (G-I) Methods of mechanical characterization of MMAM structures through indentation hardness testing[140] and tensile testing with variations in material orientation.[58] Reprinted with permission from Bai *et al.*[140] and Chen *et al.*[57]. Copyright© Elsevier 2019. (J-L) Space applications of MMAM designs.[49,59,23] Reprinted with permission from Wessel and Amsterdam,[49] Schneck *et al.*,[59] and Gu *et al.*[23] Copyright© Elsevier 2021.

and smaller layer thickness (<100 μm).[37] Limitations of MM-LPBF include (i) limited build size, (ii) challenges in powder recyclability, and (iii) dependence on powder size and processing parameters.

2.2. Laser-directed energy deposition

Laser-directed energy deposition is defined as an "AM process in which focused thermal energy is used to fuse materials by melting as they are being deposited" by the ISO/ASTM 52900 standard.[87] The LDED process deposits powder feedstock directly onto the substrate by melting it in a controlled heated region using focused energy in the form of a laser, electron beam, or plasma arc.[88,89] The process of feeding molten powder or wire feedstock into a melt pool produced by the heat source beam builds material onto the substrate in a layer-wise process, followed by rapid solidification. The feedstock can be changed mid-process to produce discrete or graded heterogeneous components with tailored material properties. Inert gases are used during the AM process to prevent the molten pool from being contaminated by unmelted powder particles or porosities.[88] In multi-material LDED (MM-LDED), the fabrication process follows the same method as a single-material LDED with the inclusion of dissimilar materials through powder ejecting nozzle from different hoppers (Figure 3B). These nozzles can be mounted onto a multi-axis arm that moves around a fixed component or onto a tool head to deposit onto a component mounted in a five-axis vice.[90] Given these capabilities, MM-LDED offers unique advantages and limitations, as summarized below.

Advantages of MM-LDED include (i) inherent functionality of depositing MM and location-specific material deposition,[88,89,91] (ii) higher rate of deposition rates compared to PBF,[88,92,93] (±2.5 kg/h for LDED vs. ±0.01 kg/h for LPBF vs. ±0.25 kg/h for EB-PBF),[94] (iii) large-scale fabrication (compared to LPBF),[92,93,95] and (iv) potential use for coating, cladding,[96,97] and repairing damaged parts.[98,99] Limitations of MM-LDED include (i) limited design freedom due to lower-dimensional accuracy and higher surface roughness,[95,100] (ii) low powder efficiency and recyclability, particularly in MM, and (iii) possible shrinkage, residual stress, and deformation due to thermal process cycling. LDED is commonly paired with computer numerical control machining as a hybrid-AM solution to resolve the poor surface finish and achieve near-net shape geometry.[93]

2.3. Wire arc AM

Wire arc AM is a subset of LDED that uses a welding arc to generate a melt pool. WAAM is gaining more interest and traction in the AM community, especially for MMAM; hence, it is presented separately here and in subsequent discussions. In WAAM, a wire of heterogeneous characteristic materials is fed into the melt pool created by the welding arc along the designed path to form a component (Figure 3C). WAAM is compatible only with wire feedstock, like the feeding rods used in most welding processes. As a result, material restrictions include only materials that are ductile enough to be pulled into the wire. Weldable materials such as SS, Ni, Ti, and Al alloys are commonly used in WAAM.[71,101] Like MM-LDED, multi-material WAAM (MM-WAAM) follows the same procedure as the dissimilar materials deposited through a wire-fed nozzle. Building upon the basic WAAM process, the major advantages and challenges associated with MM-WAAM are outlined below.

The advantages of WAAM coincide with those of LDED. While WAAM offers a higher deposition rate than PBF, it comes at the expense of increased surface roughness and reduced dimensional accuracy. To improve the surface finish and dimensional accuracy, components are often required to undergo post-processing or subtractive machining to produce near-net shape geometry. Alongside a higher deposition rate, WAAM is associated with an inexpensive machine cost, simple configuration, high efficiency, and large-scale component fabrication.[71,102-105]

2.4. Mechanisms of melt pool formation

The formation of a bi-metallic interface using MMAM processing involves thermal and fluidic interactions between the solid substrate and the unmelted feedstock of the dissimilar metal. A key challenge in MMAM processing is mitigating the defects that tend to form at the interface of the dissimilar metals, mainly caused by the mismatch in thermal properties. This mismatch may induce macro-strains near the interface and cause defects such as cracking and porosity. Understanding the mechanisms of melt pool formation and the subsequent cooling process is a necessary foundation for mitigating the formation of defects in that region.

In all metal MMAM processes, many studies characterize the interface as having grain refinement and report an increase in hardness across the transition. For processes such as MM-LPBF, a high cooling rate (10^7 K/s) compared to other laser or arc-welding processes (10^3 K/s) may cause additional grain refinement. Grain refinement may be further exaggerated for all processes while printing bi-metallic structures, which pair highly conductive materials (such as Cu alloys) with a moderate alloy (such as steel), wherein the highly conductive material may act as a heat-sink and expedite the cooling rate of the more moderate material. Generally, material pairs that have the most contrasting thermal properties are reported to have a weaker metallurgical bond at the interface. For example, a moderately conductive steel alloy, which is commonly paired with a highly conductive Cu alloy (Table 1), is usually reported as having poor bonding, where local cracking is the most common defect near the interface. Reports show that cracking occurs in these Cu alloys for two main reasons: (i) A mismatch of the thermo-physical material properties and (ii) an infiltration of Cu to the grain boundaries in steel, which provides micro-cracks during melting due to thermal mismatch. Optimizing process parameters, namely those related to the temperature distribution (e.g., laser speed, power, and scanning strategy), can help mitigate the severity of the thermal gradient across the interface and improve metallurgical bonding.

The dilution effect is another common phenomenon observed in MMAM processes and describes the gradual decrease in alloy blending as a part is built in the vertical direction. Dendritic cracking commonly occurs perpendicularly to the boundary of the fusion zone and extends gradually into the material of the higher thermal stress, which is usually the less conductive material. Dendritic cracking is influenced by the thermomechanical stresses that arise due to the temperature gradients during the solidification processes. The presence of a secondary alloy in the melt pool can exacerbate these stresses and increase the likelihood of crack formation. Cracking from dissimilar metal mixing is further discussed in Section 2.5. On a related note, element diffusion at the interface describes the causal mechanisms behind the blending of two dissimilar alloys within the melt pool. Diffusion is aided by the Marangoni convective forces, driven by the surface tension gradients of the melt pool's molten fluid. This leads to a non-homogeneous distribution of elements, commonly observed by the solidified heat-affected zones through energy dispersive spectroscopy (EDS). The difference in material density may also play a role in how the metals mix and interact under gravitational forces. All factors considered in this section play a crucial role in identifying the alloy compatibility between dissimilar materials in MMAM.

2.5. Alloy compatibility in MM mixtures

Achieving compatibility between dissimilar alloys in bimetallic structures is a critical challenge, as differing physical, chemical, and mechanical properties of each alloy can significantly influence the performance and longevity of the components. The alloys are designed precisely to tailor the elemental proportions and thermomechanical processing conditions to generate the ideal microstructural

Table 1. A comprehensive summary of the empirical literature on the metallurgical bonding in bimetallic multi-material additive manufacturing

Base material \ Deposited material	Titanium alloy	Stainless steel alloy	Nickel alloy	Aluminum alloy	Copper alloy	Ferrous alloy	Miscellaneous alloy
Stainless steel alloy	122,123	124,125	91,126-138	50	33,56,58,128, 139-146	147	148,149
Titanium alloy	150-153	154	155	—	55	—	—
Nickel alloy	52,156	91,131,132, 157-161	—	—	47,162,163	164	—
Ferrous alloy	165	166	—	—	167,168	169,170	171
Aluminum alloy	—	—	—	172-174	175	176	177
Copper alloy	—	178	—	—	179	—	—

features and mechanical properties.[39] In FGM, the element composition typically varies throughout the structure, with the ratio of elements varying with respect to the build height. A minor deviation in element content from the intended composition could disrupt the alloy's performance and fundamental properties.[106] In the discrete MMAM, the abrupt change of composition could act as a chemical potential gradient that drives alloying elements and impurities from one side to another, leading to failure mechanisms. Similar behavior could be observed in a steep property gradient of FGM, which serves as a residual stress concentration site during manufacturing. Besides the chemical composition of the alloys, properties such as thermal conductivity and melting temperature can prevent the successful joining of dissimilar alloys.

To better understand these challenges, Reichardt *et al.*[106] noted that most dissimilar joining issues can be grouped into three distinct categories: (i) Intermetallic formation and solubility limitations, (ii) thermal property mismatch, and (iii) other metallurgical effects. In Section 3, which focuses on the interfacial characteristics of the discrete MMAM structure, the aforementioned phenomena can be observed. Many of these issues have been resolved in the welding industry through effective practice of introducing filler metals, interlayer blazing, high energy density beam welding, and friction stir welding.[42,106-108] The three main categories of joining issues and strategies to overcome each will be examined in more detail. From those, the formation of brittle intermetallic phases in dissimilar alloys is the biggest challenge in the MMAM process. Most metal alloys have limitations in solid solubility and tend to form ordered intermetallic phases. This becomes more complex when considering commercial alloys with multiple elements, including impurities that could lead to detrimental phases. In cases of Ti/steel or Ti/Ni alloys (Sections 3.1, 3.2, and 3.3 for more explanation), which tend to form brittle intermetallic approaches such as introducing a third dissimilar metal alloy that acts as an interlayer can be used to resolve the problem. Apart from the intermetallic formation, the thermal property disparity between dissimilar alloys plays a significant role in metallurgical bonding.

The disparity between the thermal properties of dissimilar alloys, such as melting temperature, CTE, and thermal conductivity, is one of the issues that contribute to weaker metallurgical bonding. During the MMAM process, significant differences in melting temperature not only lead to a non-uniform heat flow and dilution but also tend to cause cracking on the low melting temperature alloy side during solidification (e.g., SS316L/W).[109] The cracking attributed to this mismatch in melting temperature can be mitigated by introducing an intermediate melting temperature alloy. Similar to the characteristics difference of dissimilar melting temperature, CTE, and thermal conductivity play a significant role in the interfacial bonding region of the bimetallic structures. Regarding CTE, thermal mismatch can result in an unequal thermal contraction, leading to a stress concentration at the interface. The disparity of thermal conductivity could cause distortion and a lack of complete fusion of the low thermal conductivity material due to insufficient heat present. In Section 3, a detailed description of the bimetallic structures that were analyzed using EDS, electron backscatter diffraction, and X-ray diffraction to understand the alloy compatibility at the abrupt change in element composition in discrete MMAM is presented.

2.6. Powder recyclability and reuse

Powder reuse presents complex challenges due to the diverse thermal properties, oxidation susceptibility, and chemical reactivity of the constituent alloys. These factors critically affect process stability, part performance, and reproducibility. In powder-based metal AM processes such as LPBF, EB-PBF, and LDED, powder degradation is influenced by its interaction with high-energy sources (e.g., laser and electron beam), molten metal, ambient reactive chemical compounds, and contact with mechanical components present in the build chamber (i.e., recoater).[110]

Powder degradation occurs due to thermal, chemical, and mechanical effects, including but not limited to dealloying, sintering, oxidation, deformation, contamination, oxide deposition, particle fragmentation, and wear. The mechanisms are exacerbated by the intense heat input inherent in beam-based AM. LPBF and EB-PBF techniques typically operate under vacuum or inert gas conditions, mitigating oxidation and cross-contamination risks. LDED is more susceptible to such degradation as a result of relatively less controlled atmospheres.

The key contributing factor to powder degradation in powder-based metal AM is its direct interaction with the melt pool. The dynamic flow within the melt pool can lead to the ejection of molten metals, resulting in the formation of metal jets, droplets, and powder spatter. These spatters, rich in partially fused and oxidized particles, can further contaminate the powder bed, compounding degradation across build layers. This understanding of degradation mechanisms is crucial, as the degraded powder significantly impacts the mechanical behavior of printed components.

The use of degraded powder affects key mechanical properties, including chemical composition, density, porosity, tensile strength, and surface roughness. In single alloy materials, the use of recycled powder can lead to a gradual change in chemical composition, particularly in critical alloys such as IN718[111] and Ti-48Al-2Cr-2Nb,[112] which in turn influences the mechanical properties. Studies on density and porosity have shown that reused powder can lead to lower or less predictable part densities, driven by uneven particle size distributions, increased spatter presence, and incomplete melting.

Beyond the chemical composition, density, and porosity, the use of recycled powder has been shown to have a significant effect on the material's tensile properties. Properties such as ultimate tensile strength (UTS), yield strength (YS), Young's modulus, and elongation have seen the most change, though the extent varies with the alloy. Tang *et al.*[113] observed that the use of recycled Ti-6Al-4V powder alloy resulted in an increase in strength due to high oxygen content, whereas SS316[114] and AlSi10Mg[115] typically exhibit reduced strength and stiffness, mainly due to higher porosity and coarser particle sizes.

Finally, surface roughness is another critical factor that is affected by powder reuse. Recycled powders often contain larger particles that do not fully melt, leading to a rougher surface finish. This not only degrades the build quality but also increases the need for post-processing, which is both costly and time-consuming. Studies involving SS316,[114] Ti-6Al-4V,[116] and IN718[117] confirm that surface roughness worsens with powder reuse, potentially compromising fatigue resistance and overall component performance.

Given this detailed understanding of powder degradation and its consequences, it is essential to explore the current state-of-the-art recycling techniques. These range from mechanical to advanced approaches. For a more in-depth understanding, the authors recommend reviewing the articles by Lanzutti and Marin[118] and Powell *et al.*[110] A range of powder recycling and rejuvenation techniques has been explored; conventional strategies include mechanical methods (e.g., sieving and centrifugal separation), thermal treatment (e.g., vacuum degassing, re-sintering, and conventional remelting), and chemical approaches (e.g., acid and electrochemical etching). Emerging technologies such as plasma cleaning and plasma spheroidization offer promising methods as well. Plasma cleaning uses ionized gas to remove surface contaminants (e.g., moisture and trapped gases), whereas plasma spheroidization reshapes irregular powder particles to improve flowability and packing density.

While most current research focuses on single-alloy powder reuse, MM powder recyclability in MMAM remains underexplored. A detailed discussion of future research direction in MMAM powder reuse is presented in Section 6.1.

2.7. In-process monitoring

In-process monitoring has emerged as a critical enabler for ensuring process stability, defect mitigation, and quality assurance in MAM, particularly when fabricating MM components. In-process monitoring in PBF, LDED, and WAAM processes benefits from *in-situ* monitoring techniques aimed at detecting defects and ensuring part quality during fabrication. In PBF, monitoring focuses on powder spreading uniformity, laser-powder interactions, melt pool characteristics (size, shape, and temperature), scan path accuracy, and layer geometry. Optical imaging, pyrometry, infrared (IR) cameras, and data-driven methods such as computer vision and neural networks are commonly used to identify defects such as porosity or incomplete fusion.[119,120] Real-time monitoring facilitates process parameter adjustments to reduce defects and improve part consistency.

Similarly, in LDED, monitoring methods include pyrometry, IR imaging, and acoustic emission (AE) sensors to track melt pool temperature, build height, and crack formation. These sensors enable closed-loop control strategies to maintain stable thermal conditions and geometry, improving material uniformity and reducing defects.[120,121] WAAM uses comparable optical and thermal techniques, such as near-IR cameras and optical emission spectrometry, to monitor melt pool integrity and surface finish. Emerging approaches like 3D laser scanning have also been applied to detect geometric deviations during builds.

Moreover, current state-of-the-art in-process monitoring could allow the research community to further characterize and advance MMAM, which will be further discussed in Section 6.2.

3. MM bimetallic interfacial characterization

The microstructures at the interfaces between dissimilar materials play a crucial role in dictating the mechanical properties of MMAM components. In the context of bimetallic structures, the materials involved often possess similar atomic bonds, as well as comparable physical and chemical properties, including melting temperature, CTE, thermal conductivity, and elemental composition.[39] Consequently, a fusion region is formed at the interface of dissimilar materials, facilitating the interlocking of materials and thereby enhancing their metallurgical bonding strength. Such insights underscore the importance of understanding and optimizing microstructural characteristics for the advancement of MMAM.

The interfacial microstructure of dissimilar materials exhibits varying traits, necessitating a closer examination of each material's unique characteristics. This section explores the microstructural characteristics of significant bi-metal alloys, namely Ti, SS, Ni, Al, and Cu as base materials. Each of these alloys presents distinctive interfacial characteristics influenced by factors such as composition, crystalline structure, and processing conditions. Understanding these nuances is crucial for optimizing MMAM process parameter selection and improving the mechanical properties of MMAM structures. Each subsection is focused on one base material alloy and contains a description of the relevant available literature.

3.1. Stainless steel-based bimetallic alloys

Understanding the bonding between SS and Ni has been explored numerous times (Table 1), with a few examples shown in Figure 4. This combination of alloys is relevant in extreme applications, including nuclear and aerospace, where properties such as high strength, corrosion and oxidation resistance, creep, and fatigue resistance are required.[156,180] In the work by Bodner *et al.*,[129] SS316L/IN625 bimetallic structures were fabricated using liquid-dispersed metal powder bed fusion. Due to the residual stress gradient at the interface, a zigzag-patterned crack

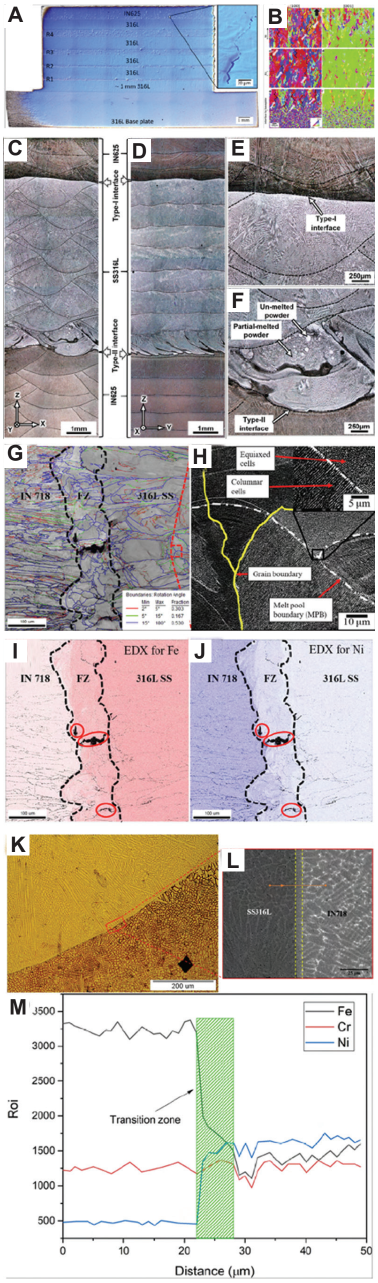

Figure 4. Interfacial meso- and microstructural characteristics of stainless steel and nickel-based bimetallic alloys fabricated through different multi-material (MM) additive manufacturing techniques. (A and B) SS316/IN625 produced by MM-laser powder bed fusion (LPBF). Scale bar: 1 mm. Reprinted with permission from Bodner *et al.*[129] Copyright © 2020, Elsevier B.V. (C-F) SS316/IN625 MM-laser-directed energy deposition (LDED). Scale bars: 1 mm and 250 µm. Reprinted with permission from Chen *et al.*[132] Copyright © 2020, Elsevier B.V. (G-J) SS316L/IN718 MM-LPBF[130] and (K-M) SS316L/IN718 MM-LDED[127]. Scale bars: 5 µm, 10 µm, 25 µm, 100 µm, 200 µm and 250 µm. Reprinted with permission from Yusuf *et al.*[130] Copyright © 2020, Elsevier B.V. and Ghanavati *et al.*[127] The images highlight significant characteristics of the interfacial morphology, phase transformation, grain structure, growth, and bonding quality influenced by the process techniques and material combinations.

propagated from the SS316L interface region and expanded into the IN625, as confirmed by scanning electron microscopy imaging. Such patterned cracks formed due to the implemented scanning strategy, which induced residual stresses and mismatches in CTEs between the sub-layers (Figure 4A and B).

Similarly, Chen *et al.*[132] fabricated multiple layers of SS316L/IN625 using MM-LDED to understand the microstructural characteristics at two types of interfaces: type I (SS316L as a substrate) and type II (IN625 as a substrate) (Figure 4C and D). This section focuses on type I interfaces, while type II will be discussed in Subsection 3.3. The type I interface exhibits a flat transition region due to less penetration compared to type II (Figure 4E and F). The shallower penetration in type I was attributed to the lower energy absorptivity and thermal conductivity of IN625 relative to SS316L. Fractography images revealed no cracks or pores at the interface due to the lower density and viscosity of SS316L compared to IN625. Beyond surface observation, the inverse pole figure map of the type I interface exhibited fine columnar grains in IN625 and equiaxed grains on SS316L. Similarly, in a hybrid-AM process where SS316L was fabricated using LPBF and IN625 using LDED, no cracks or porosity were visible on the surface,[126] which validates the earlier findings. In all cases, the interface exhibited a good transition zone with smooth, defect-free bonding due to comparable melting points and CTE values of the two alloys.

The SS316L/IN718 interface has been similarly analyzed as the SS316L/IN625-LPBF interfaces. Yusuf *et al.*[130] observed that the transition zone exhibits equiaxed grain growth with a transition zone thickness of approximately 100 μm and was characterized by columnar grains in the individual element-rich region (Figure 4G and H). Despite the presence of irregular-shaped lack-of-fusion pores (highlighted in red in Figures 4I and J), no cracks were detected. Similar observations were made by Mei *et al.*[131] and Wei *et al.*,[132] who attributed the formation of pores at the interface to energy-material mismatch and uneven powder deposition during the MM-LPBF fabrication. In contrast, Ghanavati *et al.*[127] reported a nearly defect-free interface between SS316L and IN718 (Figure 4K and L), which was attributed to the presence of a strong local temperature gradient at the interface. The microstructural solidification at the interface proceeded through a narrow planar solidification mode, driven by the high local temperature gradient.[127] An EDS analysis confirmed a smooth transition from the Fe- to Ni-rich region (Figure 4M).

Across various AM processes, the SS/Ni bimetallic structure with SS as substrate generally exhibited good metallurgical bonding. Considering the CTE of SS316L, IN625, and IN718, it is evident that IN718 has a lower CTE compared to IN625. In SS316L/IN625 structures, although the actual temperature increases from SS316L to IN625 due to the heat source, a gradual decrease in the liquid temperature within the transition zone inhibits the protrusion of SS316L into this region, resulting in a smoother interface. As reported by Bodnar *et al.*,[129] it is evident that the process parameters significantly influence the formation of zigzag cracks at the SS316L/IN625 interface. In contrast, for SS316L/IN718 bimetallic structures, porosity and cracks were clearly observed in MM-LPBF rather than MM-LDED. This behavior was attributed to the formation of brittle intermetallic phases during solidification, coupled with the lower CTE of IN718 compared to SS316L, which exacerbates thermal stress at the interface.

Besides the influence of brittle intermetallic phase formation and CTE, the authors speculate that the shielding gas flow rate differences between SS316 and IN718 could potentially have an impact on the interfacial porosity formation, attributed to the deposition of spattering and welding plume. The lack of data on shielding gas flow rate at the interface provides no evidence of the influence of gas flow rate but could be found on monolithic materials of SS316[181] and IN718.[182]

Stainless steel/Cu alloy combinations are utilized in fields such as energy[55] and automotive,[49] leveraging the mechanical strength of SS and the high thermal conductivity of Cu. Figure 5 illustrates the interfacial microstructural characteristics of dissimilar SS/Cu materials with various Cu alloys.

A bimetallic SS316L/C18400 structure fabricated through MM-LPBF exhibited sporadic cracking (Figure 5B) on the SS side of the interface, with a transition width of 750 μm (Figure 5A).[141] These cracks were attributed to the thermal mismatch between SS and Cu, whereby Cu diffuses into austenitic grain boundaries of SS316L, exerting pressure and causing cracking. Optical microscopic images revealed SS-rich regions free of porosity or defects, while a considerable number of pores were observed on the Cu-rich region due to the high reflectivity and thermal conductivity of Cu (Figure 5C and D). EDS analysis revealed a good metallurgical bonding between SS316L and C18400. With the understanding of the interfacial characteristics of SS316L/C18400, the bimetallic structure of SS316L/C25400 could also be examined. Similarly, an SS316L/C25400/SS316L MMAM structure manufactured using MM-LPBF exhibited characteristics akin to the SS316L/C18400. Bai *et al.*[140] observed the formation of a few cracks at the transition region extending to the

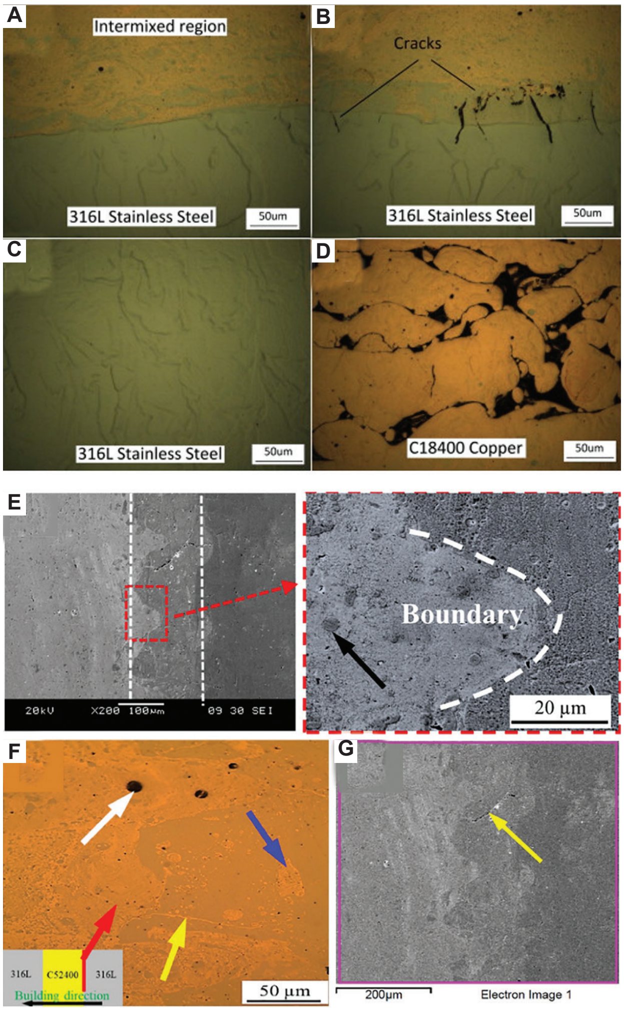

Figure 5. Interfacial meso- and microstructural characteristics of stainless steel and copper bimetallic alloys fabricated through multi-material-laser powder bed fusion. (A-D) SS316L/C18400[141] and (E-G) SS316L/C52400[140]. Scale bars: 20 µm, 50 µm, and 100 µm, magnifications: (E and G) 300×. Reprinted with permission from Liu *et al.*[141] (Copyright © 2014, Elsevier Inc.) and Bai *et al.*[140] (Copyright © 2020, Elsevier Inc.). The images reveal the interfacial characteristics associated with each copper alloy composition, highlighting variations in metallurgical bonding, porosity formation, elemental diffusion, and phase transformation.

SS316L-rich region, attributed to the high content of Cu (Figure 5E-G). Further analysis revealed that the cracks formed within the SS-rich region were visible from high-resolution optical microscopy (Figure 5F and G; indicated by the yellow arrows).

Extensive research on SS316L/CuSn10 bimetallic structures has concluded that good metallurgical bonding between SS/Cu is achievable.[58,139,142,183] The width of the transition zone between SS316L/CuSn10 and CuSn10/SS316L was about 400 µm and 160 µm, respectively, indicating a higher bonding strength on the SS316L/CuSn10 side compared to the CuSn10/SS316L side.[56] An irregular elliptical island-like heterogeneous phase appeared in both material-rich regions due to the high-energy laser beam penetrating through several layers to re-melt the solidified SS316L.[56,58,142] The rapid movement of the laser beam caused the molten pool to be unstable. However, CuSn10/SS316L exhibited fewer cracks than SS316L/CuSn10. The crack formation was attributed to liquid metal embrittlement, driven by differential elemental diffusion rates at high temperatures, consistent with the Kirkendall effect, similar to observations by Liu *et al.*[56] Similarly, in SS316L/C18400[141] and SS316L/C25400[56] bimetallic structures, cracks were observed at the transition region and extended toward the SS-rich region in both alloy combinations due to the high residual stress in SS316L owing to its low CTE. A similar behavior was observed in the SS316L/Cu/Ti-6Al-4V[123] MMAM structure using a Cu-alloy as an intermediate bonding layer (IBL).

From these studies, it is evident that in SS/Cu bimetallic structures, crack formation is primarily driven by dissimilar thermal and mechanical properties between metal alloys. Compared to SS/Ni bimetallic structures, which generally exhibited good metallurgical bonding, SS/Cu combinations were more prone to cracking, largely due to the significantly higher thermal conductivity of Cu relative to SS. In SS/Cu structures, cracks propagated in the Cu-rich region due to the deeper penetration of Cu into the SS alloy. Conversely, in Cu/SS bimetallic, a small amount of Cu penetrates the interface of SS316L, and a brittle Cu film with low strength is formed. In the subsequent cooling process, due to the difference in the thermophysical properties between Cu and SS, the degree of shrinkage between Cu and SS is not consistent due to high residual stress, resulting in thermal penetration cracking on the SS side.

In addition to the SS/Cu bimetallic structure, SS316L/Zr and SS410/Zr bimetallic structures exhibited vertical cracks during fabrication due to the differences in CTE and dissimilar thermal properties.[171] In contrast, SS316L/17-4PH structures displayed a smooth transition without intermetallic phase formation, attributed to the similarities in thermal conductivity and CTE and a narrow thermal heat gradient between the two materials.[147] Finally, SS316L/W bimetallic structures exhibited larger, irregular pores in the SS-rich region, which were closer to the transition region. These pores and cracks were formed due to inadequate process optimization, excess thermal stress gradient from high heat input from the molten pool, and mismatch of CTE values between the two materials.[148] From all the above miscellaneous studies, it was evident in SS316L/Zr, SS410/Zr, and SS316L/W that thermal properties such as thermal conductivity, CTE, and temperature gradient played a significant role in determining the metallurgical bonding between dissimilar materials.

3.2. Titanium-based bimetallic alloys

A Ti-6Al-4V/Ti-5Al-2.5Sn bimetallic structure, manufactured via MM-LDED and tested by Wei *et al.*,[151] exhibited high-quality metallurgical bonding, attributed to optimized deposition parameters. Throughout the entire specimen, defects such as pores, cracks, and lack of fusion were notably scarce, underscoring the efficacy of the employed parameters and the presence of extremely high thermal gradients along the build direction.[151] In addition, an EDS line scanning profile of the as-built specimen revealed an interdiffusion region spanning 70 μm at the interface, with the elemental composition transitioning from Tin (Sn)-dominant to Vanadium (V)-dominant. A strong Marangoni convection allowed the V elements to move downward and the Sn elements to move upward within the molten liquid. This well-interfacial bonding between dissimilar materials increased its strength compared to Ti-5Al-2.5Sn layers. The physical and thermal properties of Ti-6Al-4V and Ti-5Al-2.5Sn were consistent, which is evidently represented in the interface bonding, indicating a smooth transition of elements from one side to another. Although the elemental composition of both alloys is different, they produced a near-homogeneous martensitic microstructure due to the high cooling rate.

In contrast, the interface in a Ti-6Al-4V/SS410 bimetallic structure observed by Onuike *et al.*[154] exhibited a narrow (15 μm) transition region with numerous cracks perpendicular to the interface due to the immiscibility of SS and Ti alloy. Both materials were discerned by a thin layer of phase mixture (Figure 6A). To overcome the immiscibility of Ti-6Al-4V and SS410, niobium (Nb)[154] and Ni-chromium alloy (NiCr)[122] were used as an IBL to optimize the metallurgical bonding. Ti-6Al-4V/Nb/SS410 fabricated using MM-LDED showed a good metallurgical bonding with no cracks or de-bonding. Due to the Marangoni convection, an upward movement of elements such as Ti, V, and Nb into the SS410 layer was observed using EDS (Figure 6B). Notably, no brittle intermetallic phases (e.g., FeTi and Fe_2Ti) were detected at the IBL, emphasizing the role of Nb as an intermediate bond and diffusion barrier layer. This highlights its effectiveness in mitigating brittle intermediate phases and reducing thermal stresses.

Conversely, in Ti-6Al-4V/NiCr/SS410, a significant number of pores were observed at the interface,

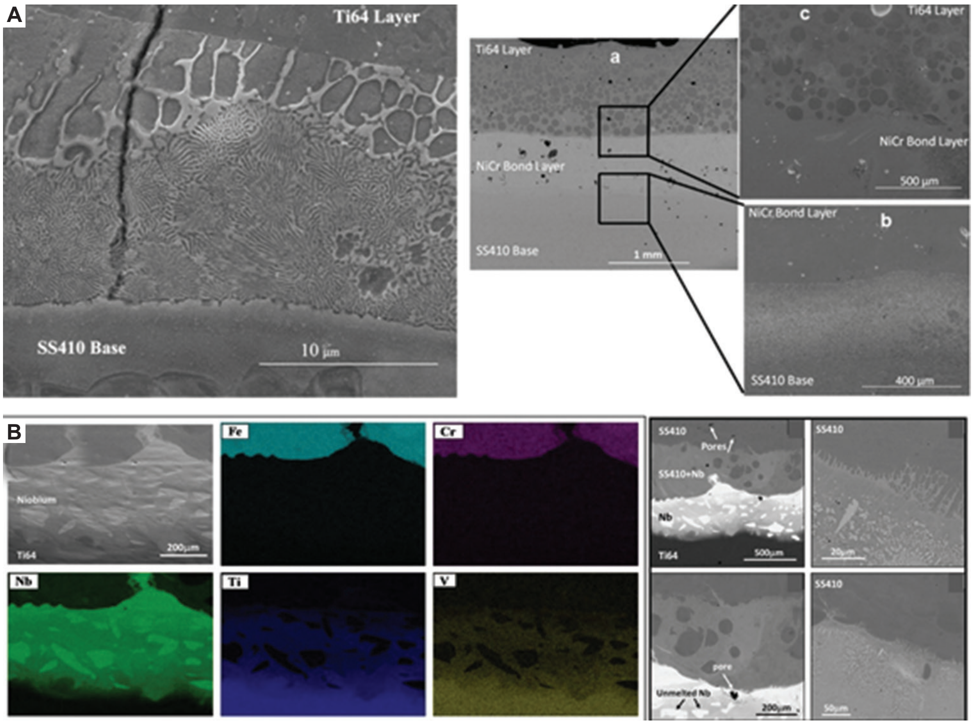

Figure 6. Interfacial characteristics of titanium (Ti)-based bimetallic structures. These structures were fabricated using (A) Ti-6Al-4V/NiCr/SS410 MM-laser-directed energy deposition (LDED)[122] and (B) Ti-6Al-4V/Nb/SS410 MM-LDED.[154] The images reveal the interfacial evolution and metallurgical bonding behavior across the Ti-base alloy combination with interlayer, with particular emphasis on elemental transition, interlayer strategies, crack formation, and phase formation. Scale bars: 10 μm, 50 μm, 200 μm, 400 μm, 500 μm, and 0.5 mm. Reprinted with permission from Sahasrabudhe *et al.*[122] (Copyright © 2014, Elsevier B.V.) and Onuike and Bandyopadhyay[156] (Copyright © 2018 Elsevier B.V.).

attributed to the inadequate energy input during NiCr layer deposition.[122] Nevertheless, Ti-6Al-4V/NiCr has amalgamated and formed a strong overall bonding, as evidenced by the presence of light and darker circles, as observed in Figure 6A. The disparity in thermal properties between Nb and NiCr contributes to the observed porosity in Ti-6Al-4V/NiCr/SS410 but not in Ti-6Al-4V/Nb/SS410. This underscores the importance of material compatibility and thermal characteristics when selecting intermediate materials. Another interesting investigation looked at the effect of transition joints on the interfacial characteristics in Ti-6Al-4V/TiC. Using dual-material transition joints, two distinct joints - (1) Butt joint and (2) interlock joints illustrated a crack-free interfacial bonding.[150] These findings shed light on the effectiveness of different joint configurations in achieving a strong and seamless bond, providing valuable insights toward the design and fabrication of dual-material transition applications. Owing to the similar physical and thermal properties of Ti-6Al-4V and TiC, the resulting bonds exhibited defect-free surfaces and microstructural characteristics resembling those observed in Ti-6Al-4V/Ti-5Al-2.5Sn joints.

3.3. Nickel-based bimetallic alloys

Bimetallic structures of IN718/SS316L[159] and IN625/SS316L,[132] fabricated using MM-LPBF and MMLDED, respectively, exhibited similar wavy characteristics at the interface. These distinctive characteristics are caused by the high degree of molten pool banding, compared to the interface between SS316L/IN625, as explained in Section 3.1 (Figure 4C, D, and F). The interface exhibited epitaxial growth, implying that irregular-shaped coarse grains are observed at the transition/composite zone. At the IN718/SS316L interface, Duval-Chaneac *et al.*[159] observed a minor crack formed due to liquation cracking (Figure 7A). Liquation cracking occurs due to the rapid solidification of alloys with high alloying content, which widens the solidification range and promotes the formation of liquation cracks. Notably, both Ni-based systems exhibited interfacial cracks resulting from solidification-induced stresses and the absence of compensating melt flow. In contrast, a Ni/Cu bimetallic structure demonstrated poor metallurgical bonding, with strong interfacial adhesion between the two alloys.[184] The high thermal conductivity of Cu allowed deeper penetration into the Ni-based substrate, promoting diffusion and metallurgical integration. Onuike *et al.*[184] examined IN718/GRCop-48 bimetallic structure fabricated using LDED and observed poor interfacial bonding, characterized by metal lump formation and the balling phenomenon. This was attributed to the extreme differences in thermal properties and poor diffusion compatibility. To address this, a compositional gradient layer was introduced, which facilitated improved bonding by gradually bridging the thermal and physical mismatches between the dissimilar alloys. This approach highlights the effectiveness of using a gradient transition layer in overcoming bonding challenges in systems with significant property disparities.

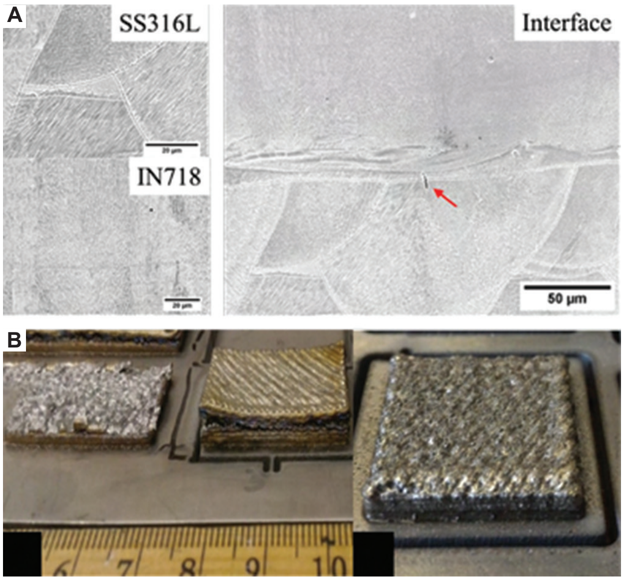

Figure 7. Interfacial characteristics of nickel (Ni)-based bimetallic alloys fabricated through multi-material laser powder bed fusion (MM-LPBF) and mixed-material laser-directed energy deposition (MM-LDED). (A) IN718/SS316L produced by MM-LPBF[159] and (B) IN718/Ti-6Al-4V produced by MM-LDED.[156] The images reveal minor crack formation, metal lump formation, and delamination at the interface across different material combinations and process techniques. Scale bars: 10 μm and 50 μm. Reprinted with permission from Onuike and Bandyopadhyay[156] (Copyright © 2018 Elsevier B.V.) and Duval-Chaneac *et al.*[159] (Copyright © 2021 Elsevier Ltd.).

Similar to previous studies, the interfacial characteristics of IN718/Ti-6Al-4V[156] and NiTi/Ti-6Al-4V[52] were observed to form lateral cracks with no visible crack formation. The lateral crack formation at the interface between IN718/Ti-6Al-4V was due to the larger dissimilarities in CTE and immiscibility, which inhibit bonding; the crack was later overcome by introducing a vanadium-carbide compositional bonding layer (Figure 7B). Vanadium-carbide serves as a bonding link for dissimilar materials and minimizes the formation of brittle intermetallic phases.[156] However, due to the close range in thermal properties between NiTi and Ti-6Al-4V and NiTi's secondary dominant composition being Ti-element, the interface exhibited good metallurgical bonding. Bartolomeu *et al.*[52] indicated that, due to the MM-LPBF fabrication strategy (removing excess powder before adding Ti-6Al-4V) along with adequate process parameters, the number of cracks was reduced, and good metallurgical bonding was achieved.

Lastly, a Ni-Al alloy dissimilar material composition was studied by Liu and Dupont.[185] They observed high solidification and sub-solidus cracking susceptibility, as well as porosity formation. The porosity formation was caused by the use of water-atomized Ni rather than gas-atomized Ni, and the cracks were formed due to the combined effect of high thermal stress and brittleness of the intermetallic. Subsolidus cracking and porosity were formed at the interface due to differences in thermal properties.

3.4. Ferrous-, aluminum-, and copper-based bimetallic alloys

In the Fe/SS (P21/SS316L)[166] bimetallic structure fabricated using MM-LDED, a good metallurgical bonding without cracks, pores, or unmelted particles was observed at the interface due to the rapid cooling and steep thermal gradient. The P21 morphology consisted of diminutive austenite and mostly of martensite. However, the interface of H13 (ferrous alloy)/Cu was observed to be discrete compared to Fe/SS, where micro-cracks and pores were observed even though Cu was able to adhere to H13 (Figure 8A and B). The cracks were formed due to the solidification cracks and higher CTE variation between H13 and Cu and propagated perpendicularly towards the H13 region.[167] However, in the 18Ni300/CuSn10 bimetallic structure, the interface appeared relatively loose, with small pores and interfacial mixing of α-Fe and α-Cu phases, as evidenced by scanning electron microscopy and EDS mapping. In contrast, in the CrMn/MS1 (ferrous/ferrous alloy) bimetallic structure, the interface exhibited a good metallurgical bonding with no cracks or pores, attributed to its similar thermal properties. At higher magnification, a curved solidification characteristic was visible due to the Marangoni convection (Figure 8C-F).[169]

In studies where Al was the base material, Wang *et al.*[172] and Sing *et al.*[175] investigated Al-12Si/Al-Cu-Mg-Si and Al-12Si/C18400, respectively. In Al-12Si/Al-Cu-Mg-Si, the interface exhibited good metallurgical bonding with no pores and few defects on the base material due to a similarity in their thermal properties. However, the Al-12Si/C18400 interface exhibited cracks compared to the Al-12Si/Al-Cu-Mg-Si due to the dissimilarities in CTE, resulting in uneven expansion and contraction during solidification.[186] However, a good metallurgical bonding was indicated with a transition region of 200 μm in both cases.

Both bimetallic structures Cu-Cr/07Cr15Ni5[178] and T2 (Cu alloy)/MS1[179] exhibited defects such as cracks and pores due to the high thermal conductivity of Cu-Cr, insufficient energy applied during manufacturing, and variations in process parameters. In the bimetallic structure of Cu/MS1, specimens were fabricated by Tan *et al.*[179] using LPBF at different scanning speeds (500 – 1,250 mm/s). At low scan speeds (500 – 950 mm/s), the interface exhibited good metallurgical bonding. However, at high scan speeds (1,100 and 1,250 mm/s), cracks due to residual stress and pores due to lack of fusion were observed (Figure 8G and H). High thermal conductive Cu enhanced the metallurgical bonding mechanism through Marangoni convection, contributing toward interfacial elemental diffusion and bonding strength.

4. Mechanical characteristics of MMAM structures

Understanding the mechanical properties of an MM composition is crucial for comprehending its characteristics. With the potential of manufacturing MM samples through AM methods, conducting mechanical testing would expand researchers' understanding of the primary, interfacial, and secondary material properties. The evaluation of the MMAM structure properties will support the qualification of components fabricated with MMs based on the target regime or environments that the materials are expected to experience.

This section explores the mechanical properties of MMAM components, organized according to the types of mechanical tests performed on MM components. These tests provide crucial insights into the performance and integrity of the interface between dissimilar materials. The mechanical evaluations include hardness (Section 4.1), tensile testing (Section 4.2), flexural strength (Section 4.3), compression test (Section 4.4), fatigue (Section 4.5), and miscellaneous testing (Section 4.6), including wear performance, thermal diffusivity, and shear bond test. Table 2 provides an overview of all mechanical testing conducted on MMAM to date, categorizing them by microhardness, tensile, flexural, and miscellaneous tests and further categorizing them according to the base material. As shown in Figure 10, microhardness and UTS are the most commonly employed techniques to evaluate the interfacial performance in MM components.

4.1. Micro-hardness/micro-indentation

Hardness testing is often conducted on MMAM specimens as a preliminary test, following the ASTM standard E384[187] for small- or large-scale specimens. Hardness testing provides data about the material's resistance to deformation, indentation, scratching, or penetration. From the empirical studies collected (Table 2), hardness testing is one of the most widely adopted testing methods

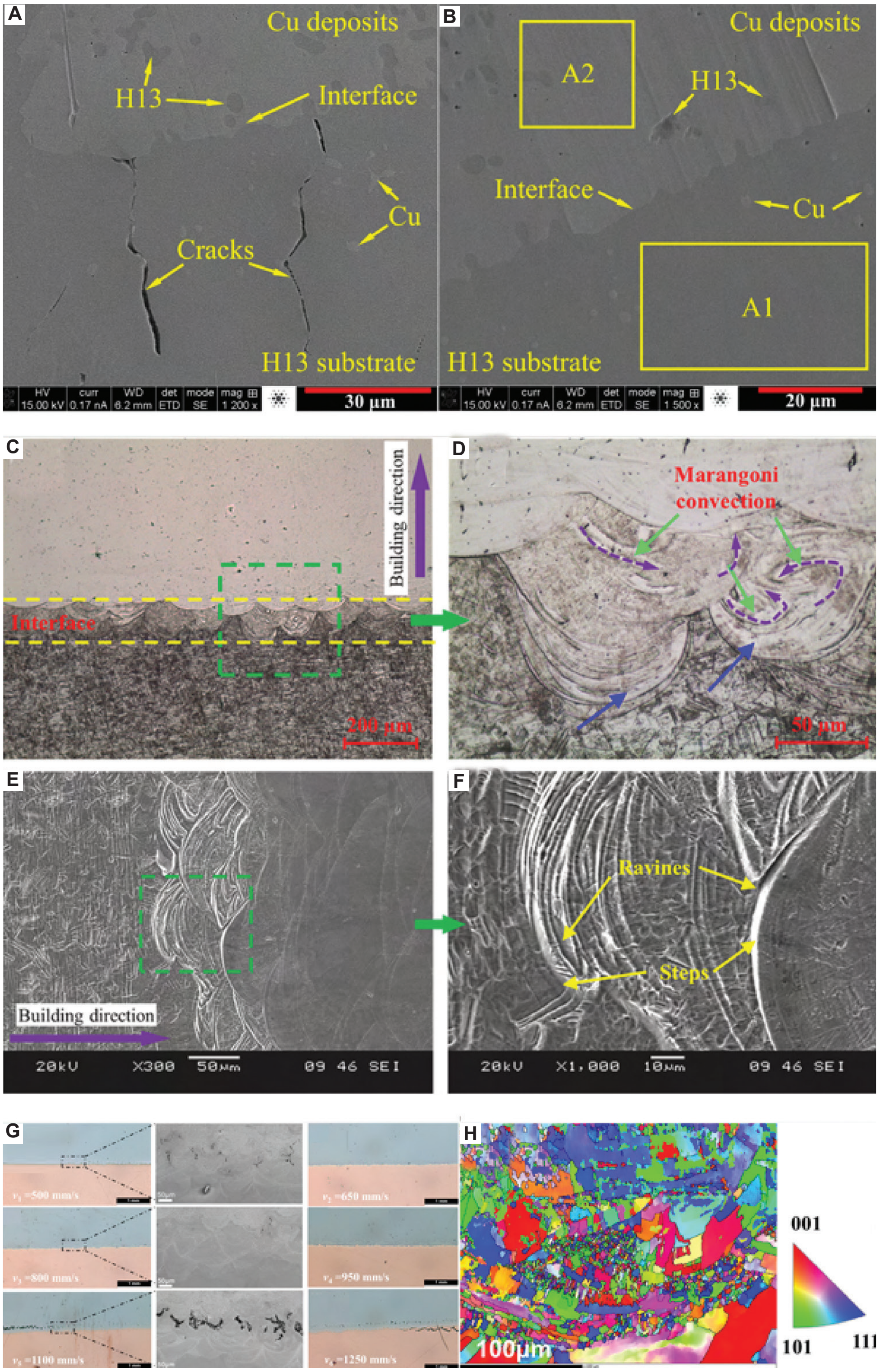

Figure 8. Interfacial characteristics of iron- and copper (Cu)-based bimetallic structures fabricated through mixed-material laser powder bed fusion (MM-LPBF) and mixed-material laser-directed energy deposition (MMLDED). (A and B) H13/pure Cu produced by MM-LDED,[167] (C-F) CrMn/MS1 produced by MM-LPBF,[169] and (G and H) T2/MS1 produced by MM-LPBF.[179] The images reveal the interfacial morphology, metallurgical bonding, elemental diffusion, and microstructural characteristics. Scale bars: 10 μm, 20 μm, 30 μm, 50 μm, 100 μm, and 200 μm, magnifications: (A) 1200×, (B) 1500×, (E) 300×, (F) 1000×. Reprinted with permission from Zhang *et al.*[167] (Copyright © 2020 Elsevier B.V.), Bai *et al.*[169] (Copyright © 2020 Elsevier B.V.), and Tan *et al.*[179] (Copyright © 2018 Elsevier Ltd.).

Table 2. Mechanical testing of each bimetallic combination

Deposited material Base material	Titanium alloy	Stainless steel alloy	Nickel alloy	Aluminum alloy	Copper alloy	Ferrous alloy	Miscellaneous alloy
Stainless steel alloy	A, B[123]		A[126,127,129,130], (A, B)[131,133,157]		A[56,128,140], (A, B, C, E, F_{com})[58], (A, C)[141], (A, B, C, E)[142], (A, B)[187]	(A, F_{com})[144,166]	(A, C)[148]
Titanium alloy	(A, F_{com})[188], (A, B)[189,151], (A) [122]	E[154]	A[155]		A[57]		
Nickel alloy	(A, F_{Shear})[52], (A)[156]	(B) [131], (A, F_{wear})[158], (A, F_{fat})[159], (A)[160]			(A)[47], (A, $F_{T\,herm}$)[184]		
Ferrous alloy		(F_{com})[166], (B, D, F_{Fat})[170]		A[190]	(B, E)[179], (A, C)[167]	(A, B) [169], (B, D, F_{Fat})[170]	
Aluminum alloy				(A, C)[172,173]	(A, C, E)[179], (A, E)[175]	A [167]	A[177]
Copper alloy			A, B, F_{com} [176]			A[167]	

Note: The mechanical testing conducted on each bimetallic combination is denoted alphabetically. For detailed information on the alloy composition in a specific reference within the multi-material additive manufacturing combination and specific experimental procedures, refer to Table A2.
Abbreviations: A: Hardness; B: Tensile strength (||); C: Tensile strength (=); D: Flexural strength (||); E: Flexural strength (=); F_{com}: Compression; F_{fat}: Fatigue; F_{Shear}: Bond shear; F_{wear}: Wear performance; $F_{T\,herm}$: Thermal diffusivity.

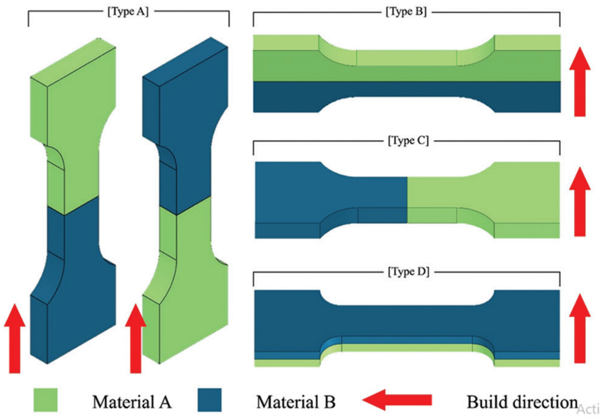

Figure 9. Build orientation of multi-material additive manufacturing samples that are used in the literature. Type A: Two distinctive materials stacked vertically. The dissimilar materials meet at the horizontal interface. Type B: Two material systems joined side by side along the vertical interface. Type C: Two materials layered on top of each other horizontally, forming a horizontal interface. Type D: Similar to Type C, with the horizontal interface at the middle of the thickness of the specimen

as it provides valuable insight into the mechanical integrity and performance of the components.

In bimetallic structures such as SS316L/Ni[126,127,129,131,157] and Ni/SS316L,[131,158-160] the interface region exhibits a smooth transition from higher to lower hardness level or vice versa, reflecting the changes from one material to another. The literature revealed a smooth gradient in hardness across the interface, with bulk-Ni alloys such as IN718 and IN625 exhibiting a hardness level of 304±16 HV and 260±13 HV, respectively. Feenstra *et al.*[157] noted that increasing the laser power resulted in a decrease in hardness, particularly at the interface region. Interestingly, the incorporation of carbon fiber IBL in IN718/SS316L MMAM structures resulted in a 1.5 to 2-fold increase in microhardness relative to the monolithic materials. The increase in hardness is attributed to the formation of chromium-rich carbides at the interface.[158] Beyond the general observation of a gradual hardness transition, both laser power and incorporation of an IBL have been shown to significantly influence the hardness level. These trends in SS/Ni structures offer a useful comparison to other bimetallic structures, such as SS/Cu, which are discussed in the following sections.

Similarly, the MMAM structures composed of SS316L/Cu[139] or Cu/SS316L[56] exhibited similar hardness transitional behavior to that of SS316L/Ni. Specifically, in SS316L/Cu, hardness levels descend from 240 ± 37 HV (SS316L) to 156 ± 4 HV, 181 HV, and 74 HV for CuSn10, C52400, and C18400, respectively (Figure 10A). A reverse trend is noted when transitioning from Cu to SS316L (Figure 10B). A smooth transition between SS and Cu alloys was revealed, attributed to the variation in Fe and Cu content in the melt pool and grain refinement at the interface. Supporting these observations, Meyer *et al.*[139] Liu *et al.*[139] observed a higher hardness level of 248.6 ± 22.5 HV in the diffusion zone when compared to the monolithic material region of SS316L and CuSn10. This increase is attributed to the presence of highly refined grains, which hinder dislocation movements and enhance microhardness, in addition to strain hardening induced by micro-strains.

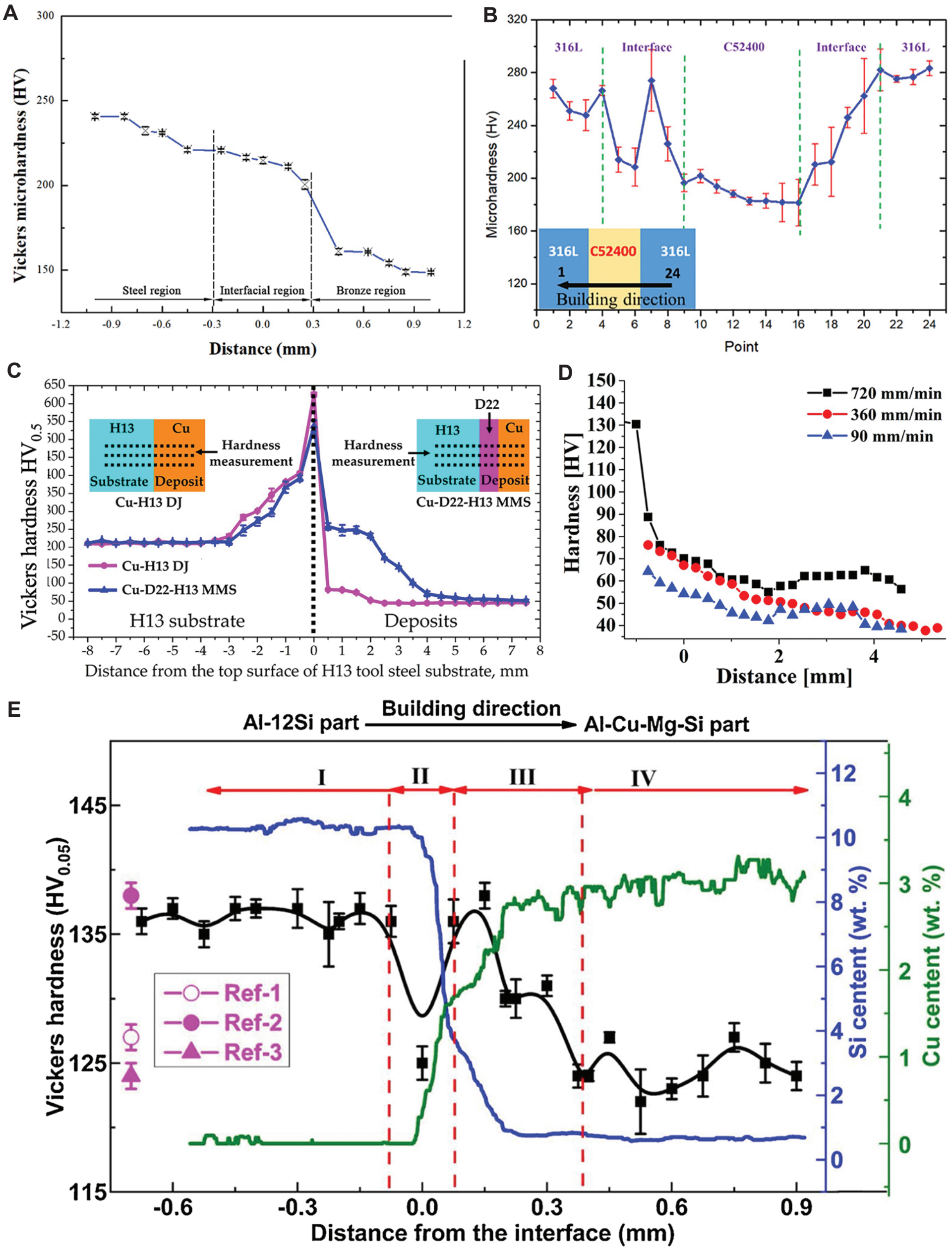

Figure 10. Representative hardness profile of various bimetallic structures fabricated through multi-material laser powder bed fusion (MM-LPBF) and multi-material laser-directed energy deposition (MM-LDED): (A) SS316L/CuSn10 (MM-LPBF);[58] (B) SS316L/C25400/SS316L (MM-LPBF);[56] (C)H13/Cu (MM-LDED);[167] (D) Al/W (MM- LDED);[177] (E) Al12Si/Al3.5Cu1.5Mg1Si (MM-LPBF).[172] These profiles illustrate the hardness gradient across interfacial regions, capturing effects due to material mismatch, processing parameters, and interlayer presence. The hardness data represent transitions across interfaces and highlight the influence of process conditions, elemental diffusion, and interlayers on local mechanical response.

The hardness level transition in the bimetallic structure of SS/Cu revealed that the grain refinement, elemental diffusion, and strain hardening played a significant role in the hardness of the components.

Extending this trend to SS-based MMAM structure, the interface region of SS316L/P21[141] and SS316L/17-4PH[147] revealed a smooth transition of hardness. This behavior was attributed to residual stresses and the finer microstructure inherent to these combinations of dissimilar materials. The bulk hardness values of P21 and 17-4PH were reported as 330 HV and 312 HV, respectively, while the interface between SS316L/17-4PH and SS316L/P21 exhibited an average hardness of 232±7 HV. Unlike SS/Fe MMAM structures, the interfacial region of SS316L/tungsten exhibited a higher hardness of 543±3.7 HV compared to the SS316L and tungsten-rich region, which exhibited 392±1.6 HV and 411.7±3.3 HV, respectively.[148]

This increase in hardness is due to the secondary phases like Fe_2W, Fe_3W_3C, and Fe_6W_6 which disperse high levels of hardness due to the presence of brittle and intermetallic compound (IMC) phases. In bimetallic structures with SS316L as the substrate, it was revealed that the hardness mostly exhibited a smooth transition, besides cases having a poor interfacial characteristic (discussed in Section 3), which has influenced the hardness at the interface by forming intermetallic phases that have higher hardness values.

A similar trend in interfacial hardening has been observed in other combinations of MMAM structures. Wei *et al.*[151] studied the Ti-5Al-2.5Sn/Ti-6Al-4V structures and observed a smooth transition at the interface for both as-deposited and annealed specimens, noting a drop in overall hardness of the specimen due to the softening effect provided by the "$\alpha' \rightarrow \alpha$" recrystallization process. Similar to the SS316/CF/IN718 structure, the influence of the IBL in Ti-6Al-4V/SS410 was also significant—with the introduction of IBL, such as Nb and NiCr—exhibiting distinct effects on interfacial hardness. The Ti-6Al-4V/Nb/SS410 MMAM structures exhibited a smooth transition up to the interface with SS410, where the hardness value dropped due to the element diffusion and heat-affected zone.[154] However, in Ti-6Al-4V/NiCr/SS410, the hardness at the interface was observed to be smoother compared to the specimens with an Nb IBL.[122] In a Ti/Cu MM composition, it was observed that the hardness of the interface region increases with increasing Cu content, primarily due to the formation of hard IMCs and solid solution strengthening.[123] The transition through the interface in the Ti/Ti and Ti/IBL/SS bimetallic structure revealed a smooth transition in hardness. In the Ti/Ti bimetallic structure, an overall drop in hardness was observed due to annealing, while in the Ti/IBL/SS bimetallic structure, the presence of IBL influenced the interfacial region to form a smoother transition with no abnormalities.

Overall, these studies highlight that the selection of IBL and constituent materials in MMAM structures critically governs the interfacial hardness profile, with smoother transitions and tailored mechanical responses achievable through strategic material design and thermal management.

Similar to the earlier findings, in the MMAM structures of NiTi/Ti-6Al-4V[52] and IN718/Ti-6Al-4V,[154] a smooth transition with no abrupt changes at the interface was observed during transitioning. In IN718/Ti-6Al-4V, the diffusion of chromium carbide particles into the IN718 led to the formation of the Cr_3C_2 phase, which resulted in higher hardness at the interface compared to the bulk materials. Similarly, the IN718/Cu MMAM structures fabricated using MM-LPBF and MM-LDED revealed enhanced interface hardness. In MM-LPBF, this was attributed to rapid solidification effects from the localized laser remelting.[47,184] However, the MM-LDED study did not provide detailed information on the interface or the transition in hardness. The studies on Ni/Ti and Ni/Cu revealed a smooth transition similar to the earlier bimetallic structure observation. In IN718/Ti-6Al-4V, the formation of intermetallic phases resulted in superior hardness than the bulk material. These findings further affirm that in MMAM structures, smooth interfacial transitions can be achieved even between highly dissimilar materials, with interfacial hardening predominantly influenced by elemental diffusion, intermetallic formation, and process-specific thermal conditions.

In contrast, the hardness at the interface of H13/Cu did not exhibit a smooth transition. Instead, it exhibited a peak hardness at the interface attributed to the increased laser hardening, followed by a sudden drop, which was attributed to poor diffusion of elements (Figure 10C).[167] Similarly, in CrMn/MS1 bimetallic structures, a mostly smooth transition was observed, but with a sudden hardness increase at the interface, resulting from the influence of the presence of MS1.[169] Overall, in the SS316L/P21, SS316L/17-4PH, and CrMn/MS1 MMAM structures, a smooth transition from harder to weaker material was revealed, though CrMn/MS1 uniquely exhibited a localized hardness increase at the interface. In contrast, the H13/Cu bimetallic structure interface deviated significantly from this trend, showing a rapid hardness change due to laser hardening in the deposited H13 region and a subsequent drop caused by insufficient interdiffusion.

Additional insight into hardness behavior across dissimilar materials was observed in Al-based bimetallic structures. The hardness factors of Al/tungsten, AlSi10Mg/C18400, and Al12Si/Al3.5Cu1.5Mg1Si MMAM structures were analyzed extensively,[172,175] revealing unique behaviors at the interface and during transitioning. In the Al/tungsten bimetallic structure, a smooth transition from tungsten (high hardness) to Al (low hardness) was observed.[177] In addition, the hardness throughout the sample increased as the scanning speed was reduced (Figure 10D). In AlSi10Mg/C18400, a gradual hardness decrease was observed from the Al-rich to Cu-rich regions, with anomalous hardness values exhibited at the interface. Such anomalous hardness values are due to the presence of brittle intermetallic Al_2Cu, which results in hardness ranges of 400 – 600 HV.[175] In Al12Si/Al3.5Cu1.5Mg1Si MMAM structures, the interfacial region showed a sudden drop in hardness moving away from Al12Si.[172] From the silicon-dominant region (zone II) to the Cu-dominant region (zone III) (Figure 10E), the hardness increased significantly. This was attributed to the microstructural shift from cellular to granular morphology, accompanied by the development of a <001> fiber texture. Beyond zone III, however, the hardness decreased again due to grain growth and increased silicon content.

4.2. Tensile strength

Analyzing the tensile strength of MMs is necessary to determine the tensile characteristics at the interface and the bond between the dissimilar metals based on the deposition order and design. This section delves into the tensile properties of MMAM structures, where the dissimilar material deposition configurations are classified with respect to the build direction as Types A, B, C, and D, as shown in Figure 9. For the ease of the readers, the discussion follows the same order as Section 3, beginning with SS-based to Cu-based bimetallic structures.

The tensile strength of SS/Ni bimetallic structures has been evaluated using different compositions of Ni-based alloys, such as IN625[133,157] and IN718.[131] For SS316/IN625 structures fabricated in the Type-A orientation, Feenstra *et al.*[157] and Ahsan *et al.*[133] used MM-LDED and MM-WAAM, respectively. In both cases, the UTS was found to be greater than that of wrought and as-built SS316, with the bimetallic structures exhibiting a UTS of 577 ± 16 MPa. Interestingly, elongation values ranged from 10 – 15% in MM-LDED to 40% in MM-WAAM. Both studies reported dimple-like features on the fracture surfaces, suggesting ductile failure through micro-void coalescence. For SS316L/IN718 fabricated in Type-A orientation using MM-LPBF, UTS and elongation values were 596 ± 10 MPa and 28.1%, respectively—higher UTS than AM-SS316 but lower elongation than AM-IN718. Post-fracture analysis of the fracture surface revealed similar features to SS316/IN625, with dimple-like characteristics leading to a mixed-mode fracture, where the ductile mode was prominent. In both bimetallic structures, UTS values exhibited similar trends with a variation of 19 ± 19 MPa, and elongation remained within a comparable range. The root cause of failure in both cases was the formation of micro-voids at the interface, leading to ductile fracture and lower UTS compared to monolithic Ni-based alloys. Mitigating interfacial micro-voids could potentially enhance the mechanical performance of bimetallic structures.

Extending the evaluation to SS/Cu bimetallic structures, researchers have investigated various combinations fabricated using Cu alloys such as CuSn10[58,139,183] and C18400.[141] Chen *et al.*[58] manufactured SS316L/CuSn10 specimens in both Type-A and Type-D orientations. In both cases, the tensile strength and elongation were lower than those of bulk SS316L, with UTS values of 423.3 ± 30.2 MPa and 459.1 ± 8 MPa, and elongation values of 4.6 ± 0.9% and 10.5 ± 1.7%, respectively. Type-D specimens exhibited slightly higher UTS and approximately 6% greater elongation than Type-A specimens (Figure 11A). Fractography revealed distinct fracture modes: Type-A specimens exhibited cleavage fracture (a brittle transgranular mode) at the interfacial layer, attributed to unmelted SS316 powder particles, whereas Type-D specimens demonstrated a mixed mode of transgranular and intergranular fracture, with brittle fractures concentrated at the fusion zone.

Liu *et al.*[183] reported similar trends for Type-A orientation, although they observed lower tensile strength than that reported by Chen *et al.*,[58] primarily due to the presence of pores and interfacial cracks. A comparative study between LPBF and laser-welded structures indicated that LPBF showed higher tensile stress, attributed to finer grain structures formed under higher cooling rates.[139] Compared to SS316L/CuSn10,[139] the tensile strength of SS316L/C18400 in Type-D orientation was lower (310 ± 18 MPa. However, unlike in previous SS/Cu bimetallic systems, the fracture occurred on the Cu-side (the weaker material), indicating a well-formed metallurgical bond. Between CuSn10 and C18400, the latter showed improved bonding with SS316L, likely due to the lower reactivity of Fe–Cr compared to Fe–Sn. The Fe–Sn system is prone to form brittle intermetallic phases such as $FeSn_2$. In addition, Type-D orientation marginally performed better than Type-A, which may be attributed to the larger bonding area of Type-D.

Extending beyond Cu-based bimetallic, SS316L has also been combined with dissimilar materials such as W[148] and Ti-6Al-4V,[123] yielding varied interfacial characteristics. In MM-LPBF-fabricated SS316L/W (Type-D) structures, tensile strength increased from 239.7 MPa to 257.4 MPa after heat treatment, while elongation improved significantly from 5.3% to 17%.[148] This improvement was attributed to the transformation of the brittle fracture mode to a more ductile one, driven by the formation of Fe_7W_6 near the interface—an inherently hard and brittle phase. Fractures typically initiated on the W side of the interface. For SS316L/Ti-6Al-4V (Type-A) MM-LPBF structures, in which a Cu-alloy was used as an IBL, the scanning speed was a key parameter. Tey *et al.*[123] observed that specimens built at 650 mm/s exhibited higher tensile strength and better bonding than those built at 350 mm/s.

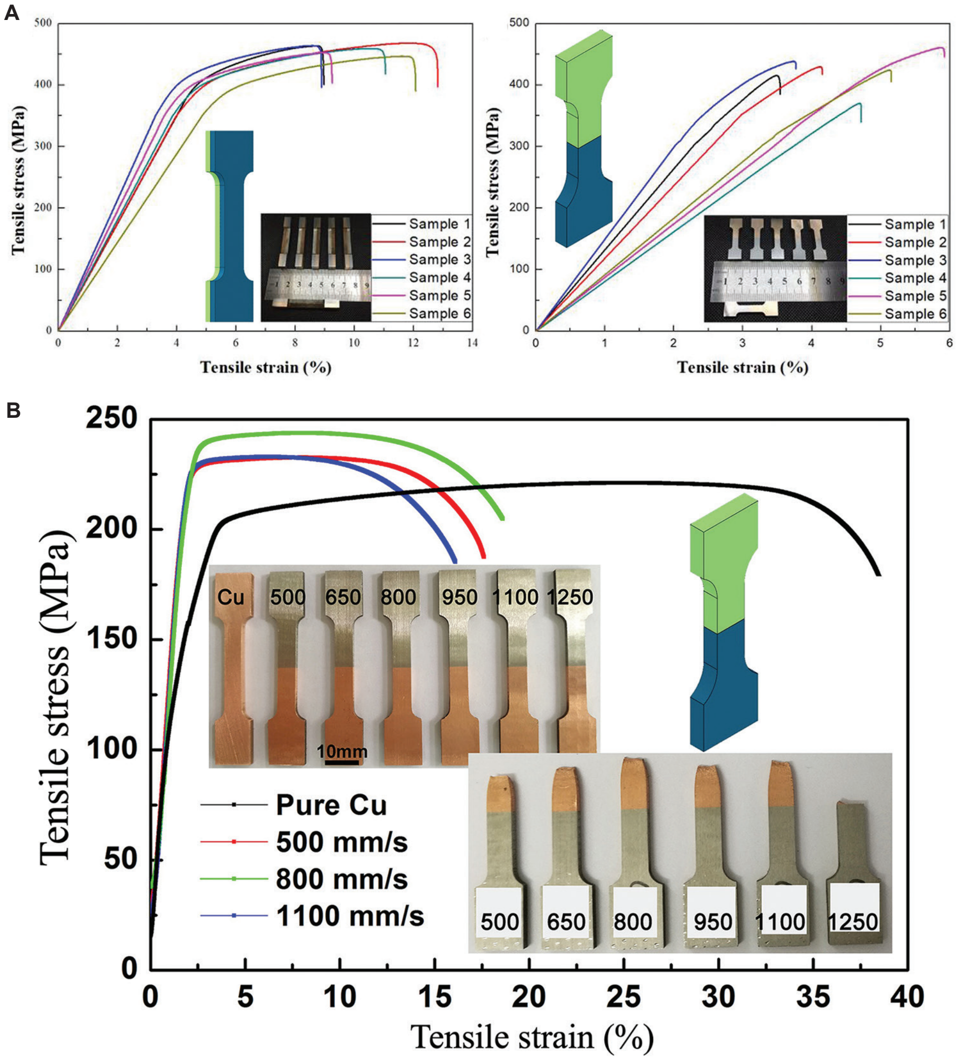

Figure 11. Quasi-static tensile stress–strain response of selected bimetallic structures fabricated throughmulti-material laser powder bed fusion: (A) SS316L/CuSn10;[58] and (B) MS1/Cu;[179] and (C) Ti-5Al-2.5Sn/Ti-6Al-4V.[151] The graphs highlight mechanical behavior across bimetallic interfaces, including differences in strength, ductility, and elongation. A schematic representation of the build orientation is also provided, consistent with that in Figure 9.

This resulted in a predominantly ductile fracture mode, in contrast to the brittle failure observed in lower-speed builds. In the above-mentioned MM-LPBF structures, the presence of defects and porosity evidently contributed to premature failure compared to the bulk materials. In both SS316L/W and SS316L/Ti-6Al-4V systems, characteristics such as heat treatment and processing parameters played a critical role in determining tensile behavior. These improvements were largely attributed to the removal of brittle IMCs and the relief of through-thickness residual stresses. Elimination of IMCs facilitated a transition from brittle to ductile fracture modes in both systems.

Although extensive research has been conducted on SS-based bimetallic structures, Ti-based bimetallics have also gained attention for their tensile strength. The tensile strength of Ti-5Al-2.5Sn/Ti-6Al-4V (Type-A) in as-deposited specimens reached a UTS of 1,034 MPa and an elongation of 4%, which is lower than that of forged Ti-alloys—primarily due to the formation of martensite microstructure.[151] Similar to the SS316/W system,[148] heat treatment increased elongation by 10%, due to the decomposition of the martensite phase, which led to a significant improvement in the strength–ductility balance. Compared to forged and AM monolithic materials, the bimetallic UTS exceeded that of forged alloys but remained lower than their AM counterparts, whereas elongation showed the opposite trend. Fractography analysis of the as-deposited bimetallic revealed that the fracture occurred on the To-5Al-2.5Sn side, due to its lower hardness compared to Ti-6Al-4V. This observation is validated by the hardness data presented earlier in Section 3.2.

MS1/Cu (Type-A)[179] and CrMn/MS1 (Type-A)[169] bimetallic structures outperformed the weaker constituent materials when compared to the earlier examples. In the MS1/Cu system, specimens fabricated at various scanning speeds showed similar UTS and elongation, except for the one built at 1,250 mm/s. At this higher scanning speed, a fracture occurred at the interface rather than on the Cu side, which had been the fracture location in all other specimens (Figure 11B). As previously discussed in Section 3.1 (Figure 8G), the MS1/Cu interface at low scanning speeds exhibited good metallurgical bonding due to enhanced thermal conductivity and Marangoni convection. These effects, influenced by Cu and Fe dissolution, contributed to the solid-solution strengthening of the Cu at the interface. In the CrMn/MS1 bimetallic structure, specimens exhibited slightly higher tensile strength compared to wrought CrMn, but lower than AM MS1. The fracture occurred on the CrMn side, indicating good metallurgical bonding. As with earlier observations, tensile strength and elongation were influenced by process parameters, indicating that optimal scanning conditions can promote ideal metallurgical bonding. Notably, CrMn/MS1 exhibited better tensile strength than wrought CrMn due to its improved bonding. Interestingly, bimetallic structures composed of the same alloy system but with different compositions (e.g., Ti-5Al-2.5Sn/Ti-6Al-4V) demonstrated better tensile behavior than the weaker monolithic constituent. This could be attributed to good metallurgical bonding and a defect-free interface.

Similar to the other same-alloy bimetallic structures, the AlSi10Mg/C18400 (Type-D) specimen exhibited higher tensile strength than C18400, but significantly lower than AlSi10Mg.[175] Failure predominantly occurred on the Cu-rich side, reinforcing the notion that interfacial bonding between Al and Cu is stronger than the bonding within the Cu-rich region itself. Fractographic analysis revealed a mixed brittle and ductile fracture mode, with ductile features dominating. This was influenced by the presence of unmelted particles on the Cu side of the fracture surface, which acted as stress concentrators and initiated failure. Similarly, tensile testing of Al12Si/Al3.5Cu1.5Mg1Si (Type-A) revealed a higher YS of 267 ± 10 MPa compared to as-built LPBF bulk counterparts. However, the UTS was lower than that of the bulk materials due to differences in microstructure.[172] Fractographic analysis revealed a brittle fracture mode approximately 200 μm from the interface on the Al12Si side, indicating good metallurgical bonding accompanied by localized embrittlement. Finally, for the Al6060/Al5087 (Type-A) bimetallic structure fabricated using MM-WAAM in the longitudinal direction, Hauser *et al.*[173] reported that the YS of as-built monolithic Al6060 was lower, and that of as-built monolithic Al5087 was higher than that of the bimetallic counterpart. Similar trends were observed for UTS values. Upon heat treatment, all specimens—including the bimetallic—experienced improved YS and UTS as expected. The UTS of the heat-treated bimetallic structure was comparable to that of Al6060 and slightly lower than that of Al5087, confirming the beneficial influence of post-processing on mechanical performance. Consistent with earlier observations, porosity and defects negatively influenced mechanical properties in Al/Cu bimetallic structures. In contrast, Al/Al bimetallics, similar to other same-element combinations (e.g., CrMn/MS1-Fe/Fe and Ti-5Al-2.5Sn/Ti-6Al-4V–Ti/Ti), exhibited good metallurgical bonding and superior mechanical performance compared to wrought material or monolithic as-built materials.

4.3. Flexural strength

Compared to other mechanical properties, the flexural strength of MMAM structures has received relatively limited attention. Among the available literature, ferrous-based MMAM structures such as C300MS/AISI304 and C300MS/AISI1045CS, fabricated in Type-A and Type-D orientations (Figure 9), have shown promising results. Both bimetallic structures exhibited higher flexural YS and Ultimate flexural strength (UFS) compared to their monolithic counterparts.[170] Notably, while the UFS of C300MS/AISI1045CS was 9.2% lower than that of its base material AISI1045CS, the C300MS/AISI304 specimen exceeded its monolithic counterpart by 2.5% (Figure 12). This suggests that interfacial strengthening in C300MS/AISI304 is more effective, likely due to coherent grain orientation bridging across the interface, which enhances load transfer and structural integrity.

A similar interfacial effect was observed in MS1/Cu MMAM structures fabricated using LPBF in the Type-A orientation (Figure 9) under varying scanning speeds. The flexural strength varied significantly, attributed to the presence of defects and suboptimal processing conditions.[179] Among the tested parameters, a moderate scanning speed of 800 mm/s yielded the highest UFS of 557 ± 19 MPa, due to strong interfacial bonding and defect-free (Figure 12B [regarding flexural strength] and Figure 8G and H [regarding interfacial morphology]). Beyond the influence of process parameters, IBL additions can also affect the flexural properties of the MMAM structures. In SS316L/CuSn10 and CuSn10/SS316L, the flexural strength differed due to the incorporation of tin–bronze (TB). Specifically, the addition of TB flexural strength by 20% in both configurations.[58,142] Despite this reduction, both structures exhibited good metallurgical bonding, though dendritic cracks were observed, attributed to CTE mismatch. The more significant reduction in flexural strength observed by Chen *et al.*[142] compared to Chen *et al.*[58] can be attributed to a wider transition zone, which compromises mechanical homogeneity across the interface. Finally, in AlSi10Mg/C18400 MMAM structures, the orientation of the base material significantly influenced flexural performance. When Al served as the substrate, both flexural strength and strain were higher compared to configurations where Cu was the base material.[175] This outcome is linked to the higher porosity and lower mechanical integrity of the Cu-rich region, emphasizing that most of the load-bearing capacity is retained by the Al side. In both cases, porosity formation at the interface, attributed to mismatch thermal properties, resulted in reduced flexural strength.

4.4. Compression strength

Among the available MMAM empirical studies, compression testing remains relatively underexplored, with only a limited number of investigations focusing on this mechanical property. Notably, in MMAM structures such as P21/SS316L[166] and 17-4PH/SS316L,[167] both of which employ ferrous alloys as base materials, distinct deformation behaviors were observed under compression loading. Post-failure analysis revealed that SS316L specimens exhibited axisymmetric plastic deformation, indicative of uniform plastic flow. In contrast, P21/SS316L deformed laterally due to differences in the compressive YS between the constituent materials. These experimental findings were validated by an FEA study, which accurately predicted the observed deformation patterns.[166] Further details regarding the FEA methodology and results are discussed in Section 5. The observed deformation behavior can be further explained by considering the underlying plastic deformation mechanisms. Both 17-4PH and P21 possess a body-centered cubic (BCC) structure, which impedes dislocation motion, while SS316L has a face-centered cubic (FCC) structure that facilitates dislocation slip. This mismatch in crystal structure contributes to the axisymmetric barreling plastic deformation observed (Figure 13B and C). Furthermore, residual thermal stresses arising from mismatched CTE between the materials may also contribute to strain-hardening effects.[147]

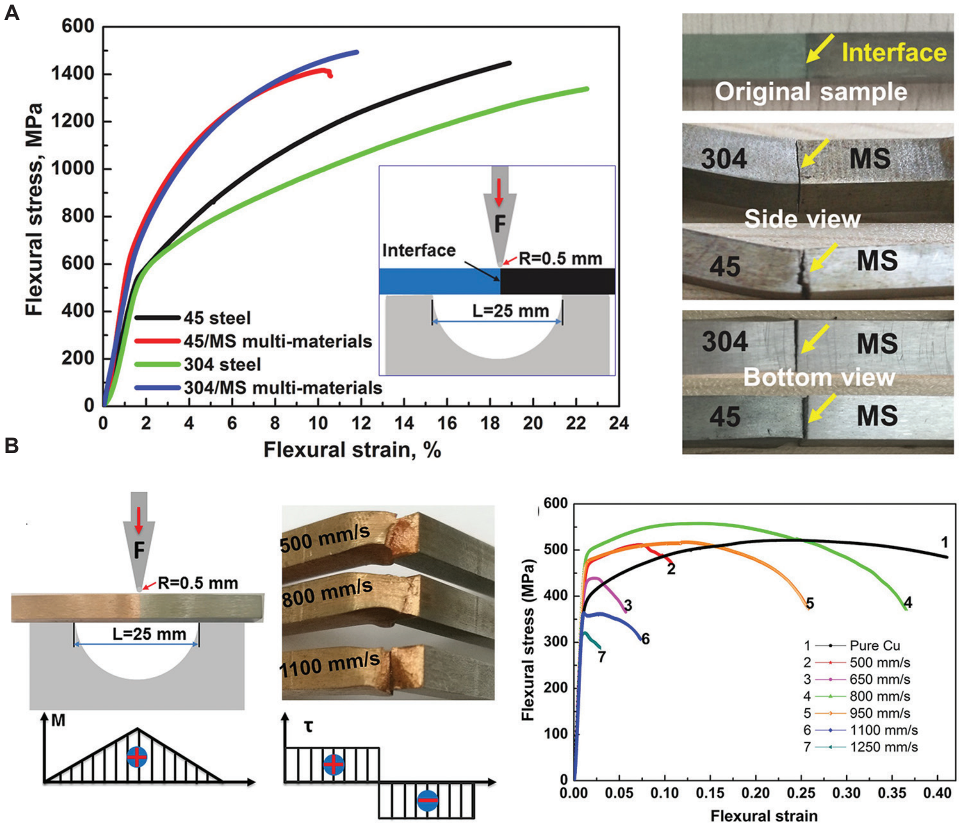

Figure 12. Flexural stress–strain response of bimetallic structures fabricated through mixed-material laser powder bed fusion. (A) C300MS/AISI304 and C300MS/AISI1045 carbon steel;[170] and (B) MS1/T2.[179] The graphs illustrate the flexural strength at the interface of the bimetallic structures and the role of metallurgical bonding under flexural loading.

In the 17-4PH/SS316L MMAM structure, the radially configured specimen exhibited a compressive YS of 654 ± 12 MPa, outperforming the double-layered, single-layered, and monolithic SS316L structures, which showed a 526 ± 4 MPa, 425 ± 7MPa, and 356 ± 17 MPa, respectively. This improvement in performance is attributed to the higher linear CTE of the outside casing (17-4PH) compared to the core (SS316L), and to the zig-zag deposition pattern, which functioned as a mechanical interlock, enhancing bond strength. Among all the tested specimens, a 1:1 premixed MM exhibited the lowest performance (Figure 13C), with a compressive YS of 303 ± 17 MPa, attributed to a reduced volume fraction of solid-solution strengthening elements, such as Ni and molybdenum by 37.5% and 40%, respectively.[147]

In a separate study, the compressive behavior of 18Ni300/CuSn10 with varying percentages of structural porosity was evaluated.[176] As expected, increasing porosity resulted in a systematic reduction in compressive YS, complicating the direct assessment of interfacial mechanical integrity due to the highly porous architecture of the specimens. Similarly, for the TiB/Ti-6Al-4V MMAM structure, the compressive response of a gyroid scaffold design was analyzed for both monolithic Ti-6Al-4V and bimetallic structures. The monolithic structure primarily exhibited a linear elastic zone, followed by an elastic–plastic transition before reaching ultimate strength. In contrast, the bimetallic lattice structure initially demonstrated a non-linear region, followed by a linear elastic response. The initial non-linear

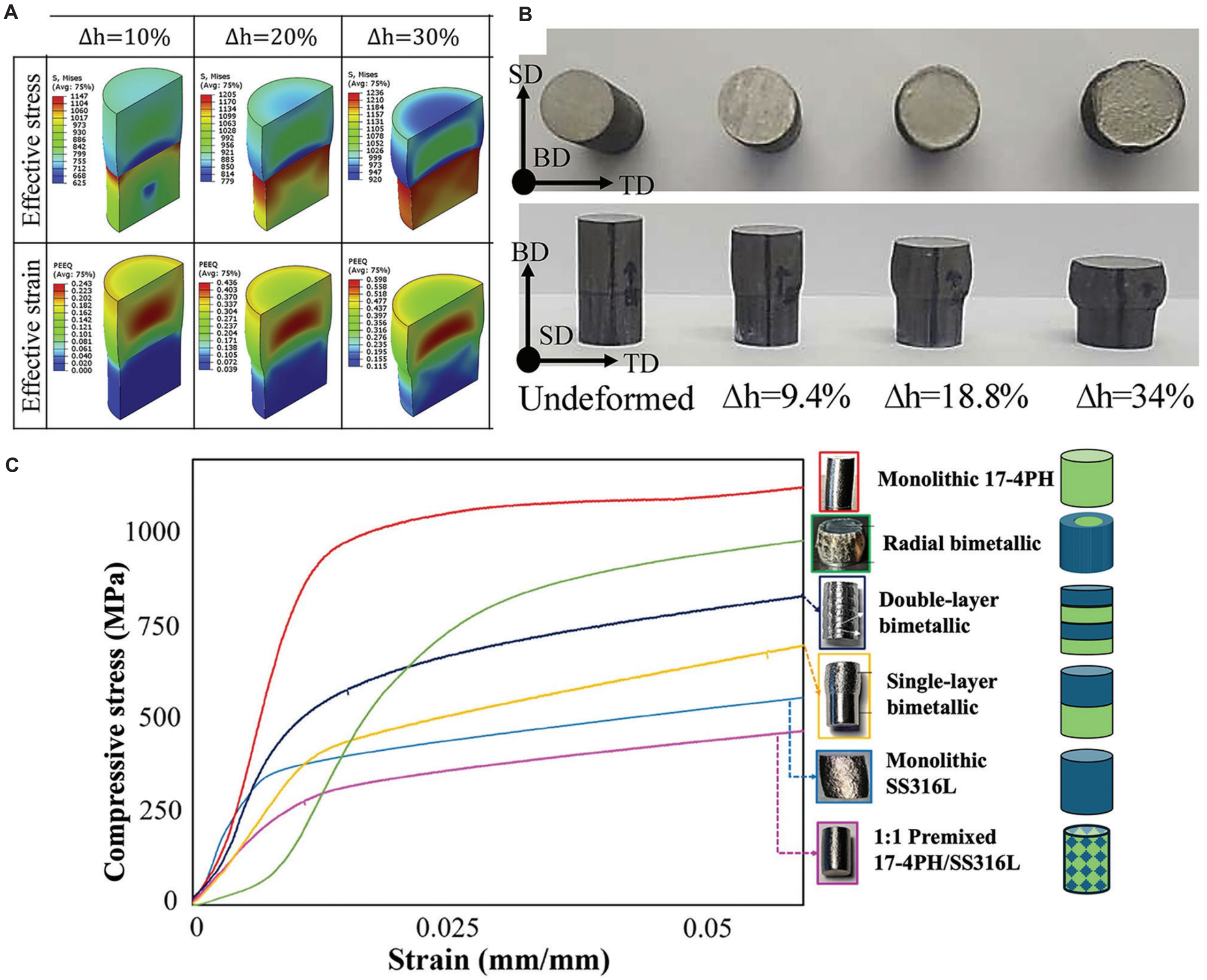

Figure 13. Compression testing of multi-material laser powder bed fusion steel-based bimetallic structures. (A and B) Corresponding numerical deformation simulations of P21/SS316L and time-stamped post-failure views (top and side);[166] and (C) Compressive stress–strain curves for various 17-4PH/SS316L configurations, including monolithic 17-4PH and SS316L, single- and double-layer bimetallic, 1:1 premixed composition, and radial bimetallic design.[147] These results present both experimental and numerical observations, highlighting the influence of architectural design and material distribution on compressive strength and deformation behavior.

behavior was attributed to surface roughness, dimensional deviation of the upper surface, and unevenness of the bottom surface.[189]

4.5. Fatigue life

Fatigue testing remains a fundamental approach for assessing the failure mechanisms of structural components under cyclic loading. Its application in bimetallic structures has gained increasing attention in recent years. Unlike other mechanical properties such as tensile strength and hardness, fatigue failure often occurs without prior visible deformation, potentially leading to catastrophic structural failures. As a result, fatigue testing is considered a critical indicator of dynamic mechanical performance, providing essential insights into the service life and reliability of MM structures, especially in high-cycle applications involving alternating stresses.

In a notable study, Tan *et al.*[170] investigated the fatigue behavior of MMAM structures with ferrous base materials, specifically C300MS/AISI304 and C300MS/AISI1045CS. Both bimetallic structures were evaluated at 30 Hz under 400 MPa stress. C300MS/AISI304 exhibited a significantly longer fatigue life of 4.505×10^6, compared to 0.36×10^6 cycles for C300MS/AISI1045CS. Failure in C300MS/AISI304 occurred on the AISI304 side, whereas in C300MS/AISI1045CS, failure initiated at the interface. Fractographic analysis revealed that the premature failure of C300MS/AISI1045CS was caused by the presence of interfacial pores, while the defect-free interface in C300MS/AISI304 contributed to its superior fatigue resistance.

The fatigue life of bimetallic IN718/SS316L was further examined through two configurations: crack arrester and crack divider.[159] Results indicated that the crack growth rate was influenced by the local crack tip stress intensity factor range (ΔK). Depending on the transition direction (soft-to-hard or hard-to-soft), crack propagation was affected by differences in material properties and grain structure. Fractographic analysis revealed that grain orientation and morphology significantly impacted crack tortuosity and propagation rate. Although dissimilar material interfaces did not show a pronounced effect under high ΔK conditions, crack behavior was markedly influenced by grain structure at lower ΔK values. Overall, Duval-Chaneac *et al.*[159] concluded that residual stress had minimal effect on crack propagation due to careful specimen preparation and the good coherence of grain structures at the interface.

4.6. Miscellaneous tests

While most studies have focused on common and widely available mechanical properties such as hardness and tensile strength, some have explored environmental effects, including thermal diffusivity and wear performance, which are critical for specific application domains. Understanding thermal diffusivity is vital for characterizing the heat transfer behavior of MMAM structures during manufacturing. Thermal diffusivity data provides information on a material's ability to conduct heat relative to its ability to store it. Figure 14 presents both experimental and theoretical thermal diffusivity data for MMAM structures with IN718 as the base material, along with data for the constituent single-alloy materials. The comparison illustrates how the thermal performance of the bimetallic system differs from its monolithic counterparts. Theoretical thermal diffusivity values of the bimetallic structures range from 14.37 to 17.09 mm^2/s between 50°C and 300°C.In contrast, experimental values were found to be lower, ranging from 10.30 ± 07 to 12.33 ± 0.07 mm^2/s within the same temperature range.[184] The thermal diffusivity of the bimetallic structure lies between those of monolithic IN718 and the Cu alloy, reflecting the expected thermal blending behavior.

In addition to thermal behavior, wear performance was also investigated. Wear testing was conducted on an IN718/SS316L MMAM structure with carbon fiber functioning as the IBL. The analysis included comparative wear data for both IN718 and IN718/CF/SS316L. Results showed that IN718/CF/SS316L reached a steady-state wear rate in under 80 seconds, significantly faster than wrought IN718, which stabilized after approximately 300 s.[158]

5. Modeling and simulation for MMAM

An extensive list of in-process and post-fabrication simulation software and codes currently exists for single-material AM across multiple length scales, providing insights into the state of research and development toward MMAM. Experimental investigations are often time-consuming and costly, making them prohibitive for some AM research. Consequently, simulations play a critical role in augmenting understanding, optimizing processes, and enabling process control. Simulations commonly used in single-material AM include thermodynamic modeling, melt pool dynamics, powder bed behavior (PBB), and computational fluid dynamics-volume of fluid (CFD-VOF) models. Thermal simulation modeling is employed to guide parameter selection, ranging from single melt pool point penetration to single or multiple melt pool tracks, and extending to full component modeling at micro-, meso-, and macro-length scales. Melt pool dynamic simulations focus on material behavior during interaction with the laser and heat-affected zone, providing information on melt pool morphology, cooling rates, and microstructural characteristics. PBB simulations model particle–particle interactions on the powder bed, powder

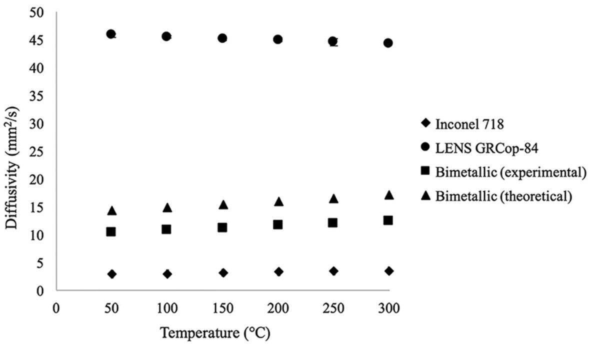

Figure 14. Thermal diffusivity of IN718/CuA bimetallic structure,[184] including measured values for monolithic IN718 and GRCop-84, alongside experimental and theoretical thermal diffusivity values for the bimetallic composition. The comparison illustrates the thermal diffusivity behavior of the bimetallic structure relative to its constituent materials across a temperature range of 50°C to 300°C.

spreading dynamics, and particle–laser interactions during melting. These simulations, often conducted using the discrete element method (DEM), help optimize powder shape or size distribution to achieve ideal powder flow characteristics, thereby improving layering and reducing mesoscale defects. The CFD-VOF model typically includes a laser heat source and a coaxial nozzle with a single powder feeder aligned with the laser path. This model captures key phenomena during LDED, such as powder and gas flow dynamics, laser–powder interactions, attenuation effects, and melt pool behavior.

5.1. Microstructural computational analysis (phase transformation, melt pool formation, and alloy mixing)

Simulating and predicting the microstructural evolution at the interface of bimetallic structures fabricated using MMAM is critical to optimizing their performance in industrial applications. Microstructural simulation and modeling serve as powerful tools to bridge the gap in understanding the links between processing conditions and final material properties. These tools enable the capture of solidification behavior, phase transformations, grain morphology, and elemental diffusion across dissimilar materials. In bimetallic structures with significant differences in thermal properties, computational analysis is essential for evaluating the nature of bonding, transition zone development, and the formation of undesired IMCs, porosity, or other defects. Various techniques—such as the Monte Carlo method, CALPHAD, Lattice Boltzmann, Cline–Anthony model (for melt pool geometry), and smoothed particle hydrodynamics (SPH)–are employed to simulate grain growth, phase diagrams, diffusion at interfaces, and microscale kinetics. Most solidification modeling software or open-source codes have been developed for single-material processes; thus, simulation platforms specifically tailored for MMAM remain underdeveloped, unvalidated, and unqualified. In this section, we review existing literature on the computational analysis of bimetallic structures and processes, with a focus on developments toward MMAM. Specifically, the remainder of this section discusses research conducted on simulating melt pool dynamics, elemental intermixing, phase diagrams, and grain growth during solidification.

Although extensive studies have been conducted on single-material melting and solidification, Sorkin *et al.*[192] presented the first published attempt at simulating MM melting using the open-source molecular dynamics software Large-scale Atomic/Modular Massively Parallel Simulator (LAMMPS), albeit with numerous simplifications. However, the model's assumptions neglected several key physical processes involved in LPBF, including surface tension forces, multiphase flow, and molten pool formation. Moreover, no experimental validation was provided to support the simulation results. Beyond melt pool dynamics, powder deposition plays a significant role in MM applications, influencing interfacial properties based on packing, design, and deposition strategies. Gu *et al.*[23] investigated various deposition patterns involving multiple materials by incorporating particle size distribution data obtained from a particle size analyzer and simulating it employing the DEM (EDEM v2019). The studied deposition patterns included evenly mixed, bimetallic separation, interlock deposition, and FGM. Further discussion on the influence of these deposition patterns on melt pool formation is provided later in this section.

The characteristics of the melt pool, including temperature gradients, thermodynamics, fluid dynamics, and laser–matter interactions, have been thoroughly studied in LPBF and LDED processes. Sun *et al.*[20] applied a DEM approach using ABAQUS FLUENT for multiphase mesoscale modeling of an MM powder bed composed of IN718/Cu10Sn (Figure 15A). This study simulated several powder configurations within a single layer (aligned parallel or perpendicular to the laser scan path, and pre-mixed by wt.%). The simulations focused on melt pool morphology and thermal behavior during single-track laser scans. To simplify the model, the two components were treated as mutually soluble, enabling microlevel mixing. When comparing tracks composed of mixed versus unmixed dissimilar powders, melt pools with a high content of IN718 exhibited higher peak temperatures due to their thermo-physical properties. In the unmixed case, the melt pool size and temperature transitioned gradually as the laser moved from one material to the other.

More recently, Gu *et al.*[23] applied a modified DEM approach to simulate multiple adjacent laser tracks of SS316L/Cu10Sn (Figure 15B and C). As noted previously, the process introduced a variety of powder deposition patterns and compared simulation outcomes with experimental data. In the study, the material was deposited horizontally and vertically to investigate melt pool morphology and temperature distribution (Figure 15C). When observing the melt pool track in both configurations, the vertical deposition of the bimetallic structure exhibited a discontinuous melt pool formation. This discontinuity is attributed to the difference in laser absorptivity between SS316L (0.35) and Cu10Sn (0.03), as well as the higher thermal conductivity of Cu10Sn compared to SS316L, which leads to highly efficient heat dissipation from the beam center to the surrounding powder. In contrast, during horizontal layer deposition, SS316L powder melted first, and the heat conducted from the molten SS316L

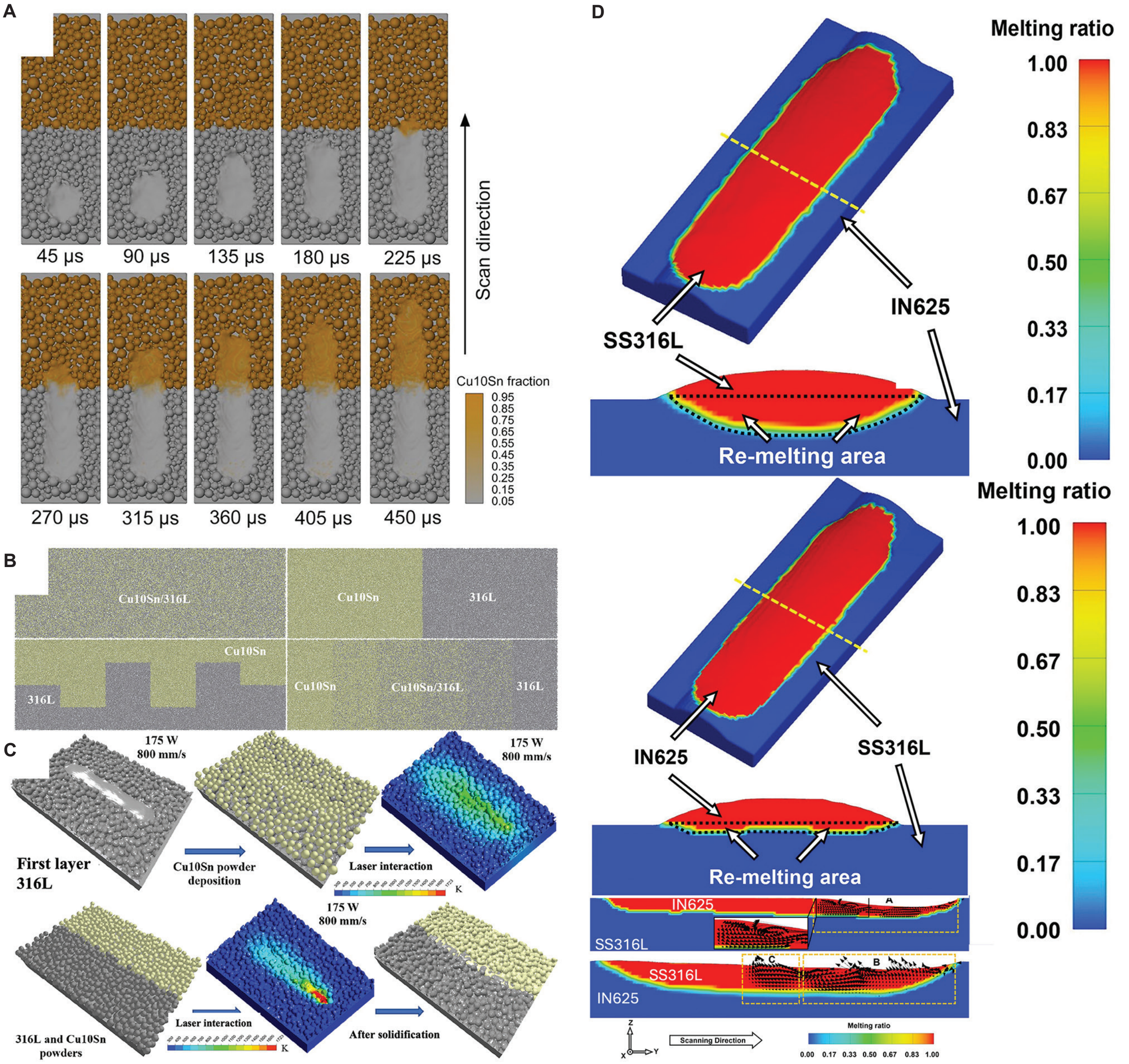

Figure 15. Single-track melting and solidification in selected bimetallic structures. (A) IN718/CuSn10 single-track melting profile;[20] (B and C) SS316L/CuSn10 solidification simulation illustrating thermal and powder solidification dynamics;[23] and (D) single-track solidification of IN625/SS316L (top: Type-A) and SS316L/IN625 (bottom: Type-B) configurations.[132] The visualizations demonstrate the influence of materials order and interfacial configuration on melt pool evolution and solidification morphology.

powder and its convection flow contributed to the melting of Cu10Sn. Scanning electron microscopy analysis further revealed that phase migration was likely driven by this convection flow, which facilitated elemental intermixing across multiple layers.

Interestingly, Zhang *et al.*[193] used the Cline–Anthony model to calculate the melt pool temperature field during the LDED process for CuCr/07Cr15Ni5. Using this model, they successfully predicted printability maps as a function of deposition layer number. A narrowing of the printability window with increasing layer number was found to enhance thermal conductivity, specific heat capacity, and effective density. The calculated results from the proposed analytical model were in good agreement with experimental data. Similarly, Li *et al.*[194] applied a CFD-based approach to model the fabrication process of FGM using MM-LDED. They developed a multiphysics, MM model to simulate thermal gradients, phase transitions, melt pool dynamics, and final part geometry, identifying non-uniformities in material gradation across the transition zone. Ghanavati *et al.*[127] identified that SS 316L is susceptible to composition changes and a lack of fusion, which can lead to porosity due to its high equilibrium vapor pressure. In contrast, IN718 is more prone to distortion, owing to the formation of larger melt pools. In a study involving MM-LPBF TiB_2/Ti-6Al-4V, Chen *et al.*[195] used a multilayer finite element model (ANSYS) to predict temperature gradients and remelting ratios. They assumed that the absorptivity of Ti-6Al-4V is equivalent to that of Ti-alloy powder, while TiB_2 behaves similarly to non-oxide ceramics with relatively high absorptivity. The results showed that the maximum temperature gradient occurred at the interface and demonstrated a direct proportionality between laser power and temperature gradient (Figure 16A), and an inverse proportionality with laser scan speed (Figure 16B). In addition to temperature gradient analysis, a CFD–DEM-based approach was applied to SS316L/W and W/SS316L interfaces to examine melt pool temperature profiles (Figure 16C). The temperature profiles were evaluated with respect to the melting temperatures of SS316L (1658 K) and W (3695 K). The observed characteristic behavior is attributed to the significantly higher thermal conductivity of W, which facilitates efficient heat dissipation. These simulations collectively demonstrate the capabilities of MM thermal-fluid dynamics models in fundamentally investigating the AM process and assessing printability.

Understanding phase stability and phase transformations under variable temperatures, pressures, and compositions is crucial for the development of advanced computational capabilities. In one example, thermodynamic calculations were employed to predict the phases present in high-strength steel/Ti-6Al-4V bimetallic structures. Using CALPHAD, Wei *et al.*[165] identified three intermetallic formations at the interface: α-Fe + Fe_2Ti, Fe_2Ti, and TiFe + β-Ti. Their analysis indicated that a compositional gradient build strategy would not be sufficient to prevent the formation of Fe_2Ti, a brittle IMC. In a similar approach, Kannan *et al.*[196] conducted a CALPHAD analysis on a compositionally graded Al-Cu-Ce-Zr/SS316L joint. They found that composition ratios of 90%, 80%, 20%, and 10% SS316L were promising for fabrication, as no primary intermetallic formations were observed. Instead, a BCC_A2 matrix formed on the Fe-rich side and an FCC_A1 matrix on the Al-rich side. Scheil simulations performed on a P21/704H bimetallic structure fabricated using MM-WAAM revealed drastic variations in volumetric CTE and freezing range due to the formation of an MC carbide phase from the liquid during solidification. This phase formation led to cracking in the intermediate region.[197] Iams *et al.*[198] performed similar testing on GRCop-42/IN718 using Scheil simulation and observed the formation of a C15 Cr_2Nb phase in the GrCop-42 composition. They also reported enrichment in Ni and Fe, which contributed to the formation of the C14 $(Cr,Ni,Fe)_2Nb$ phase and the BCC α-Cr phase. In the case of Ti-6Al-4V/Al-Cu-Mg structures, which exhibit significantly different thermal properties, the interface was found to be prone to cracking due to the formation of IMCs. Based on this understanding, Zhang *et al.*[199] used Scheil–Gulliver simulation and Malac–Distmas calculations to predict the phase diagram and diffusion path of the bimetallic structure. The binary phase diagram and diffusion path of direct Ti–Al bonding revealed high susceptibility to cracking and delamination at the interface (top two panels of Figure 16D). To mitigate interfacial cracking, a Cu interlayer was introduced. The two lower panels in Figure 16D show the predicted IMCs. Since Cu is a eutectoid-forming element with both Ti and Al, it contributes to constitutional supercooling and stabilizes the bonding interface.

Beyond thermal behavior, Chen *et al.*[132] applied a CFD-based approach to investigate melt pool morphology in MM-LDED-processed IN625/SS316L (Type-A) and SS316L/IN625 (Type-B) structures (Figure 15D). In Type-A, an anticlockwise flow at the rear of the melt pool contributed to a fully mixed zone by moving remelted SS316L toward regions of higher temperature. In contrast, the Type-B interface exhibited a clockwise flow, causing unmixed IN625 to rise into the melt pool and become trapped during solidification (Figure 4C and F for experimental validation). The simulation was used to verify and explain the experimental observations previously discussed. Using a similar CFD–DEM-based

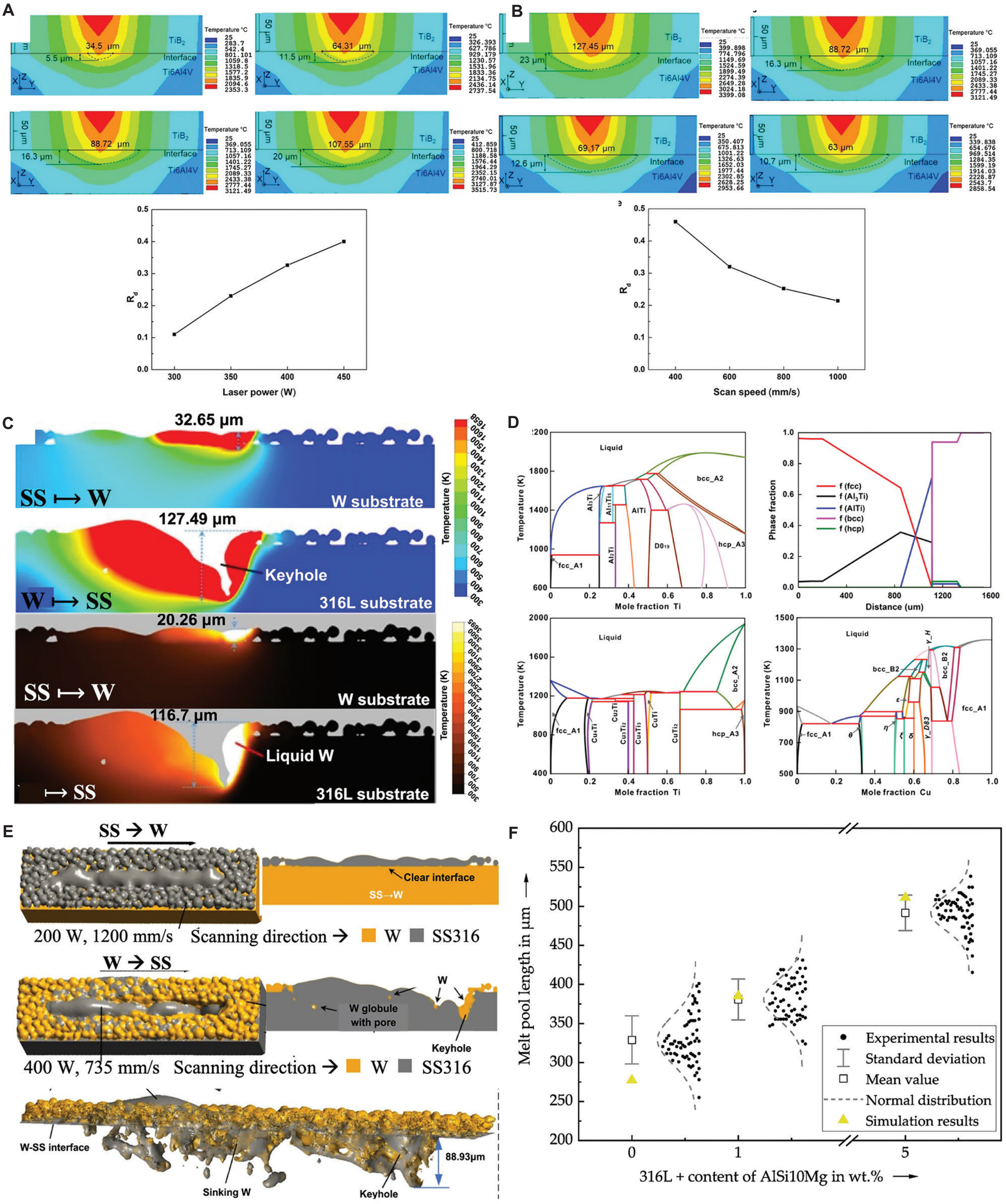

Figure 16. Temperature distribution and melt pool behavior in multi-material laser powder bed fusion (MM-LPBF). (A and B) Cross-sectional temperature profiles in Ti-6Al-4V/TiB$_2$ as a function of laser power and scan speed;[195] (C) Scan track morphology of SS316L/W and W/SS316L, illustrating directional dependency in bimetallic printing;[149] (D) corresponding melt pool temperature profiles ranging from 300 – 1658 K and 300 – 3695 K;[199] (E) Comparison of numerically simulated and experimentally measured melt pool lengths in SS316L/AlSi10Mg;[199] (F) CALPHAD-based phase diagram predictions for Ti-Al, Ti-Cu, and Al-Cu binary phase systems, along with diffusion path analysis for Ti-Al.[200] The images collectively illustrate the influence of process parameters, material combinations, and thermodynamic modeling on thermal behavior in MM-LPBF.

approach, Wei *et al.*[149] simulated the MMAM of SS316L/W bimetallic structures using MM-LPBF, treating the bottom layer material as a substrate (Figure 16E). At the SS316L/W interface (top of Figure 16C), good wettability with the W substrate was observed, and the cross-sectional melt pool view (right-hand side) indicated that W did not melt and no elemental mixing occurred. However, at the W/SS316L interface (bottom of Figure 16E), the SS316L appeared on top of W rather than beneath it. This was attributed to high energy density resulting in keyhole mode melting, as seen in the bottom right-hand side of Figure 16E. The application of excess heat is due to significant differences in thermal properties between SS316L and W. In a similar approach using CFD–DEM based methods, Wimmer *et al.*[200] conducted a numerical simulation of melt pool dimensions in SS/Al and compared the results to experimental data (Figure 16F), utilizing a meshless SPH method.

5.2. Mechanical behavior computational analysis

Finite element modeling (FEM) of MMAM structures is crucial for predicting the mechanical behavior of complex designs, thereby supporting the optimization of material distribution. Recent studies have applied and advanced various modeling software tools to address the structural or thermal qualification of designs using FEM. The presence of dissimilar materials with contrasting mechanical and thermal properties introduces complex residual stresses, especially near the interface. FEM enables detailed analysis of elastic and plastic deformation, residual stress accumulation, interfacial stress distribution, and potential failure mechanisms under various loading conditions. This modeling approach provides insights into the structural reliability of MM structures and is essential for identifying stress concentration zones and guiding design strategies to mitigate defects such as warping, delamination, and cracking. While most of these studies have been validated using multi-polymeric structures,[201,202] due to the relative ease of fabrication compared to metallic structures, only a few have shown the capability of modeling and verifying metallic MMAM structures. McDonnell *et al.*[125] and Zhang *et al.*[199] fabricated MMAM lattice structures using SS316L/17-PH and Ti-6Al-4V/CuA/Al-Cu-Mg, respectively. McDonell *et al.*[125] constructed a bimetallic lattice structure composed of BCC and octet truss architectures using MM-LPBF, with horizontal and vertical material separations (Figure 17A). It was observed that the deformation behavior and stress–strain response of the bimetallic lattice—featuring a combination of ductile and brittle metals—varied with lattice arrangement. The parallel bimetallic lattice structure demonstrated superior energy-absorption performance compared to the series arrangement due to its stress–strain plateau, reduced fracture, and consistent plastic deformation. FEM successfully predicted this behavior. Similarly, Zhang *et al.*[199] investigated a Ti-6AL-4V/CuA/Al-Cu-Mg MMAM gyroid lattice structure (Figure 17B) fabricated using MM-LPBF. FEM analysis of a unit cell showed that the highest levels of equivalent stress and strain occurred at the center of the inclined struts, indicating shear fracture. Due to the differences in strength and stiffness between the Al-rich and Ti-rich regions, the upper portion of the lattice deformed prior to the lower portion.

Likewise, FEA-based compression testing on a P21/SS316L bimetallic cylindrical structure fabricated using MM-LDED revealed significant stress and strain accumulation during the test (Figure 17C). Stress concentration occurred around the circumference of the P21 region as Δh percentage increased, while strain primarily accumulated on the SS316L side.[166] Throughout the test, it was observed that the softer material absorbed a larger portion of the strain, whereas the harder material bore the majority of the stress. This behavior is clearly depicted in the color intensity gradients in Figure 17A-C. It should be noted that due to limitations in software flexibility and adaptability for AM structures—including bimetallic systems—models typically assume smooth surfaces (i.e., neglecting surface roughness), the absence of defects or porosity, and ideal, crack-free interfaces. As a result, FEA results often exhibit notable discrepancies when compared with experimental data. Griffis *et al.*[203] performed site-specific MM structural FEM using local material properties in the MM-LPBF bimetallic fusion zone, modeling the interfacial region as an effective third material. Their FEA method was used to inform a localized redesign of the fusion zone geometry to interlock material regions and improve the global pull-apart strength of the interface.

Few studies have applied MM structural modeling from a computational topology optimization design perspective. Giraldo-Londona *et al.*[204] developed a multi-objective algorithm for the joint design of MM structures, considering both structural and thermal load cases. For comprehensive reviews on multiobjective topology optimization in MMAM component design, readers are referred to Zhang *et al.*[205] and Sanders *et al.*,[206] who provide detailed theoretical insights into the development of MM topology optimization algorithms.

6. Discussion and future direction

6.1. Feedstock recyclability and build material cross-contamination

Post-processing and recycling procedures for parts produced via metal AM using powder feedstock present

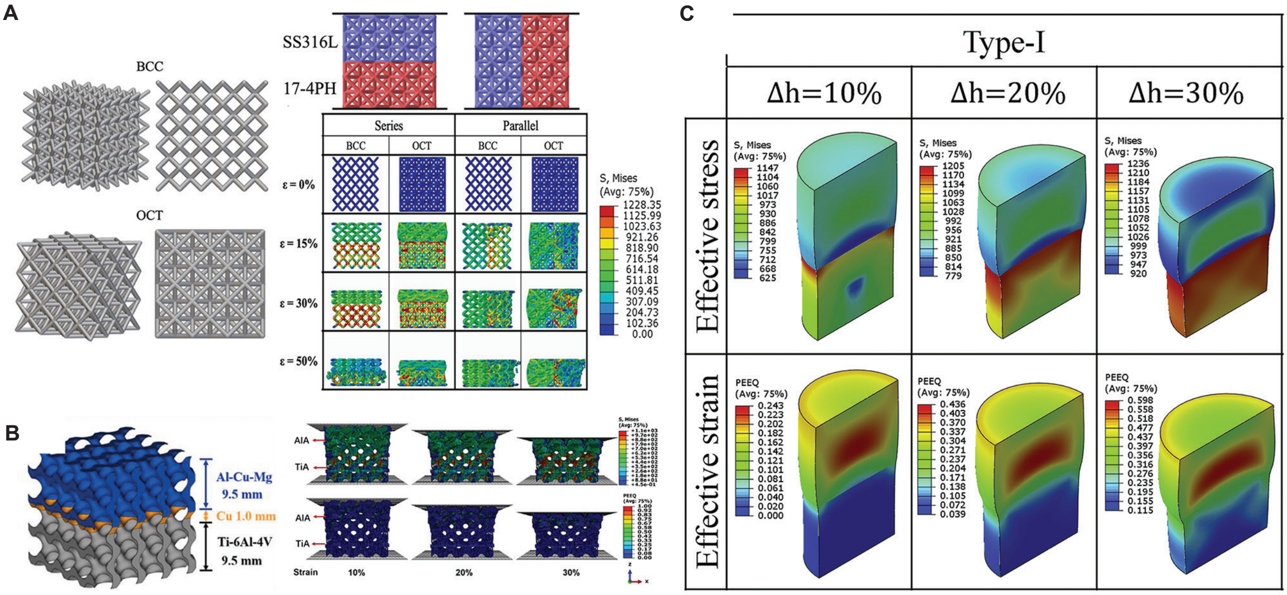

Figure 17. Compression behavior of bimetallic lattice structures fabricated through multi-material laser powder bed fusion (MM-LPBF) and multi-material laser-directed energy deposition (MM-LDED). (A) Finite element modeling-based compression simulation of body-centered cubic and octet truss 17-4PH/SS316L lattice structures fabricated through MM-LPBF;[125] (B) Simulation-based compression test on a gyroid bimetallic Ti-6Al-4V/CuA/Al-Cu-Mg lattice structure fabricated through MM-LPBF;[199] (C) Compression test on a cylindrical P21/SS316L bimetallic structure fabricated using MM-LDED.[166] The finite element analysis results highlight the influence of lattice structure and multi-material additive manufacturing process on deformation behavior under compressive loading

unique challenges compared to mono-material powder bed processing. These challenges primarily stem from the potential for cross-contamination between the materials used in fabrication. In monolithic processing, a single powder material is used across the build plate. Additional recycling steps are necessary to maintain the particle size/shape distribution and chemical composition of the powder, particularly if partial sintering or oxidation has occurred from repeated use. However, no clear standard currently exists to define recycling procedures or specify the required purity of chemical composition after post-processing. This lack of standardization complicates the transition to MM powder recycling, where up to three powder materials may be spatially mixed within a single build plate.

A few efforts have been made to separate powder materials, but none have shown significant success. Sieving can separate powders based on particle size distributions,[175,207,208] but it is ineffective for separating materials with similar particle sizes. Most powders used in LPBF typically fall within a D_{50} size distribution of 10 – 90 μm. As a result, the Gaussian distribution curves of even dissimilar powders overlap at both the upper and lower tails, making clean separation infeasible. Other proposed methods include separation based on relative density (using a particle inertia approach) or magnetic properties. However, all three methods require specific material properties to be effective and cannot be generalized to most powder combinations. To the best of the authors' knowledge, there is currently no comprehensive study on the recycling of leftover powder from MM-LPBF or MM-LDED processes, including the chemical composition analysis of separated materials. This recyclability issue is specific to MM-LPBF and MM-LDED, as there are numerous well-established methods for recycling mono-material powders to control parameters such as powder size distribution,[209-212] chemical composition,[209-211,213,214] flowability,[209-212,214] and morphology.[211-214] Generally, powder reuse introduces additional process uncertainties due to powder degradation. Many studies have reported a moderate reduction in ultimate strength after powder reuse,[211,215,216] while others have found no significant change in mechanical properties following recycling.[217,218] The material consumption and associated costs due to the lack of effective powder recycling methods remain major barriers to the industrial adoption of MMAM. In contrast, wire-fed directed energy deposition and WAAM avoid this issue by using wire-based feedstocks, thus circumventing powder waste altogether. However, the geometric resolution and as-built surface finish provided by these wire-based processes are generally insufficient for many applications unless extensive post-processing is applied.

6.2. In-process monitoring

In-situ process monitoring includes multiple techniques applicable to all MMAM processes, allowing for real-time observation and analysis of the manufacturing process. These methods are essential for assessing the build quality, particularly at the MM interface. *In-situ* monitoring data can also be used to calibrate and inform MM simulations across various length scales, depending on the monitoring technique used.

In-situ monitoring techniques can be broadly categorized into acoustic monitoring, optical imaging, and thermal imaging, and are commonly paired with machine learning algorithms for real-time defect prediction.

Acoustic monitoring utilizes sound waves detected during fabrication as predictive tools to identify internal defects. Acoustic signals generated during processing can be correlated with internal irregularities, enabling the development of AE monitoring systems capable of classifying AE wave patterns associated with specific processing conditions, such as conduction mode, lack-of-fusion pores, and keyhole pore formation.[219] Compared to other *in-situ* methods, this approach is relatively straightforward and particularly useful for detecting internal defects that are otherwise difficult to identify. Acoustic monitoring is commonly combined with complementary optical techniques (e.g., high-speed cameras, IR sensors, photodiodes) to improve detection reliability. One limitation of AE monitoring as a standalone method is the challenge of isolating AE sound waves produced by laser-material interactions from ambient noise generated by the machine or environment.[220] Machine learning algorithms are frequently used to deconvolute these signals, helping to identify and differentiate AE wave patterns associated with defective conditions.[221,222] This approach has been well studied in the context of single-material AM fabrication.[220,223-228]

Build-plate imaging is another widely used *in-situ* technique that monitors the fabrication process on a layer-by-layer basis. High-speed cameras provide real-time feedback on surface quality, layer deposition, and process anomalies such as spatter.[229,230]

Radiographic imaging, including X-ray and computed tomography, offers cross-sectional views of the process, revealing internal structures, voids, and defects.[231] In MMAM, these methods can differentiate most material pairs based on grayscale contrast related to material density. Cross-sectional imaging of the melt pool at metal interfaces provides fundamental insights into melt pool formation mechanisms, supplementing post-process techniques typically used to analyze heat-affected zones. When combined with mesoscale DEM modeling, these techniques can enhance the prediction of melt pool solidification behavior.

Thermal imaging uses IR cameras to capture emitted radiation during the AM process, allowing visualization of temperature gradients, hotspots, and cooling rates. This data is used to identify proper fusion between adjacent layers and detect anomalies with distinct thermal signatures, such as incomplete melting. Thermal maps generated through this method can also be used to calibrate and validate macro-scale process models and simulations, enhancing the understanding of thermally induced distortions and residual stresses.[232] In MMAM, metal matrices often exhibit non-uniform heating and cooling behavior due to differences in material solidification and thermal properties. Thermal imaging can thus serve as an input-control mechanism in real-time monitoring systems to maintain uniform thermal profiles—such as heating/cooling rates or thermal expansion/contraction rates—across the build plate, even in the presence of bimaterial boundaries.[233]

6.3. Standardization of MM testing

Mechanical property characterization tests conducted on monolithic materials fabricated using AM processes typically follow standard testing procedures established for conventionally manufactured specimens. While this approach is suitable for monolithic materials, it is not fully applicable to MMAM due to the unique characteristics of the MM interface between dissimilar materials. The interfacial bonding between two dissimilar materials plays a significant role in determining the failure point and overall mechanical performance of the specimen. Similar to the influence of build orientation in AM, the material deposition configuration significantly affects the mechanical performance of MMAM components. To the authors' knowledge, most experimental studies have not thoroughly investigated deposition configurations to identify optimal strategies for enhancing mechanical performance. For example, Chen *et al.*[58] manufactured SS316L/CuSn10 structures using LPBF with SS316L as the base material and conducted mechanical testing, such as microhardness, tensile, and flexural strength tests. Their tensile testing results indicated that horizontally combined specimens exhibited greater elongation than vertically combined ones, although the UTS was similar in both configurations. Similarly, Dash and Bandyopadhyay[147] fabricated vertically and radially combined SS316L/17-4PH specimens using MM-LDED and observed that radially combined specimens exhibited higher compressive strength than both vertically combined specimens and wrought SS316L. In both cases, mechanical performance was optimized by strategically selecting the material combination configuration. The absence of standardized guidelines regarding material deposition configuration in MMAM highlights a pressing need to establish testing protocols that account for interfacial bonding strength.

To further assess interfacial strength, testing standards must be adapted to evaluate the mechanical performance of MM specimens in multiple dimensions. A notable gap exists in the literature concerning MMAM structures with complex radial interfaces in the horizontal plane while maintaining vertical consistency.

With the site-specific material deposition enabled by AM, traditional strain measurement techniques may be insufficient. In cases where dissimilar materials are deposited in non-conventional orientations (e.g., horizontally or vertically), data from extensometers, crosshead displacement, or strain gauges may not accurately capture local strain behavior within the specimen. In this context, digital image correlation (DIC) emerges as a valuable tool for strain measurement. DIC enables the acquisition of full-field local strain data across the specimen surface, allowing researchers to detect strain localization, necking, and crack initiation. Beyond these advantages, DIC also provides critical information about interface performance and enables the generation of contour maps across the entire specimen, supporting detailed visualization and quantification of strain behavior.

6.4. Thermo-mechanical modelling (part-scale)

Even though a substantial number of simulations have been conducted on MMAM, the field remains less extensive and well-developed compared to single-material AM. This research gap stems from the developmental and fundamental complexities of MMAM. MMAM introduces additional challenges in parameter selection to achieve ideal melting, mixing, and solidification conditions. In single-material AM, selecting parameters often involves optimizing laser power and scan speed for a given material; however, this approach cannot be applied to MMAM, as it would entail extensive experimental costs and time. To address this, a process simulation framework must be developed to identify reasonable process parameters, mitigate significant defects, and achieve desired cooling rates and microstructures. Such a framework would lower the experimental burden required for case-by-case validation of simulation results. The advancements in high-fidelity PBF simulations and the capability of CFD to deliver detailed, high-resolution results need to be extended to MMAM. The importance of particle-based simulations is attributed to the core understanding of the physical phenomena, such as evaporation, recoil pressure, and surface tension, factors that are currently underrepresented in numerical modeling for MMAM. These phenomena are especially critical at material interfaces, where differing thermal properties of dissimilar materials have a major influence. Beyond advancing particle-based simulation approaches, the simulation of multi-track and multi-layer builds is inevitable for linking microscale behavior to part-scale mechanical performance. Modeling of single- and multi-track and multi-layer in single-material AM has been crucial for understanding defect formation and predicting mechanical properties. This approach needs to be expanded to encompass MMAM. Recent work by Küng *et al.*[234] has begun to address this, employing a two-dimensional PBF model using the Lattice–Boltzmann-based simulation (a class of CFD simulation), as well as the DEM-SPH method.[200] To further accelerate the understanding of the multi-track and multi-layer phenomena, the community is encouraged to investigate the integration of DEM-SPH/optimal transportation meshfree—a particle-based method formulated for simulating solid and fluid flows—to address part-scale size challenges. In single-material AM, SPH has experienced extensive developments due to its algorithmic maturity and established track record, which could serve as a foundation for MMAM. Insights from multi-track and multi-layer approaches can also inform FEA simulations, helping to advance the understanding of MMAM's mechanical behavior. However, as discussed in Section 5, existing FEA simulations for MMAM often rely on assumptions that compromise accuracy when compared to experimental data. These assumptions stated throughout the studies will not provide accurate results when compared to the experimental data. Assumptions and simplifications such as a smooth, roughness-free surface, a defect-free or crack-free interface, and a well-bonded interface will yield inaccurate results in MMAM, due to their influence on mechanical behavior. One way to address these limitations is to integrate X-ray micro-computed tomography imaging data as inputs into modeling workflows, enabling more accurate mechanical behavior predictions. In 2024, Auenhammer *et al.*[235] proposed an approach to overcome the image-based numerical modeling for carbon fiber using an open-source Python script.[236] While the method has some drawbacks, it offers a promising future direction for extending image-based numerical modeling to both single- and MMAM.

6.5. Future direction

MM-AM has emerged as a transformative approach in engineering, enabling the integration of distinct metals within a single component to harness their complementary properties. However, when it comes to discrete metal transitions, such as joining high-conductivity Cu to high-strength steel or combining corrosion-resistant

Ni alloys with lightweight Al, the process introduces significant challenges. These challenges stem from the intrinsic differences in thermophysical properties that were discussed in detail in this article, such as melting points, thermal conductivity, and CTE, often leading to residual stresses, cracking, and brittle intermetallic phase formation. Addressing these issues represents a critical frontier in MMAM research and development.

A promising future direction lies in the deliberate design and fabrication of compositionally graded interlayers and engineered interface architectures that facilitate smooth transitions between dissimilar metals. Instead of abrupt material changes—which may offer advantages in certain applications but often introduce sites of mechanical weakness or metallurgical incompatibility—graded transitions and/or IBLs allow for gradual variations in composition and microstructure. These interlayers can mitigate thermal mismatch, reduce stress concentrations, and suppress the formation of brittle intermetallics, thereby enabling strong, defect-free metallurgical bonding. To advance this strategy, several enabling technologies and research methodologies must be leveraged. Computational alloy design tools informed by CALPHAD databases and density functional theory can predict phase stability and guide the development of transition compositions that optimize bonding without compromising functionality. Coupled with this, data-driven approaches such as machine learning can be employed to refine the process parameters in real time, using data from prior builds to predict optimal conditions for layer deposition and fusion quality.

Another key enabler that was discussed in this section is *in situ* monitoring during the printing process. Techniques such as optical pyrometry, thermal imaging, and AE sensing can provide real-time feedback on the thermal environment and melt pool dynamics, allowing immediate adjustment of laser power, scan speed, or feedstock composition. These monitoring strategies can provide valuable data for post-build quality assurance and digital twin development. Furthermore, multiscale modeling and simulation play a vital role in predicting the evolution of thermal gradients, phase transformations, and stress fields across the transition zone. By simulating the build process from the microstructural to the component scale, researchers can anticipate failure modes and iterate on interface designs before fabrication. The successful implementation of discrete metal transitions through MMAM unlocks a wide range of application opportunities. For example, heat exchangers can be designed with Cu-rich regions for high thermal conductivity seamlessly bonded to SS for structural support and corrosion resistance.

In aerospace and nuclear industries, components could be fabricated with spatially varying properties to withstand both mechanical loads and radiation damage. Biomedical implants could combine biocompatible surfaces with load-bearing cores, all within a single manufacturing process. In conclusion, the future of MMAM with discrete metal transitions hinges on the convergence of material science, advanced modeling, real-time sensing, and data-driven control. By developing intelligent interlayer designs and integrating process monitoring with adaptive manufacturing strategies, the field is positioned to overcome longstanding metallurgical barriers and enable a new generation of multifunctional, high-performance components.

Abbreviations

3D	Three-dimensional
AE	Acoustic emission
AM	Additive manufacturing
BCC	Body-centered cubic
CALPHAD	Calculation of phase diagram
CAD	Computer-aided design
CFD	Computational fluid dynamics
CFD-DEM	Computational fluid dynamics – discrete element method
CFD-VOF	Computational fluid dynamics – volume of fluid
CTE	Coefficient of thermal expansion
DEM	Discrete element method
DEM-SPH	Discrete element method – smoothed particle hydrodynamics
DIC	Digital image correlation
EB-PBF	Electron beam powder bed fusion
EBSD	Electron backscatter diffraction
EDS	Energy dispersive spectroscopy
F_{com}	Compression
FCC	Face-centered cubic
FEA	Finite element analysis
F_{fat}	Fatigue
F_{shear}	Shear
F_{therm}	Thermal diffusivity
F_{wear}	Wear performance
FGM	Functionally graded material
FGM-LDED	Functionally graded material laser-direct energy deposition
FSW	Friction stir welding
HV	Hardness Vickers
IBL	Intermediate bonding layer
IMC	Intermetallic compound
IR	Infrared
LDED	Laser-direct energy deposition
LPBF	Laser powder bed fusion
LAMMPS	Large-scale atomic/molecular massively parallel simulator

MM	Multi-material
MMAM	Multi-material additive manufacturing
MM-LDED	Multi-material laser direct energy deposition
MM-LPBF	Multi-material laser powder bed fusion
MM-WAAM	Multi-material wire-arc additive manufacturing
NASA	National Aeronautics and Space Administration
PBB	Powder bed behavior
P-S-P	Process-structure-property
QR	Quick response
SPH	Smoothed particle hydrodynamics
UFS	Ultimate flexural strength
UTS	Ultimate tensile strength
WAAM	Wire-arc additive manufacturing
XRD	X-ray diffraction
YS	Yield strength

Acknowledgments

None.

Funding

Saneej N. Samad and Nadia Kouraytem would like to acknowledge the support by the U.S. Nuclear Regulatory Commission under award number 31310024M0039, and startup funds from USU. Guha Manogharan would like to acknowledge the support by the NSF CMMI-EDSE award #213069, and student support from the Applied Research Laboratory (ARL) at the Pennsylvania State University for their funding contribution through the Walker Fellowship.

Conflict of interest

The authors declare they have no competing interests.

Author contributions

Conceptualization: Nadia Kouraytem, Guha Manogharan
Writing – original draft: Saneej N. Samad, Jacklyn Griffis
Writing – review & editing: All authors

Ethics approval and consent to participate

Not applicable.

Consent for publication

Not applicable.

Availability of data

As this is a review article, no primary research results, data, software, or code have been included.

References

1. Bakewell J. *Customising Production*. Berlin: Springer; 2019.
2. Csere C. How Automakers Are 3D-Printing Parts for Production Cars (and Classics). How Automakers are 3D-Printing Parts for Production Cars (and Classics); 2018. Available from: https://www.caranddriver.com/features/columns/a20684648/how-automakersare-3d-printing-parts-for-production-cars-and-classics [Last accessed on 2024 Sep 28].
3. Gandy D, Albert M. Small Modular Reactor Pressure Vessel Manufacturing and Fabrication Technology Development; 2020. Available from: https://www.energy.gov/sites/default/files/2021/03/f83/ne-amm-david-gandy-1-030221.pdf [Last accessed on 2024 Sep 28].
4. Ellis JK. 3D-Printed Nuclear Reactor Promises Faster, more Economical Path ToNuclear Energy; 2020. Available from: https://www.ornl.gov/news/3d-printed-nuclear-reactor-promisesfaster-more-economical-path-nuclear-energy [Last accessed on 2024 Sep 28].
5. Zhong Y, Rännar LE, Liu L, *et al.* Additive manufacturing of 316L stainless steel by electron beam melting for nuclear fusion applications. *J Nucl Mater*. 2017;486:234-245.
6. McMahon M. Metal AM in the Aerospace Sector: From Early Successes to The transformation of an Industry; 2023. Available from: https://www.metal-am.com/articles/metal-am-inthe-aerospace-sector-from-early-successes-to-the-transformation-of-an-industry [Last accessed on 2024 Sep 28].
7. Russell R, Wells D, Waller J, *et al.* Qualification and certification of metal additive manufactured hardware for aerospace applications. In: *Additive Manufacturing for the Aerospace Industry*. Netherlands: Elsevier; 2019. p. 33-66.
8. González-Barrio H, Calleja-Ochoa A, Lamikiz A, López De Lacalle LN. Manufacturing processes of integral blade rotors for turbomachinery, processes and new approaches. *Appl Sci*. 2020;10(9):3063.
9. Radhika C, Shanmugam R, Ramoni M, Gnanavel BK. A review on additive manufacturing for aerospace application. *Mater Res Exp*. 2024;11(2):022001.
10. Jalui S, Xuan Y, Manogharan G, O'Connor J. Development of a method for shape optimization for a gas turbine fuel injector design using metal-additive manufacturing. *J Eng Gas Turb Power*. 2025;147(1):011023.
11. He P, Sun C, Wang Y. Material distortion in laser-based additive manufacturing of fuel cell component: Three-dimensional numerical analysis. *Addit Manuf*. 2021;46:102188.
12. Hossain A, Pellicotte JT, Stewart M. A calibration approach for accelerated creep testing for electron beam melted (EBM) Ti-6Al-4V using the WCS model. In: *Industrial and Cogeneration; Manufacturing Materials and Metallurgy*. Vol. 8. Boston, Massachusetts, USA: American Society of Mechanical Engineers; 2023. p. V008T17A023.
13. Metal AM. Nexxt Spine Develops Additively Manufactured Spinal Implants using MTS Test Systems; 2019. Available from: https://www.metal-am.com/nexxt-spine-develops-

additivelymanufactured-spinal-implants-using-mts-test-systems [Last accessed on 2025 Sep 28].

14. Harrysson OLA, Marcellin-Little DJ, Horn TJ. Applications of metal additive manufacturing in veterinary orthopedic surgery. *JOM*. 2015;67(3):647-654.

15. Vilardell AM, Takezawa A, Du Plessis A, *et al.* Topology optimization and characterization of Ti6Al4V ELI cellular lattice structures by laser powder bed fusion for biomedical applications. *Mater Sci Eng A*. 2019;766:138330.

16. Tilton M, Lewis GS, Hast MW, Fox E, Manogharan G. Additively manufactured patient-specific prosthesis for tumor reconstruction: Design, process, and properties. *PLoS One*. 2021;16(7):e0253786.

17. Tilton M, Borjali A, Griffis JC, Varadarajan KM, Manogharan GP. Fatigue properties of Ti-6Al-4V TPMS scaffolds fabricated via laser powder bed fusion. *Manuf Lett.* 2023;37:32-38.

18. Shuai C, Li D, Yao X, Li X, Gao C. Additive manufacturing of promising heterostructure for biomedical applications. *Int J Extreme Manuf.* 2023;5(3):032012.

19. F42 Committee. Terminology for Additive Manufacturing - General Principles -Terminology. United States: ASTM.

    doi: 10.1520/F3177-21

20. Sun Z, Chueh YH, Li L. Multiphase mesoscopic simulation of multiple and functionally gradient materials laser powder bed fusion additive manufacturing processes. *Addit Manuf.* 2020;35:101448.

21. He C, Ramani KS, Okwudire CE. An intelligent scanning strategy (SmartScan) for improved part quality in multi-laser PBF additive manufacturing. *Addit Manuf.* 2023;64:103427.

22. Aerosint Company. Aerosint. Available from: https://aerosint.com/printing-services [Last accessed on 2024 Apr 15].

23. Gu H, Wei C, Li L, *et al.* Multi-physics modelling of molten pool development and track formation in multi-track, multi-layer and multi-material selective laser melting. *Int J Heat Mass Transfer*. 2020;151:119458.

24. Toursangsaraki M. A Review of Multi-material and Composite Parts Production by Modified Additive Manufacturing Methods [Preprint]; 2018.

    doi: 10.48550/arxiv.1808.01861

25. Li Y, Feng Z, Hao L, *et al.* A review on functionally graded materials and structures via additive manufacturing: From multi-scale design to versatile functional properties. *Adv Mater Technol.* 2020;5(6):1900981.

26. Mirzaali MJ, Nava AH, Gunashekar D, Nouri-Goushki M, Doubrovski EL, Zadpoor AA. Fracture behavior of bio-inspired functionally graded soft-hard composites made by multi-material 3D printing: The case of colinear cracks. *Materials* (*Basel*). 2019;12(17):2735.

27. Guessasma S, Nouri H, Roger F. Microstructural and mechanical implications of microscaled assembly in droplet-based multi-material additive manufacturing. *Polymers* (*Basel*). 2017;9(12):372.

    doi: 10.3390/polym9080372

28. Vaezi M, Chianrabutra S, Mellor B, Yang S. Multiple material additive manufacturing Part 1: A review: This review paper covers a decade of research on multiple material additive manufacturing technologies which can produce complex geometry parts with different materials. *Virt Phys Prototyp.* 2013;8(1):19-50.

29. Sheydaeian E. *Systems, Materials, and Methodologies for Multi-material Hybrid Additive Manufacturing Functionally Graded Structures*. PhD thesis, University of Waterloo, Ontario, Canada; 2017.

30. Putra NE, Mirzaali MJ, Apachitei I, Zhou J, Zadpoor AA. Multi-material additive manufacturing tech- nologies for Ti-, Mg-, and Fe-based biomaterials for bone substitution. *Acta Biomater*. 2020;109:1-20.

    doi: 10.1016/j.actbio.2020.03.037

31. Doubrovski EL, Tsai EY, Dikovsky D, Geraedts JMP, Herr H, Oxman N. Voxel-based fabrication through material property mapping: A design method for bitmap printing. *Comput Aided Design*. 2015;60:3-13.

32. Skylar-Scott MA, Mueller J, Visser CW, Lewis JA. Voxelated soft matter via multima- terial multinozzle 3D printing. *Nature*. 2019;575(7782):330-335.

33. Griffis JC, Shahed K, Meinert K, Yilmaz B, Lear M, Manogharan G. Multi-material laser powder bed fusion: Effects of build orientation on defects, material structure and mechanical properties. *NPJ Adv Manuf.* 2025;2(1):5.

34. Nazir A, Gokcekaya O, Billah KM, *et al.* Multi-material additive manufacturing: A systematic review of design, properties, applications, challenges, and 3D printing of materials and cellular metamaterials. *Mater Design*. 2023;226:111661.

35. Singh AW, Kapil S, Das M. A comprehensive review of the methods and mechanisms for powder feedstock handling in directed energy deposition. *Addit Manuf.* 2020;35:101388.

36. Luo X, Chang W, Zhong W, Wardle F. Hybrid machine tool design. In: *Hybrid Machining*. Netherlands: Elsevier; 2018. p. 197-214.

37. Gibson I, Rosen D, Stucker B. Directed energy deposition processes. In: *Additive Manufacturing Technologies*. New York: Springer New York; 2015. p. 245-268.

38. Tanwar RS, Jhavar S. A review on additive manufacturing of SS-Ni multi-material fabrication. In: *Materials Today: Proceedings*; 2023. p. S2214785323010866.

39. Wang D, Liu L, Deng G, *et al.* Recent progress on additive manufacturing of multi-material structures with laser powder bed fusion. *Virt Phys Prototyp.* 2022;17(2):329-365.

40. Wei C, Li L. Recent progress and scientific challenges in multi-material additive manufacturing via laser- based powder bed fusion. *Virt Phys Prototyp.* 2021;16(3):347-371.

41. Wu Z, Wilson-Heid AE, Joey Griffiths R, Elton ES. A review on experimentally observed mechanical and microstructural characteristics of interfaces in multi-material laser powder bed fusion. *Front Mech Eng*. 2023;9:1087021.

42. Sun Z, Ion JC. Laser welding of dissimilar metal combinations. *J Mater Sci*. 1995;30(17):4205-4214.

43. Mai TA, Spowage AC. Characterisation of dissimilar joints in laser welding of steel-kovar, copper-steel and copper-aluminium. *Mater Sci Eng A*. 2004;374(1-2):224-233.

44. Estrin Y, Beygelzimer Y, Kulagin R, *et al.* Architecturing materials at mesoscale: Some current trends. *Mater Res Lett*. 2021;9(10):399-421.

45. Gradl PR, Protz C, Fikes J, *et al.* Lightweight thrust chamber assemblies using multi-alloy additive manufacturing and composite overwrap. In: *AIAA Propulsion and Energy 2020 Forum*, VIRTUAL EVENT. USA: American Institute of Aeronautics and Astronautics; 2020.

46. Gradl PR, Protz CS, Ellis DL, Greene SE. Progress in Additively Manufactured Copper-Alloy GRCop-84, GRCop-42, and bimetallic combustion chambers for liquid rocket engines. In: *International Astronautical Congress*.

47. Marques A, Cunha A, Gasik M, Carvalho O, Silva FS, Bartolomeu F. Inconel 718–copper parts fabricated by 3D multi-material laser powder bed fusion: A novel technological and designing approach for rocket engine. *Int J Adv Manuf Technol*. 2022;122(3):2113-2123.

48. Bhaduri D, Penchev P, Essa K, *et al.* Evaluation of surface/interface quality, microstructure and mechanical properties of hybrid additive- subtractive aluminium parts. *CIRP Ann*. 2019;68(1):237-240.

49. Wits WW, Amsterdam E. Graded structures by multi-material mixing in laser powder bed fusion. *CIRP Ann*. 2021;70(1):159-162.

50. Nguyen DS, Park HS, Lee CM. Applying selective laser melting to join Al and Fe: An investigation of dissimilar materials. *Appl Sci*. 2019;9(15):3031.

51. Andreiev A, Hoyer KP, Dula D, *et al.* Laser beam melting of functionally graded materials with application-adapted tailoring of magnetic and mechanical performance. *Mater Sci Eng A*. 2021;822:141662.

52. Bartolomeu F, Costa MM, Alves N, Miranda G, Silva FS. Additive manufacturing of NiTi-Ti6Al4V multi- material cellular structures targeting orthopedic implants. *Optics Lasers Eng*. 2020;134:106208.

53. Tan C, Zhou K, Kuang T. Selective laser melting of tungsten-copper functionally graded material. *Mater Lett*. 2019;237:328-331.

54. Wei C, Liu L, Gu Y, *et al.* Multi-material additive- manufacturing of tungsten - copper alloy bimetallic structure with a stainless-steel interlayer and associated bonding mechanisms. *Addit Manuf*. 2022;50:102574.

55. Wei C, Sun Z, Huang Y, Li L. Embedding anti-counterfeiting features in metallic components via multiple material additive manufacturing. *Addit Manuf.* 2018;24:1-12.

56. Liu L, Wang D, Deng G, *et al.* Interfacial characteristics and formation mechanisms of copper-steel multimaterial structures fabricated via laser powder bed fusion using different building strategies. *Chin J Mech Eng Addit Manuf Front*. 2022;1(3):100045.

57. Wei C, Liu L, Cao H, *et al.* Cu10Sn to Ti6Al4V bonding mechanisms in laser-based powder bed fusion multiple material additive manufacturing with different build strategies. *Addit Manuf.* 2022;51:102588.

58. Chen J, Yang Y, Song C, Zhang M, Wu S, Wang D. Interfacial microstructure and mechanical properties of 316L/CuSn10 multi-material bimetallic structure fabricated by selective laser melting. *Mater Sci Eng A*. 2019;752:75-85.

59. Schneck M, Horn M, Schmitt M, Seidel C, Schlick G, Reinhart G. Review on additive hybrid-and multi-material-manufacturing of metals by powder bed fusion: State of technology and development potential. *Prog Addit Manuf*. 2021;6(4):881-894.

60. Ansari M, Jabari E, Toyserkani E. Opportunities and challenges in additive manufacturing of functionally graded metallic materials via powder-fed laser directed energy deposition: A review. *J Mater Process Technol*. 2021;294:117117.

61. Bhavar V, Kattire P, Thakare S, Patil S, Singh R. A review on functionally gradient materials (FGMs) and their applications. *IOP Conf Ser Mater Sci Eng*. 2017;229:012021.

62. Mahmoud D, Elbestawi M. Lattice structures and functionally graded materials applications in additive manufacturing of orthopedic implants: A review. *J Manuf Mater Process*. 2017;1(2):13.

63. Ren L, Wang Z, Ren L, Han Z, Liu Q, Song Z. Graded biological materials and additive manufacturing technologies for producing bioinspired graded materials: An overview. *Compos Part B Eng*. 2022;242:110086.

64. Saleh B, Jiang J, Fathi R, *et al.* 30 Years of functionally graded materials: An overview of manufacturing methods, Applications and Future Challenges. *Compos Part B Eng*. 2020;201:108376.

65. Xu F, Zhang X, Zhang H. A review on functionally graded structures and materials for energy absorption. *Eng Struct*. 2018;171:309-325.

66. Wei C, Zhang Z, Cheng D, Sun Z, Zhu M, Li L. An overview of laser-based multiple metallic material additive manufacturing: From macro- to micro-scales. *Int J Extreme Manuf*. 2021;3(1):012003.

67. Ostolaza M, Arrizubieta JI, Lamikiz A, Plaza S, Ortega N. Latest developments to manufacture metal matrix composites and functionally graded materials through AM: A state-of-the-art review. *Materials* (*Basel*). 2023;16(4):1746.

doi: 10.3390/ma16041746

68. Ma Z, Liu W, Li W, *et al.* Additive manufacturing of functional gradient materials: A review of research progress and challenges. *J Alloys Compd*. 2024;971:172642.

69. Ju Y, Li C, Yang X, Ba L, Wang Y, Di X. Recent progress on additive manufacturing of steel-based functionally graded materials. *Mater Today Commun*. 2024;40:109953.

70. Sanjeeviprakash K, Rajesh Kannan A, Siva Shanmugam N. Additive manufacturing of metal-based functionally graded materials: Overview, recent advancements and challenges. *J Braz Soc Mech Sci Eng*. 2023;45(5):241.

71. Srivastava M, Rathee S, Tiwari A, Dongre M. Wire arc additive manufacturing of metals: A review on processes, materials and their behaviour. *Mater Chem Phys*. 2023;294:126988.

72. Yan L, Chen Y, Liou F. Additive manufacturing of functionally graded metallic materials using laser metal deposition. *Addit Manuf*. 2020;31:100901.

73. Dev Singh D, Arjula S, Raji Reddy A. Functionally graded materials manufactured by direct energy deposition: A review. *Mater Today Proc*. 2021;47:2450-2456.

74. Tyagi SA, Manjaiah M. Laser additive manufacturing of titanium-based functionally graded materials: A review. *J Mater Eng Perform*. 2022;31(8):6131-6148.

75. Zhang R, Jiang F, Xue L, Yu J. Review of additive manufacturing techniques for large-scale metal functionally graded materials. *Crystals*. 2022;12(6):858.

76. Ghanavati R, Naffakh-Moosavy H. Additive manufacturing of functionally graded metallic materials: A review of experimental and numerical studies. *J Mater Res Technol*. 2021;13:1628-1664.

77. Karimzadeh M, Basvoju D, Vakanski A, Charit I, Xu F, Zhang X. Machine learning for additive manufacturing of functionally graded materials. *Materials*. 2024;17(15):3673.

78. Yang L, Miyanaji H, Ram DJ, Zandinejad A, Zhang S. Functionally graded ceramic based materials using additive manufacturing: Review and progress. In: Shimamura K, Kirihara S, Akedo J, Ohji T, Naito M, editors. *Ceramic Transactions Series*. 1st ed., Vol. CCLVIII. United States: Wiley; 2016. p. 43-55.

79. Delacroix T, Lomello F, Schuster F, *et al.* Influence of build characteristics and chamber oxygen concentration on powder degradation in laser powder bed fusion. *Powder Technol*. 2023;416:11823.

80. Lu SP, Fujii H, Nogi K, Sato T. Effect of oxygen content in He–O_2 shielding gas on weld shape in ultra-deep penetration TIG. *Sci Technol Weld Join*. 2007;12(8):689-695.

81. Li R, Liu J, Shi Y, Wang L, Jiang W. Balling behavior of stainless steel and nickel powder during selective laser melting process. *Int J Adv Manuf Technol*. 2012;59(9-12):1025-1035.

82. Wang D, Wu S, Fu F, *et al.* Mechanisms and characteristics of spatter generation in SLM processing and its effect on the properties. *Mater Design*. 2017;117:121-130.

83. Leung CLA, Marussi S, Towrie M, Atwood RC, Withers PJ, Lee PD. The effect of powder oxidation on defect formation in laser additive manufacturing. *Acta Mater.* 2019;166:294-305.

84. Mertens R, Dadbakhsh S, Van Humbeeck J, Kruth JP. Application of base plate preheating during selective laser melting. *Proc CIRP.* 2018;74:5-11.

85. Guan J, Wang Q. Laser powder bed fusion of dissimilar metal materials: A review. *Materials*. 2023;16(7):2757.

86. Dzogbewu TC, Du Preez WB. Additive manufacturing of Ti-based intermetallic alloys: A review and conceptualization of a next-generation machine. *Materials*. 2021;14(15):4317.

87. International Organization for Standardization. *Additive Manufacturing-General Principles-Terminology.* United Kingdom: ISO/ASTM 52900; 2018.

88. Hasanov S, Alkunte S, Rajeshirke M, *et al.* Review on additive manufacturing of multi-material parts: Progress and challenges. *J Manuf Mater Process*. 2021;6(1):4.

89. Verma A, Kapil A, Klobčar D, Sharma A. A review on multiplicity in multi-material additive manufacturing: Process, capability, scale, and structure. *Materials*. 2023;16(15):5246.

90. Thompson SM, Bian L, Shamsaei N, Yadollahi A. An overview of Direct Laser Deposition for additive manufacturing; Part I: Transport phenomena, modeling and diagnostics. *Addit Manuf*. 2015;8:36-62.

91. Ning J, Zhu L, Wang S, *et al.* Printability disparities in heterogeneous material combinations via laser directed energy deposition: A comparative study. *Int J Extreme Manuf*. 2024;6(2):025001.

92. Feenstra DR, Banerjee R, Fraser HL, Huang A, Molotnikov A, Birbilis N. Critical review of the state of the art in multi-material fabrication via directed energy deposition. *Curr Opin Solid State Mater Sci*. 2021;25(4):100924.

93. Svetlizky D, Zheng B, Vyatskikh A, *et al.* Laser-based directed energy deposition (DED-LB) of advanced materials. *Mater Sci Eng A*. 2022;840:142967.

94. Frank Medina. Fundamental of Additive Manufacturing for Production. Available from: https://www.nrc.gov/docs/ml1816/ml18164a226.pdf [Last accessed on 2025 May 02].

95. Svetlizky D, Das M, Zheng B, *et al.* Directed energy deposition (DED) additive manufacturing: Physical characteristics, defects, challenges and applications. *Mater Today*. 2021;49:271-295.

96. Xie J, Huang Z, Lu H, Zheng B, Xu X, Lei J. Additive manufacturing of tantalum-zirconium alloy coating for corrosion and wear application by laser directed energy deposition on Ti6Al4V. *Surf Coat Technol*. 2021;411:127006.

97. Rai AK, Srinivasulu B, Paul CB, *et al.* Development of thick SiC coating on thin wall tube of zircaloy-4 using laser based directed energy deposition technique. *Surf Coat Technol*. 2020;398:126088.

98. Michael Wilson J, Piya C, Shin YC, Zhao F, Ramani K. Remanufacturing of turbine blades by laser direct deposition with its energy and environmental impact analysis. *J Clean Prod*. 2014;80:170-178.

99. Saboori A, Aversa A, Marchese G, Biamino S, Lombardi M, Fino P. Application of directed energy deposition-based additive manufacturing in repair. *Appl Sci*. 2019;9(16):3316.

100. DebRoy HL, Wei JS, Zuback T, *et al.* Additive manufacturing of metallic components-Process, structure and properties. *Prog Mater Sci*. 2018;92:112-224.

101. Dhanola A, Prasad DS. A comprehensive review of wire arc additive manufacturing for metallic functionally graded materials. *Eng Res Express*. 2024;6(4):042501.

102. Bandyopadhyay A, Heer B. Additive manufacturing of multi-material structures. *Mater Sci Eng R Rep*. 2018;129:1-16.

103. Vimal KEK, Naveen Srinivas M, Rajak S. Wire arc additive manufacturing of aluminium alloys: A review. *Mater Today Proc*. 2021;41:1139-1145.

104. Ding D, Pan Z, Cuiuri D, Li H. Wire-feed additive manufacturing of metal components: Technologies, developments and future interests. *Int J Adv Manuf Technol*. 2015;81(1-4):465-481.

105. Chen Z, Yuan L, Pan Z, *et al.* A comprehensive review and future perspectives of simulation approaches in wire arc additive manufacturing (WAAM). *Int J Extreme Manuf*. 2025;7(2):022016.

106. Reichardt A, Shapiro AA, Otis R, *et al.* Advances in additive manufacturing of metal-based functionally graded materials. *Int Mater Rev*. 2021;66(1):1-29.

107. Akinlabi ET, Akinlabi SA. Friction stir welding of dissimilar metals. In: *Advances in Friction-Stir Welding and Processing*. Netherlands: Elsevier; 2014. p. 241-293.

108. Sun Z, Karppi R. The application of electron beam welding for the joining of dissimilar metals: An overview. *J Mater Process Technol*. 1996;59(3):257-267.

109. Kah P, Shrestha M, Martikainen J. Trends in joining dissimilar metals by welding. *Appl Mechan Mater*. 2013;440:269-276.

110. Powell D, Rennie AEW, Geekie L, Burns N. Understanding powder degradation in metal additive manufacturing to allow the upcycling of recycled powders. *J Clean Prod*. 2020;268:122077.

111. Renderos M, Girot F, Lamikiz A, Torregaray A, Saintier N. Ni based powder reconditioning and reuse for LMD process. *Phys Proc*. 2016;83:769-777.

112. Wang P, Nai MLS, Ng FL, *et al.* Revealing mechanisms underlying powder reusability of Ti-48Al-2Cr-2Nb intermetallic in electron beam powder bed fusion process. *Addit Manuf*. 2022;59:103155.

113. Tang Y, Zhou Y, Hoff T, Garon M, Zhao YF. Elastic modulus of 316 stainless steel lattice structure fabricated via binder jetting process. *Mater Sci Technol*. 2016;32(7):648-656.

114. McGeehan O, Oldfield S, Wilks J, Mawby J, Linaker L. *Testing and Analysis of Additive Manufactured Parts from Partially Recycled Powder*. MEng Thesi, Liverpool John Moores University, Liverpool; 2018.

115. Del Re F, Contaldi V, Astarita A, *et al.* Statistical approach for assessing the effect of powder reuse on the final quality of AlSi10Mg parts produced by laser powder bed fusion additive manufacturing. *Int J Adv Manuf Technol*. 2018;97(5-8):2231-2240.

116. Seyda V, Kaufmann N, Emmelmann C. Investigation of aging processes of Ti-6Al-4 V powder material in laser melting. *Phys Proc*. 2012;39:425-431.

117. Carroll PA, Pinkerton A, Allen J, *et al.* The effect of powder recycling in direct metal laser deposition on powder and manufactured part characteristics. In: *Proceedings of the AVT-139 Specialists Meeting on Cost Effective Manufacture via Net Shape Processing*; 2006. p. 1-8.

118. Lanzutti A, Marin E. The challenges and advances in recycling/re-using powder for metal 3D printing: A comprehensive review. *Metals*. 2024;14(8):886.

119. Mostafaei A, Zhao C, He Y, *et al.* Defects and anomalies in powder bed fusion metal additive manufacturing. *Curr Opin Solid State Mater Sci*. 2022;26(2):100974.

120. Everton SK, Hirsch M, Stravroulakis P, Leach RK, Clare AT. Review of *in-situ* process monitoring and *in-situ* metrology for metal additive manufacturing. *Mater Design*. 2016;95:431-445.

121. Grasso M, Colosimo BM. Process defects and *in situ* monitoring methods in metal powder bed fusion: A review. *Meas Sci Technol*. 2017;28(4):044005.

doi: 10.1088/1361-6501/aa5c4f

122. Sahasrabudhe H, Harrison R, Carpenter C, Bandyopadhyay A. Stainless steel to titanium bimetallic structure using LENS™. *Addit Manuf*. 2015;5:1-8.

doi: 10.1016/j.addma.2014.10.002

123. Tey CF, Tan X, Sing SL, Yeong WY. Additive manufacturing of multiple materials by selective laser melting: Ti-alloy to stainless steel via a Cu-alloy interlayer. *Addit Manufact*. 2020;31:100970.

doi: 10.1016/j.addma.2019.100970

124. Watanabe I, Sun Z, Kitano H, Goto K. Multiscale analysis of

mechanical behavior of multilayer steel structures fabricated by wire and arc additive manufacturing. *Sci Technol Adv Mater.* 2020;21(1):461-470.

doi: 10.1080/14686996.2020.1788908

125. McDonnell B, Errico V, Posa P, *et al.* Bi-metallic lattice structures manufactured via an intralayer multi-material powder bed fusion method. *Addit Manufact*. 2024;89:104301.

doi: 10.1016/j.addma.2024.104301

126. Bettencourt CJ, Kouraytem N. Microstructural characterization of the transition in SS316L and IN625 bimetallic fabricated using hybrid additive manufacturing. *JOM*. 2023;75(12):5079-5087.

doi: 10.1007/s11837-023-06119-4

127. Ghanavati R, Naffakh-Moosavy H, Moradi M, Eshraghi M. Printability and microstructure of directed energy deposited SS316l-IN718 multi-material: Numerical modeling and experimental analysis. *Sci Rep.* 2022;12(1):16600.

doi: 10.1038/s41598-022-21077-8

128. Wei C, Li L, Zhang X, Chueh YH. 3D printing of multiple metallic materials via modified selective laser melting. *CIRP Ann*. 2018;67(1):245-248.

doi: 10.1016/j.cirp.2018.04.096

129. Bodner SC, Van De Vorst LT, Zalesak J, *et al.* Inconel-steel multilayers by liquid dispersed metal powder bed fusion: Microstructure, residual stress and property gradients. *Addit Manufact*. 2020;32:101027.

doi: 10.1016/j.addma.2019.101027

130. Yusuf SM, Zhao X, Yang S, Gao N. Interfacial characterisation of multi-material 316L stainless steel/Inconel 718 fabricated by laser powder bed fusion. *Mater Lett.* 2021;284:128928.

doi: 10.1016/j.matlet.2020.128928

131. Mei X, Wang X, Peng Y, *et al.* Interfacial characterization and mechanical properties of 316L stainless steel/inconel 718 manufactured by selective laser melting. *Mater Sci Eng A*. 2019;758:185-191.

doi: 10.1016/j.msea.2019.05.011

132. Chen N, Khan HA, Wan Z, *et al.* Microstructural characteristics and crack formation in additively manufactured bimetal material of 316L stainless steel and Inconel 625. *Addit Manufact*. 2020;32:101037.

doi: 10.1016/j.addma.2020.101037

133. Ahsan MRU, Fan X, Seo GJ, *et al.* Microstructures and mechanical behavior of the bimetallic additively-manufactured structure (BAMS) of austenitic stainless steel and Inconel 625. *J Mater Sci Technol*. 2021;74:176-188.

doi: 10.1016/j.jmst.2020.10.001

134. Dharmendra C, Shakerin S, Janaki Ram GD, Mohammadi M. Wire-arc additive manufacturing of nickel aluminum bronze/stainless steel hybrid parts - interfacial characterization, prospects, and problems. *Materialia*. 2020;13:100834.

doi: 10.1016/j.mtla.2020.100834

135. Ghanavati R, Naffakh-Moosavy H, Moradi M, *et al.* Design optimization for defect-free AISI 316 L/IN718 functionally graded materials produced by laser additive manufacturing. *Mater Characterization*. 2025;220:114697.

doi: 10.1016/j.matchar.2024.114697

136. Stair J, Webler BA, Beuth JL, De Boer MP. Demonstration and analysis of conditions to obtain a high strength inconel 625 to stainless steel 304l interface by directed energy deposition. *Metall Mater Trans A*. 2024;55(7):2186-2199.

doi: 10.1007/s11661-024-07413-9

137. Li L, Shi Q, Yang S. *In-situ* bonding of horizontal bimetallic interface by laser offset during laser powder bed fusion of copper/nickel multi-material structures and underlying thermodynamic mechanisms. *J Mater Process Technol*. 2025;339:118831.

doi: 10.1016/j.jmatprotec.2025.118831

138. Chen WY, Zhang X, Li M, Xu R, Zhao C, Sun T. Laser powder bed fusion of inconel 718 on 316 stainless steel. *Addit Manuf*. 2020;36:101500.

doi: 10.1016/j.addma.2020.101500

139. Meyer I, Oel M, Ehlers T, Lachmayer R. Additive manufacturing of multi-material parts - design guidelines for manufacturing of 316L/CuCrZr in laser powder bed fusion. *Heliyon.* 2023;9(8):e18301.

doi: 10.1016/j.heliyon.2023.e18301

140. Bai Y, Zhang J, Zhao C, Li C, Wang H. Dual interfacial characterization and property in multi-material selective laser melting of 316L stainless steel and C52400 copper alloy. *Mater Characterization*. 2020;167:110489.

doi: 10.1016/j.matchar.2020.110489

141. Liu ZH, Zhang DQ, Sing SL, Chua CK, Loh LE. Interfacial characterization of SLM parts in multi-material processing: Metallurgical diffusion between 316L stainless steel and C18400 copper alloy. *Mater Characterization*. 2014;94:116-125.

142. Chen K, Wang C, Hong Q, Wen S, Zhou Y, Yan C, Shi Y. Selective laser melting 316L/CuSn10 multi-materials: Processing optimization, interfacial characterization and mechanical property. *J Mater Process Technol*. 2020;283:116701.

143. Meyer I, Messmann CO, Ehlers T, Lachmayer R. Additive manufacturing of multi- material parts - effect of heat treatment on thermal, electrical, and mechanical part properties of 316L/CuCrZr. *Mater Design*. 2025;252:113783.

doi: 10.1016/j.matdes.2025.113783

144. Bulloch A, Harris A, Groom A, Cruchley A, Tuck CJ, Simonelli

M. Fundamental investigation of the interface formation of multi-material additive manufactured 316L-CuSn10 structures. *Metall Mater Trans A*. 2025;56:2586-2603.

doi: 10.1007/s11661-025-07817-1

145. Chen J, Zhang M, Zhao D, Bi G, Bai Y, Xiao Y, Wang D. The impact of interfacial characteristics on the interfacial properties of 316 L/CuSn10 multi-material manufactured by laser powder bed fusion. *Mater Characterization*. 2024;211:113862.

doi: 10.1016/j.matchar.2024.113862

146. Sun Z, Tang C, Soh V, *et al.* Laser powder bed fusion of 316L stainless steel and K220 copper multi-material. *Virtual Phys Prototyp.* 2024;19(1):e2356078.

doi: 10.1080/17452759.2024.2356078

147. Dash A, Bandyopadhyay A. 17-4 PH and SS316L bimetallic structures via additive manufacturing. *Virtual Phys Prototyp.* 2024;19(1):e2292695.

doi: 10.1080/17452759.2023.2292695

148. Zhou Y, Duan L, Li F, Chen K, Wen S. Effect of heat treatment on the microstructure and mechanical property of W/316L multi-material fabricated by selective laser melting. *J Alloys Compd*. 2022;890:161841.

doi: 10.1016/j.jallcom.2021.161841

149. Wei C, Gu H, Gu Y, *et al.* Abnormal interfacial bonding mechanisms of multi-material additive-manufactured tungsten-stainless steel sandwich structure. *Int J Extrem Manuf.* 2022;4(2):025002.

150. Obielodan J, Stucker B. Characterization of LENS-fabricated Ti6Al4V and Ti6Al4V/TiC dual-material transition joints. *Int J Adv Manuf Technol*. 2013;66(9-12):2053-2061.

doi: 10.1007/s00170-012-4481-9

151. Wei K, Zeng X, Li F, Liu M, Deng J. Microstructure and mechanical property of Ti-5Al-2.5Sn/Ti-6Al-4V dissimilar titanium alloys integrally fabricated by selective laser melting. *JOM*. 2020;72(3):1031-1038.

doi: 10.1007/s11837-019-03988-6

152. Zhai W, Wang P, Ng FL, *et al.* Hybrid manufacturing of *γ*-TiAl and Ti-6Al-4V bimetal component with enhanced strength using electron beam melting. *Compos Part B Eng.* 2021;207:108587.

doi: 10.1016/j.compositesb.2020.108587

153. Wang P, Nai MLS, Lu S, Bai J, Zhang B, Wei J. Study of direct fabrication of a Ti-6Al-4V impeller on a wrought Ti-6Al-4V plate by electron beam melting. *JOM*. 2017;69(12):2738-2744.

doi: 10.1007/s11837-017-2610-5

154. Onuike B, Bandyopadhyay A. Functional bimetallic joints of Ti6Al4V to SS410. *Addit Manuf.* 2020;31:100931.

doi: 10.1016/j.addma.2019.100931

155. Scaramuccia MG, Demir AG, Caprio L, Tassa O, Previtali B. Development of processing strategies for multigraded selective laser melting of Ti6Al4V and IN718. *Powder Technol.* 2020;367:376-389.

doi: 10.1016/j.powtec.2020.04.010

156. Onuike B, Bandyopadhyay A. Additive manufacturing of Inconel 718 - Ti6Al4V bimetallic structures. *Addit Manuf.* 2018;22:844-851.

157. Feenstra DR, Molotnikov A, Birbilis N. Effect of energy density on the interface evolution of stainless steel 316L deposited upon INC 625 via directed energy deposition. *J Mater Sci.* 2020;55(27):13314-13328.

doi: 10.1007/s10853-020-04913-y

158. Gorunov AI. Investigation microstructure of carbon fibers reinforced composite on Fe and Ni-based obtained by laser metal deposition. *Surf Coat Technol.* 2019;364:279-288.

doi: 10.1016/j.surfcoat.2019.03.006

159. Duval-Chaneac MS, Gao N, Khan RHU, *et al.* Fatigue crack growth in IN718/316L multi-materials layered structures fabricated by laser powder bed fusion. *Int J Fatigue*. 2021;152:106454.

doi: 10.1016/j.ijfatigue.2021.106454

160. Hinojos A, Mireles J, Reichardt A, *et al.* Joining of inconel 718 and 316 stainless steel using electron beam melting additive manufacturing technology. *Mater Design*. 2016;94:17-27.

doi: 10.1016/j.matdes.2016.01.041

161. Li Y, Liu Z, Wei Z, *et al.* Inhibition of interfacial cracks in 304L-Inconel718 bimetal fabricated via laser powder bed fusion. *Addit Manuf*. 2024;94:104463.

doi: 10.1016/j.addma.2024.104463

162. Chang T, Fang X, Zhou Y, *et al.* Heterogeneous interfaces of aluminum bronze/Inconel 718 dissimilar alloys under different wire arc directed energy deposition sequences. *Int J Extrem Manuf*. 2025;7(1):015003.

doi: 10.1088/2631-7990/ad870f

163. Zhang L, Dong P, Zeng Y, Yao H, Chen J. Additive manufacturing of inconel 718/CuCrZr multi-metallic materials fabricated by laser powder bed fusion. *Addit Manuf*. 2024;92:104377.

doi: 10.1016/j.addma.2024.104377

164. Prestes IB, Jägle EA. Influence of the laser strategy on bi-metallic interfaces printed via multi-material laser-based powder bed fusion. *Addit Manuf Lett.* 2025;13:100274.

doi: 10.1016/j.addlet.2025.100274

165. Wei C, Zhao Z, Wang C, *et al.* Integrated laser additive manufacturing of high-strength steel and Ti6Al4V: Experimental investigations and thermodynamic calculations. *J Alloys Compd.* 2024;983:173902.

doi: 10.1016/j.jallcom.2024.173902

166. Kim DK, Woo W, Kim EY, Choi SH. Microstructure and mechanical characteristics of multi-layered materials composed of 316L stainless steel and ferritic steel produced by direct energy deposition. *J Alloys Compd*. 2019;774:896-907.

doi: 10.1016/j.jallcom.2018.09.390

167. Zhang X, Sun C, Pan T, *et al.* Additive manufacturing of copper - H13 tool steel bi-metallic structures via Ni-based multi-interlayer. *Addit Manuf*. 2020;36:101474.

doi: 10.1016/j.addma.2020.101474

168. Shi Q, Hu Y, Fan H, Yang S. Fundamental role of vertical building sequence and its thermodynamic mechanisms during multi-material additive manufacturing of 18Ni300-CuSn10 structures with IN718 interlayer. *J Manuf Processes*. 2025;144:243-260.

doi: 10.1016/j.jmapro.2025.04.048

169. Bai Y, Zhao C, Zhang Y, Wang H. Microstructure and mechanical properties of additively manufactured multi-material component with maraging steel on CrMn steel. *Mater Sci Eng A*. 2021;802:140630.

doi: 10.1016/j.msea.2020.140630

170. Tan C, Wang D, Ma W, Zhou K. Ultra-strong bond interface in additively manufactured iron-based multi-materials. *Mater Sci Eng A*. 2021;802:140642.

doi: 10.1016/j.msea.2020.140642

171. Khodabakhshi F, Farshidianfar MH, Bakhshivash S, Gerlich AP, Khajepour A. Dissimilar metals deposition by directed energy based on powder-fed laser additive manufacturing. *J Manuf Processes*. 2019;43:83-97.

doi: 10.1016/j.jmapro.2019.05.018

172. Wang P, Lao CS, Chen ZW, *et al.* Microstructure and mechanical properties of Al-12Si and Al-3.5Cu-1.5Mg-1Si bimetal fabricated by selective laser melting. *J Mater Sci Technol*. 2020;36:18-26.

doi: 10.1016/j.jmst.2019.03.047

173. Hauser T, Reisch RT, Seebauer S, *et al.* Multi-material wire arc additive manufacturing of low and high alloyed aluminium alloys with *in-situ* material analysis. *J Manuf Processes*. 2021;69:378-390.

doi: 10.1016/j.jmapro.2021.08.005

174. Ismail L, Mohamed OF, Farrah T, George P, Schiffer A. Influence of process parameters on microstructure and interfacial mechanical properties of Al6061/AlSi10Mg multi-material components fabricated via laser powder bed fusion. *Mater Sci Eng A*. 2025;928:148061.

doi: 10.1016/j.msea.2025.148061

175. Sing SL, Lam LP, Zhang DQ, Liu ZH, Chua CK. Interfacial characterization of SLM parts in multi-material processing: Intermetallic phase formation between AlSi10Mg and C18400 copper alloy. *Mater Characterization*. 2015;107:220-227.

doi: 10.1016/j.matchar.2015.07.007

176. Zhang M, Yang Y, Wang D, Song C, Chen J. Microstructure and mechanical properties of CuSn/18Ni300 bimetallic porous structures manufactured by selective laser melting. *Mater Design*. 2019;165:107583.

doi: 10.1016/j.matdes.2019.107583

177. Ramakrishnan A, Dinda GP. Microstructural control of an Al-W aluminum matrix composite during direct laser metal deposition. *J Alloys Compod*. 2020;813:152208.

178. Zhang W, Liao H, Hu Z, *et al.* Interfacial characteristics and mechanical properties of additive manufacturing martensite stainless steel on the Cu-Cr alloy substrate by directed energy deposition. *J Mater Sci Technol*. 2021;90:121-132.

doi: 10.1016/j.jmst.2021.03.008

179. Tan C, Zhou K, Ma W, Min L. Interfacial characteristic and mechanical performance of maraging steel-copper functional bimetal produced by selective laser melting based hybrid manufacture. *Mater Design*. 2018;155:77-85.

doi: 10.1016/j.matdes.2018.05.064

180. Shah K, Haq IU, Khan A, Shah SA, Khan M, Pinkerton AJ. Parametric study of development of Inconel-steel functionally graded materials by laser direct metal deposition. *Mater Design (1980-2015)*. 2014;54:531-538.

doi: 10.1016/j.matdes.2013.08.079

181. Qingpeng C, Jiachen Y, Xiangyu L, *et al.* Effect of laser powder bed fusion gas flow rate on microstructure and mechanical properties of 316 L stainless steel. *J Manuf Processes*. 2024;132:850-862.

doi: 10.1016/j.jmapro.2024.11.024

182. Jakumeit J, Huang C, Laqua R, Zielinski J, Schleifenbaum JH. Effect of evaporated gas flow on porosity and microstructure of IN718 parts produced by LPBF-processes. *IOP Conf Ser Mater Sci Eng*. 2020;861(1):012011.

doi: 10.1088/1757-899X/861/1/012011

183. Liu L, Wang D, Deng G, *et al.* Laser additive manufacturing of a 316L/CuSn10 multimaterial coaxial nozzle to alleviate spattering adhesion and burning effect in directed energy deposition. *J Manuf Processes*. 2022;82:51-63.

doi: 10.1016/j.jmapro.2022.07.038

184. Onuike B, Heer B, Bandyopadhyay A. Additive manufacturing of Inconel 718-copper alloy bimetal- lic structure using laser engineered net shaping (LENS™). *Addit Manuf*. 2018;21:133-140.

185. Liu W, Dupont JN. *In-situ* reactive processing of nickel aluminides by laser-engineered net shaping. *Metallurgical Mater Trans A*. 2003;34(11):2633-2641.

186. Bergmann JP, Petzoldt F, Schürer R, Schneider S. Solid-state welding of aluminum to copper-case studies. *Welding World*. 2013;57(4):541-550.

187. Chen J, Yang Y, Song C, Wang D, Wu S, Zhang M. Influence mechanism of process parameters on the interfacial characterization of selective laser melting 316L/CuSn10. *Mater Sci Eng A*. 2020;792:139316.

doi: 10.1016/j.msea.2020.139316

188. Zhang J, Song B, Yang L, Liu R, Zhang L, Shi Y. Microstructure evolution and mechanical properties of TiB/Ti6Al4V gradient-material lattice structure fabricated by laser powder bed fusion. *Composit Part B Eng*. 2020;202:108417.

doi: 10.1016/j.compositesb.2020.108417

189. Borisov E, Polozov I, Starikov K, Popovich A, Sufiiarov V. Structure and properties of Ti/Ti64 graded material manufactured by laser powder bed fusion. *Materials* (*Basel*). 2021;14(20):6140.

doi: 10.3390/ma14206140

190. Demir AG, Previtali B. Multi-material selective laser melting of Fe/Al-12Si components. *Manuf Lett*. 2017;11:8-11.

doi: 10.1016/j.mfglet.2017.01.002

191. E04 Committee. Test Method for Microindentation Hardness of Materials. United States: ASTM.

doi: 10.1520/E0384-22

192. Tan JL, Wong CH, Sorkin A. Multi-material modelling for selective laser melting. *Proced Eng*. 2017;216:51-57.

193. Zhang W, Zhang B, Xiao H, Yang H, Wang Y, Zhu H. A layer-dependent analytical model for printability assessment of additive manufacturing copper/steel multi-material components by directed energy deposition. *Micromachines (Basel)*. 2021;12(11):1394.

doi: 10.3390/mi12111394

194. Li W, Kishore MN, Zhang R, *et al.* Comprehensive studies of SS316L/IN718 functionally gradient material fabricated with directed energy deposition: Multi- physics and multi-materials modelling and experimental validation. *Addit Manuf.* 2023;61:103358.

195. Chen C, Gu D, Dai D, *et al.* Laser additive manufacturing of layered TiB2/Ti6Al4V multi-material parts: Understanding thermal behavior evolution. *Optics Laser Technol*. 2019;119:105666.

doi: 10.1016/j.optlastec.2019.105666

196. Kannan R, Lee Y, Pierce D, *et al.* Additive manufacturing as a processing route for steel-aluminum bimetallic structures. *Mater Design*. 2023;231:112003.

doi: 10.1016/j.matdes.2023.112003

197. Sridar S, Klecka MA, Xiong W. Interfacial characteristics of P91 steel - inconel 740H bimetallic structure fabricated using wire-arc additive manufacturing. *J Mater Processing Technol*. 2022;300:117396.

doi: 10.1016/j.jmatprotec.2021.117396

198. Iams AD, Lienert AJ, Otazu DA, Ramoni M. Effects of deposition sequence on microstructural evolution in additively manufactured Cu-Cr-Nb alloy/superalloy bimetallic structures. *Addit Manuf Lett.* 2023;6:100151.

doi: 10.1016/j.addlet.2023.100151

199. Zhang J, Wang X, Gao J, *et al.* Additive manufacturing of Ti-6Al-4V/Al-Cu-Mg multi-material structures with a Cu interlayer. *Int J Mech Sci.* 2023;256:108477.

doi: 10.1016/j.ijmecsci.2023.108477

200. Wimmer A, Yalvac B, Zoeller C, *et al.* Experimental and numerical investigations of *in situ* alloying during powder bed fusion of metals using a laser beam. *Metals*. 2021;11(11):1842.

doi: 10.3390/met11111842

201. Patel KS, Solanki SD, Shah DB, Joshi SJ, Patel KM. Finite element simulation of additive manufacturing process of carbon allotropes. *Int J Interact Design Manuf.* 2023;18:6889-6896.

doi: 10.1007/s12008-023-01221-y

202. Ali MH, Yerbolat G, Kurokawa S. Modeling and simulation of multi-materials for additive manufacturing. *Int J Interact Design Manuf.* 2020;14(3):1057-1069.

doi: 10.1007/s12008-020-00678-5

203. Griffis J, Masker A, Schreiber J, Manogharan G. Site-specific property informed interface design of multi-material laser powder bed fusion. In: *Additive Manufacturing; Advanced Materials Manufacturing; Biomanufacturing*; *Life Cycle Engineering*. Vol. 1. Knoxville, Tennessee, USA: American Society of Mechanical Engineers; 2024. p. V001T01A034.

204. Giraldo-Londoño O, Mirabella L, Dalloro L, Paulino GH. Multi-material thermomechanical topology optimization with applications to additive manufacturing: Design of main composite part and its support structure. *Computer Methods Appl Mech Eng.* 2020;363:112812.

205. Zhang XS, Paulino GH, Ramos AS. Multi-material topology optimization with multiple volume constraints: A general approach applied to ground structures with material nonlinearity. *Struct Multidiscip Optim*. 2018;57(1):161-182.

doi: 10.1007/s00158-017-1768-3

206. Sanders ED, Aguiló MA, Paulino GH. Multi-material continuum topology optimization with arbitrary volume and mass constraints. *Comput Methods Appl Mech Eng.* 2018;340:798-823.

207. Horn M, Prestel L, Schmitt M, *et al.* Multi-material additive manufacturing - recycling of binary metal powder mixtures by screening. *Procedia CIRP.* 2020;93:50-55.

doi: 10.1016/j.procir.2020.04.098

208. Chivel Y. New approach to multi-material processing in selective laser melting. *Phys Proced.* 2016;83:891-898.

doi: 10.1016/j.phpro.2016.08.093

209. Jacob G, Brown CU, Donmez MA, Watson SS, Slotwinski J. *Effects of Powder Recycling on Stainless steel Powder and Built Material Properties in Metal Powder Bed Fusion Processes*. Technical Report NIST AMS 100-6. Gaithersburg, MD: National Institute of Standards and Technology; 2017.

210. Weiss C, Haefner CL, Munk J. On the influence of AlSi10Mg powder recycling behavior in the LPBF process and consequences for mechanical properties. *JOM*. 2022;74(3):1188-1199.

doi: 10.1007/s11837-021-05080-4

211. Koushik T, Shen H, Kan WH, *et al.* Effective Ti-6Al-4V powder recycling in LPBF additive manufacturing considering powder history. *Sustainability*. 2023;15(21):15582.

doi: 10.3390/su152115582

212. Sendino S, Martinez S, Lamikiz A. Characterization of IN718 recycling powder and its effect on LPBF manufactured parts. *Procedia CIRP.* 2020;94:227-232.

doi: 10.1016/j.procir.2020.09.043

213. Ahmed F, Ali U, Sarker D, *et al.* Study of powder recycling and its effect on printed parts during laser powder-bed fusion of 17-4 PH stainless steel. *J Mater Process Technol.* 2020;278:116522.

doi: 10.1016/j.jmatprotec.2019.116522

214. He X, Kong D, Zhou Y, *et al.* Powder recycling effects on porosity development and mechanical properties of Hastelloy X alloy during laser powder bed fusion process. *Addit Manuf.* 2022;55:102840.

doi: 10.1016/j.addma.2022.102840

215. Zhang H, Li J, Li Y. Effect of powder recycling on the organization and mechanical properties of GH4169 alloy by laser metal deposition. *Coatings*. 2023;13(3):659.

doi: 10.3390/coatings13030659

216. Popov VV, Katz-Demyanetz A, Garkun A, Bamberger M. The effect of powder recycling on the mechanical properties and microstructure of electron beam melted Ti-6Al-4 V specimens. *Addit Manuf.* 2018;22:834-843.

doi: 10.1016/j.addma.2018.06.003

217. Carrion PE, Soltani-Tehrani A, Phan N, Shamsaei N. Powder recycling effects on the tensile and fatigue behavior of additively manufactured Ti-6Al-4V parts. *JOM*. 2019;71(3):963-973.

doi: 10.1007/s11837-018-3248-7

218. Nezhadfar PD, Soltani-Tehrani A, Sterling A, Tsolas N, Shamsaei N. *The Effects of Powder Recycling on the Mechanical Properties of Additively Manufactured 17-4 PH Stainless Steel*. Texas: University of Texas at Austin; 2018.

219. Drissi-Daoudi R, Masinelli G, De Formanoir C, Wasmer K, Jhabvala J, Logé RE. Acoustic emission for the prediction of processing regimes in Laser Powder Bed Fusion, and the generation of processing maps. *Addit Manuf.* 2023;67:103484.

doi: 10.1016/j.addma.2023.103484

220. Shevchik SA, Le-Quang T, Farahani FV, *et al.* Laser welding quality monitoring via graph support vector machine with data adaptive kernel. *IEEE Access*. 2019;7:93108-93122.

doi: 10.1109/access.2019.2927661

221. Wasmer K, Kenel C, Leinenbach C, Shevchik SA. *In Situ* and Real-Time Monitoring of Powder-Bed AM by Combining Acoustic Emission and Artificial Intelligence. In: Meboldt M, Klahn C, editors. *Industrializing Additive Manufacturing - Proceedings of Additive Manufacturing in Products and Applications - AMPA2017*. Cham: Springer International Publishing; 2018. p. 200-209.

222. Shevchik S, Le-Quang T, Meylan B, *et al.* Supervised deep learning for real-time quality monitoring of laser welding with X-ray radiographic guidance. *Sci Rep.* 2020;10(1):3389.

doi: 10.1038/s41598-020-60294-x

223. Koester LW, Taheri H, Bond LJ, Faierson EJ. Acoustic monitoring of additive manu- facturing for damage and process condition determination. *AIP Conf Proc*. 2019;2102:020005.

doi: 10.1063/1.5099709

224. Shevchik SA, Masinelli G, Kenel C, Leinenbach C, Wasmer K. Deep learning for in situ and real-time quality monitoring in additive manufacturing using acoustic emission. *IEEE Trans Ind Inform.* 2019;15(9):5194-5203.

doi: 10.1109/TII.2019.2910524

225. Masinelli G, Shevchik SA, Pandiyan V, Quang-Le T, Wasmer K. Artificial intelligence for monitoring and control of metal additive manufacturing. In: Meboldt M, Klahn C, editors. *Industrializing Additive Manufacturing*. Cham: Springer International Publishing; 2021. p. 205-220.

226. Eschner N, Weiser L, Häfner B, Lanza G. Classification of specimen density in Laser powder bed fusion (L-PBF) using in-process structure-borne acoustic process emissions. *Addit Manuf.* 2020;34:101324.

doi: 10.1016/j.addma.2020.101324

227. Ito K, Kusano M, Demura M, Watanabe M. Detection and location of microdefects during selective laser melting by wireless acoustic emission measurement. *Addit Manuf.* 2021;40:101915.

228. Taheri H, Koester LW, Bigelow TA, Faierson EJ, Bond LJ. *In situ* additive manufacturing process monitoring with an acoustic technique: Clustering performance evaluation using

k-means algorithm. *J Manuf Sci Eng*. 2019;141(4):041011.

doi: 10.1115/1.4042786

229. Yang L, Lo L, Ding S, Özel T. Monitoring and detection of meltpool and spatter regions in laser powder bed fusion of super alloy Inconel 625. *Prog Addit Manuf.* 2020;5(4):367-378.

doi: 10.1007/s40964-020-00140-8

230. Zhang Y, Hong GS, Ye D, Zhu K, Fuh JYH. Extraction and evaluation of melt pool, plume and spatter information for powder-bed fusion AM process monitoring. *Mater Design*. 2018;156:458-469.

doi: 10.1016/j.matdes.2018.07.002

231. Nour YA, Gupta N. *In-situ* monitoring of sub-surface and internal defects in additive manufacturing: A review. *Mater Design*. 2022;222:111063.

doi: 10.1016/j.matdes.2022.111063

232. Myers AJ, Quirarte G, Ogoke F, *et al.* High-resolution melt pool thermal imaging for metals additive manufacturing using the two-color method with a color camera. *Addit Manuf.* 2023;73:103663.

doi: 10.1016/j.addma.2023.103663

233. Griffis JC, Shahed KS, Okwudire CE, Manogharan GP. Process Modeling of Multi-Material Laser Powder Bed Fusion. In: *Solid Freeform Fabrication Symposium* 2023; 2023.

234. Küng VE, Scherr R, Markl M, Körner C. Multi-material model for the simulation of powder bed fusion additive manufacturing. *Comput Mater Sci*. 2021;194:110415.

doi: 10.1016/j.commatsci.2021.110415

235. Auenhammer RM, Oddy C, Kim J, Mikkelsen LP. X-ray scattering tensor tomography basedfinite element modelling. *NPJ Comput Mater.* 2023;10:50.

doi: 10.24433/CO.6741464.V2

236. Auenhammer RM, Oddy C, Kim J, *et al.* XX-ray scattering tensor tomography based finite element modelling of heterogeneous materials. *NPJ Comput Mater*. 2024;10(1):50.

doi: 10.1038/s41524-024-01234-5

237. Binder M, Anstaett C, Herzer F, *et al.* Potentials and Challenges of Multi-Material Processing by Laser-Based Powder Bed Fusion. In: *Solid Freeform Fabrication Symposium*; 2018.

238. Paul CP, Yadav SP, Rai AK, Narayanan JA, Bindra KS. Laser directed energy deposition based additive manufacturing of metallic multi-material: A review. *J Metall Mater Sci.* 2021;63:75-87.

doi: 10.1016/j.jmapro.2020.09.008

239. Sing SL, Huang S, Goh GD, *et al.* Emerging metallic systems for additive manufacturing: *In-situ* alloying and multi-metal processing in laser powder bed fusion. *Prog Mater Sci*. 2021;119:100795.

doi: 10.1016/j.pmatsci.2021.100795

240. Mehrpouya M, Tuma D, Vaneker T, Afrasiabi M, Bambach M, Gibson I. Multimaterial powder bed fusion techniques. *Rapid Prototyp J.* 2022;28(11):1-19.

doi: 10.1108/RPJ-01-2022-0014

241. Dzogbewu TC, De Beer D. Powder bed fusion of multimaterials. *J Manuf Mater Process.* 2023;7(1):15.

doi: 10.3390/jmmp7010015

242. Nandhakumar R, Venkatesan K. A process parameters review on selective laser melting-based additive manufacturing of single and multi-material: Microstructure, physical properties, tribological, and surface roughness. *Mater Today Commun.* 2023;35:105538.

doi: 10.1016/j.mtcomm.2023.105538

243. Chen H, He Y, Dash SS, Zou Y. Additive manufacturing of metals and alloys to achieve heterogeneous microstructures for exceptional mechanical properties. *Mater Res Lett.* 2024;12(3):149-171.

doi: 10.1080/21663831.2024.2305261

Appendix

Table A1. Summary of review articles on multi-material additive manufacturing in the past decade

Title	Primary focus	Year	References
Multiple material additive manufacturing – part 1: A review	Review of the MMAM process and principal key processes progress, technological challenges, and future trends as of 2013	2013	28
Additive manufacturing of multimaterial structures	3D-printed polymer-based, metal/metal, and metal/ceramic MMAM applications	2018	102
Potentials and challenges of multi-material processing by laser-based powder bed fusion	Provides a collection of challenges to overcome in MM-LPBF	2018	237
Multi-material additive manufacturing technologies for Ti-, Mg-, and Fe-based biomaterial for bone substitution	Provides a brief review on tissue engineering, design requirements, and metallic biomaterials fabrication technologies	2020	30
Laser direct energy deposition-based additive manufacturing of metallic multi-material: A review	Presents the current state-of-the-art and issues associated with laser-based direct energy deposition in metallic MMAM	2021	238
Critical review of the state of the art in multi-material fabrication via direct energy deposition	Provides a critical review on developing trends, design methodologies, common issues and challenges, and future trends in MM-DED	2021	92
Review on additive manufacturing of multi-material parts: Progress and challenges	Provides information on the latest progress and challenges in MMAM technologies	2021	88
Review on additive hybrid and multi-material manufacturing of metals by powder bed fusion: state of technology and develop- ment potential	Provides information on the state of technology for hybrid and MM manufacturing of metals using AM, particularly PBF processes	2021	59
Emerging metallic systems for additive manufacturing: In-situ alloying and multi-material processing in laser powder bed fusion	Covers the state-of-the-art approach within the perspective of LPBF, and namely, the in situ alloying and multi-material process strategy	2021	239
Recent progress and scientific challenges in multi-material additive manufacturing via laser-based powder bed fusion	Reviews the latest progress in MM powder deposition mechanism, molten pool behavior, process characteristics of printing metal/metal, metal/polymer, and metal/ceramic, and their potential applications	2021	40
Multi-material powder bed fusion technique	Overview of the current state of the MM-PBF techniques	2022	240
Recent progress on additive manufacturing of multi-material structures with laser powder bed fusion	Provides a comprehensive review on achievement in MM structures through LPBF, focusing on interface characteristics, strengthening methods, critical technical issues, and potential problems	2022	39
Powder bed fusion of multi-materials	Provides an overview of the current development for MM-PBF applications	2023	241
A process parameter review on selective laser melting-based additive manufacturing of single and multi-material: microstructure, physical properties, tribological, and surface roughness	Provides information on the influence of LPBF process parameters on the quality of parts fabricated from varied materials and MM structures	2023	242
Multi-material additive manufacturing: A systematic review of design, properties, applications, challenges, and 3D printing of materials and cellular metamaterials.	Presents a comprehensive summary of MMAM systems, fundamental processes, MM combinations, design, modeling, and analysis strategies, focusing on applications and opportunities for using MMAM in various industries	2023	34
A review on additive manufacturing of SS-Ni multi-material fabrication	Summarizes methods used for SS-Ni MMAM, combination strategies, fabrication quality, microstructural variation, property enhancement, challenges, and applications	2023	38
A review on multiplicity in multi-material additive manufacturing: Process, capability, scale, and structure	Covers material combinations in polymer, composites, metals/ceramics, metal alloys, and biomaterials, exploring MMAM capabilities in bi-metallic structures, and functionally or compositionally graded materials, providing insights into various scales and structural aspects	2023	89
A review on experimentally observed mechanical and microstructural characteristics of interfaces in multi-material laser powder bed fusion	Focuses on the material interface characteristics and property performance in MM-LPBF, including common challenges in MMAM	2023	41
Additive manufacturing of metal and alloys to achieve heterogeneous microstructures for exceptional mechanical properties	Reviews the four types of heterogeneous microstructures induced by AM, and discusses the advantages and potential applications of metals and alloys with heterogeneous microstructures made by AM	2024	243

Abbreviations: 3D: Three-dimensional; AM: Additive manufacturing; DED: Direct energy deposition; Fe: Iron; LPBF: Laser powder bed fusion; Mg: Magnesium; MM: Multi-material; Ni: Nickel; PBF: Powder bed fusion; SS: Stainless steel; Ti: Titanium.

Table A2. Summary of multi-material additive manufacturing mechanical testing studies available in the literature

Base material	Hardness/indentation	Bisecting tensile (‖)	Longitudinal tensile (=)	Bisecting flexural (‖)	Longitudinal flexural (=)	Miscellaneous tests
Stainless steel alloy	^{a}SS316/IN625[129]▪					
	^{a}SS316/IN625[132]•					
	^{a}SS316/IN625[157]•					
	^{a}SS316/IN625[126]•					
	^{a}SS316/IN625[133]♦	^{a}SS316/IN625[133]♦				
	^{a}SS316/IN718[128]▪	^{a}SS316/IN718[130]▪				
	^{a}SS316/IN718[130]▪					
	^{a}SS316/IN718[127]•					
	^{a}SS316/CuSn10[128]▪ ^{a}SS316/CuSn10[58]▪	^{a}SS316/CuSn10[58]▪	^{a}SS316/CuSn10[58]▪		^{a}SS316/CuSn10[58]▪	^{a}SS316/CuSn10[58]▪
	^{a,d}SS316/CuSn10[142]▪	^{a,d} SS316/CuSn10[142]▪	^{a,d}SS316/CuSn10[142]▪		^{a,d}SS316/CuSn10[142]▪	
	^{a}SS316/CuSn10[56]▪ ^{a}SS316/CuSn10[187]▪ ^{d}SS316/C18400[141]▪	^{a}SS316/CuSn10[187]▪	^{d}SS316/C18400[141]▪			
	^{a}SS316/C52400[140]▪ ^{d}SS316/W[148]▪		^{d}SS316/W[148]▪			
	^{a}SS316/P21[166]•					^{a}SS316/P21(C) [166]•
	^{a}SS316/17-4PH [147]•					^{a}SS316/17-4PH [147]•
Titanium alloy	^{a}Ti-6Al-4V/IN718[155]▪	^{c,d}Ti/Ti-6Al-4V[189]▪				^{a}TiB/Ti-6Al-4V[188]▪
	^{a}TiB/Ti-6Al-4V[188]▪	^{a}Ti5Al2.5Sn/Ti-6Al-4V[151]▪				
	^{c,d}Ti/Ti-6Al-4V[189]▪					
	^{a}Ti5Al2.5Sn/Ti-6Al-4V[151]▪					
	^{a}Ti-6Al-4V/NiCr/SS410[122]•	^{a}Ti-6Al-4V/Cu/SS316[123]•			^{a}Ti-6Al-4V/Nb/SS410[154]•	
	^{a}Ti-6Al-4V/Nb/SS410[154]•					
	^{a}Ti-6Al-4V/Cu/SS316[123]•					
Nickel alloy	^{a}IN718/Cu[47]▪					^{a}IN718/Cu (TD)[47]▪
	^{a}IN718/SS316[159]▪					^{a}IN718/SS316(F)[159]▪
	^{b}IN718/Cu[184]•					^{a}IN718/CF/SS^{316} (WP)[158]•
	^{a}IN718/Ti-6Al-4V[156]•					
	^{a}IN718/CF/SS316[158]•					
	^{a}NiTi/Ti-6Al-4V[52]▪					^{a}NiTi/Ti-6Al-4V (BS)[52]▪
Ferrous alloy	^{a}Fe/Al12Si[190]▪	^{a}CrMn/MS1[169]▪		^{a}C300MS/AISI-304[170]▪	^{a}MS1/Cu[179]▪	^{a}C300MS/AISI-304 (F)[170]▪
	^{a}CrMn/MS1[169]▪	^{a}C300MS/AISI-304[170]▪		^{a}C300MS/AISI-1045CS[170]▪		^{a}C300MS/AISI-1045CS (F)[170]▪
		^{a}C300MS/AISI-1045CS[170]▪				
		^{a}MS1/Cu[179]▪				
Aluminum alloy	^{d}AlSi10Mg/C18400[175]▪		^{d}AlSi10Mg/C18400[175]▪		^{d}AlSi10Mg/C18400[175]▪	
	^{a}Al/W[177]•					
	^{a}Al-12Si/Al-3.5Cu-1.5Mg-1Si[172]▪		^{a}Al-12Si/Al-3.5Cu-1.5Mg-1Si[172]▪			
	^{a}Al5087/Al6060[173]♦		^{a}Al5087/Al6060[173]♦			
Copper alloy	^{a}CuSn10/18Ni300[176]▪	^{a}CuSn10/18Ni300[176]▪				^{a}CuSn10/18Ni300[176]▪
	^{a}CuSn10/Ti-6Al-4V[57]▪					
	^{a}Cu/H13[167]•					

Note: The build orientation of the specimens is superscripted (a–d) according to the printing type referenced in Figure 10. The superscripted symbol in each cell represents the additive manufacturing process used in the fabrication of those materials. The symbol ▪ represents multi-material laser powder bed fusion, • represents multi-material laser direct energy deposition, and ♦ represents multi-material wire-arc additive manufacturing.

Abbreviations: BS: Bond shear; C: Compression test; F: Fatigue test; TD: Thermal diffusivity; WP: Wear performance.